Simulation of Multiphase Flows with Multiparameter Equations of State and the Discontinuous Galerkin Method

A thesis accepted by the Faculty
of Aerospace Engineering and Geodesy of the University of Stuttgart
in partial fulfillment of the requirements for the degree of
Doctor of Engineering Sciences (Dr.-Ing.)

by

Fabian Hempert

born in Düsseldorf

Main referee:	Prof. Dr. Claus-Dieter Munz
Co referee:	Prof. Dr. Bernhard Weigand
Date of defence:	21.11.2017

Institute of Aerodynamics and Gas Dynamics
University of Stuttgart

2017

To my wife

Preface

This thesis was developed during my work as PhD student at the Central Research of the Robert Bosch GmbH at the Schillerhöhe and in Renningen.

Many thanks to my doctoral advisor, Prof. Claus-Dieter Munz, for his guidance and support. Additionally, without him I would not have applied for the PhD position. Furthermore, I would like to thank the whole Numerical Research Group of Prof. Munz, I always felt welcome during my numerous visits at your institute. I would like to specially thank Malte Hoffmann, Philipp Offenhäuser and Dr. Sebastian Boblest. It was great fun closely working with you for the past three years. Many thanks also to my co-referee Prof. Dr. Bernhard Weigand for spending is valuable time.

Many thanks to the whole CR/ARF(3) in Renningen, especially Hans-Arndt Freudigmann, Julia Leibinger and Irfan Malik, for creating a productive and fun working conditions. For providing the best possible working environment many thanks to my (former) supervisors Dr. Björn Rocker, Dr. Jörg Ziuber, Prof. Jennifer Niessner and Dr. Christian Heinen. I would like to especially highlight Dr. Dr. Uwe Iben for his on-going support, sharing his experience and always asking ”why”.

This work was supported by the Federal Ministry of Education and Research (BMBF) within the BMBF 3. HPC-Call project HONK “Industrialization of high-resolution numerical analysis of complex flow phenomena in hydraulic systems”. The computation resources were provided by the Gauss-Allianz and the computations were carried out at the HLRS in Stuttgart.

My family has been most important throughout, here I would like to thank my mother for her unconditional support. And by far the greatest share of thank goes to my wife Xi, who always encourages me.

Contents

Symbols and Abbreviations

Latin

a	Speed of sound $[\mathrm{m\,s^{-1}}]$
A	Area $[\mathrm{m^2}]$
B	Byte
c	Specific heat capacity $[\mathrm{J\,kg^{-1}\,K^{-1}}]$
c_p	– at constant pressure $[\mathrm{J\,kg^{-1}\,K^{-1}}]$
c_v	– at constant volume $[\mathrm{J\,kg^{-1}\,K^{-1}}]$
D	Diameter or distance of vapor bubbles $[\mathrm{m}]$
e	Specific total energy $[\mathrm{J\,kg^{-1}}]$
E	Total energy [J] or element
f	Free Helmholtz energy $[\mathrm{J\,kg^{-1}}]$
$\vec{\mathbf{F}}$	Flux vector
$\vec{\mathbf{F}}^{\mathrm{A}}$	– for the advection part
$\vec{\mathbf{F}}^{\mathrm{D}}$	– for the diffusive part
$\vec{\boldsymbol{\mathcal{F}}}$	Flux vector in the reference element
g	Gibbs free energy $[\mathrm{J\,kg^{-1}}]$
$\vec{\boldsymbol{\mathcal{G}}}$	Inviscid numerical flux in the reference element
h	Specific enthalpy [J] or distance of the collapse to the wall $[\mathrm{m}]$
H	Enthalpy [J] or distance of the initial bubble to the wall $[\mathrm{m}]$
$\vec{\boldsymbol{\mathcal{H}}}$	Viscid numerical flux in the reference element
J	Jacobian of the mapping
K	Gas law deviation coefficient
M	Mass [kg]
$\dot{m}$	Mass flow rate $[\mathrm{kg\,s^{-1}}]$
p	Pressure $[\mathrm{N^2\,m^{-1}}]$,[Pa]

$\vec{q}$	heat flux vector [$\mathrm{W\,s^{-1}}$]
r	Radius [m]
$r_{0.5}$	Radius at half width [m]
s	Specific entropy [$\mathrm{J\,kg^{-1}\,K^{-1}}$]
	or shock speed in Riemann solver [$\mathrm{m\,s^{-1}}$]
S	Entropy [$\mathrm{J\,K^{-1}}$]
S_P	Persson and Peraire sensor
t	Time [s]
T	Absolute temperature [K]
T_c	Critical temperature [K]
T_s	Saturation temperature [K]
u	Specific inner energy [$\mathrm{J\,kg^{-1}}$]
U	Inner energy [J]
	or Vector of conservative quantities
v	Specific volume [$\mathrm{m^3\,kg^{-1}}$]
V	Volume [$\mathrm{m^3}$]
$\vec{w} = (w_1, w_2, w_3)^\mathrm{T}$	Velocity vector [$\mathrm{m\,s^{-1}}$]
w_0	Velocity at centerline for a jet [$\mathrm{m\,s^{-1}}$]
w_J	Velocity at nozzle orifice for a jet [$\mathrm{m\,s^{-1}}$]
x	Vapor mass fraction
$\vec{x} = (x_1, x_2, x_3)^\mathrm{T}$	Spatial coordinates [m]
z	Distance [m]
Z	Compressibility factor

Greek

α	Correction term
	or vapor volume fraction
β	Expansion coefficient [$\mathrm{K^{-1}}$]
δ	Reduced density ($\delta = \rho/\rho_\mathrm{c}$)
$\delta_{i,j}$	Kronecker symbol
ϵ	Relative error
ϵ_th	Error threshold
η	Dynamic viscosity [$\mathrm{Pa\,s}$], [$\mathrm{kg\,m^{-1}\,s^{-1}}$]
γ	Surface tension [$\mathrm{N\,m^{-1}}$]
$\varkappa$	Isentropic coefficient

λ	Thermal conductivity [$\mathrm{W\,K^{-1}\,m^{-1}}$]
ν	Kinematic viscosity [$\mathrm{m\,s^{-1}}$]
$\xi = (\xi_1, \xi_2, \xi_3)^{\mathrm{T}}$	Coordinates in the reference element
ω	acentric factor
Ω	Domain
ϕ	Dimensionless Helmholtz free energy
ϕ^0	– ideal gas part of ϕ
ϕ^{r}	– residual part of ϕ
Φ	Thermodynamic variables
ρ	Density [$\mathrm{kg\,m^{-3}}$]
σ	Cavitation number
τ	Inverse reduced temperature ($\tau = T_{\mathrm{c}}/T$)
$\underline{\tau}$	shear-stress tensor
$\vec{\nabla}$	Nabla operator

Subscripts

$(.)_0$	Initial state
$(.)_{\mathrm{a}}$	Ambient or averaged state
$(.)_{\mathrm{c}}$	Critical
$(.)_{\mathrm{col}}$	Collapse
$(.)_{\mathrm{g}}$	Gas state
$(.)_{\mathrm{in}}$	Inlet value
$(.)_{\mathrm{l}}$	Liquid state
$(.)_{\mathrm{L}}$	Left state
$(.)_{\mathrm{m}}$	Molar
$(.)_{\mathrm{max}}$	Maximum value
$(.)_{\mathrm{min}}$	Minimum value
$(.)_{\mathrm{n}}$	Nozzle orifice
$(.)_{\mathrm{out}}$	Outlet value
$(.)_{\mathrm{s}}$	Solid state
$(.)_{\mathrm{S}}$	Sutherland reference value
$(.)_{\mathrm{R}}$	Right state
$(.)_{\mathrm{t}}$	Total thermodynamic value

	or time derivative
$(.)_\infty$	Far field
$(.)_*$	state in star region

Superscripts

$(.)^0$	Ideal gas part
$(.)^c$	Critical part
$(.)^r$	Residual part
$(.)', (.)'', (.)'''$	States at phase boundary line
$(.)^*$	Non-dimensional collapse time
	or numerical flux function normal to surface

Abbreviations

BC	Bubble Cloud
BR	Bassi-Rebay
CH_4	Methane
CO_2	Carbon dioxide
DG	Discontinuous Galerkin
DGI	Direct Gas Injector
DGSEM	Discontinuous Galerkin Spectral Element Method
DNS	Direct Numerical Simulation
DOF	Degree(s) of Freedom
EOS	Equation of State
FD	Finite Difference
FV	Finite Volume
HEM	Homogeneous Equilibrium Model
HLLC	Harten-Lax-van Leer-Contact flux function
HLRS	High Performance Computing Center Stuttgart
IAPWS	International Association for the Properties of Water and Steam
IG	Ideal gas
LES	Large Eddy Simulation
LF	Lax-Friedrichs flux function
Ma	Mach number
MILES	Monotonically Integrated Large Eddy Simulation
NG(I)	Natural Gas (Injector)
NSE	Navier-Stokes equations
Pr	Prandtl number
PR	Pressure ratio
(U)RANS	(Unsteady) Reynolds-Averaged Navier-Stokes equations
VB	Vapor Bubble
Re	Reynolds number
RG	Real gas
SATP	Standard Ambient Temperature and Pressure
SGS	Subgrid Scale
TVD	Total Variation Diminishing
VFS	Vapor fraction study
VOF	Volume Of Fluids

Xe	Xenon

Kurzfassung

Numerische Simulationen von Mehrphasenströmungen für industrielle Anwendungen werden immer komplexer. Die benötigten Auflösungen für die zeitlichen und räumlichen Skalen sind stark gestiegen und komplexere und numerisch anspruchsvollere thermodynamische Eigenschaften von Fluiden müssen berücksichtigt werden. Das Ziel dieser Arbeit ist es die Anwendungen von Methoden höherer Ordnung, der diskontinuierlichen Galerkin Spektral Element Methode, und einer genauen Zustandsgleichung für einen weiten Bereich von Druck und Temperatur, die freie Helmholtz-Energie, zu demonstrieren. Bislang wurden beide Aspekte oftmals voneinander getrennt untersucht, allerdings bleibt die Kombination aus beiden weiterhin sehr herausfordernd, beispielsweise für Strömungen mit Kavitation oder Freistrahlen mit Realgaseigenschaften. Die vorliegende Arbeit beschreibt den Einsatz einer diskontinuierlichen Galerkin Methode mit einer tabellierten Zustandsgleichung. Diese Zustandsgleichung beinhaltet die Gas-, Flüssigkeits- und deren Mischungsphase. Dieser Ansatz erlaubt eine detaillierte Untersuchung von Strömungsvorgängen, welche eine genaue Zustandsgleichung benötigen und bisher nicht durchführbar wurden. Die hier untersuchten Fälle beinhalten Überschallfreistrahlen mit Realgaseingenschaften und kavitierende Strömungen.

Es wurden Riemann-Probleme untersucht, bei welchen der Unterschied zwischen idealer und realer Zustandsgleichung erörtert wurde. Die Ergebnisse zeigen zum einen, dass bei höheren Drucken die ideale Zustandsgleichung deutliche abweicht. Zum anderen wurde eine sehr gute Übereinstimmung mit der analytischen Lösung erzielt. Die Ergebnisse für Überschallfreistrahlen deuten auf große Unterschiede zwischen Real- und Idealgasappoximationen für wichtige Kenngrößen wie Massenströme hin. Ein weiterer Unterschied ergibt sich bei Stoßstrukturen, welche zur Beeinflussung von Akustik und dem Mischungsverhalten führen können. Für die kavitierenden Strömungen wurde eine detaillierte Parameterstudie für den Kollaps einzelner Dampfblasen in einer Flüssigkeit durchgeführt. Durch die durchgeführten Simulationen konnten verschiedene Einflussgrößen auf den Kollaps gezeigt werden, beispielsweise den Einfluss der Gitterauflösung auf den maximalen Kollapsdruck. Weiter wurde eine Kanalströmung mit Wasser untersucht, dabei konnten eine Vielzahl von Effekten abgebildet werden. Ein Beispiel hierbei ist die langsame und stromaufwärts verlaufene Ausbreitung von Stoßwellen innerhalb des Naßdampfgebietes, welche auch in Experimenten zu beobachten ist. Generell zeigten die Ergebnisse in dieser Arbeit mit dem diskontinuierlichen Galerkin Ansatz bessere Ergebnisse als mit einem Finite Volumen Verfahren zweiter Ordnung.

Der hier verwendete Ansatz zeigt großes Potenzial für Strömungen, welche eine hohe Auflösung von Skalen benötigen. Es wurden erste Ergebnisse für industriell relevante Fälle für Ein- und Mehrphasenströmungen gezeigt. Dennoch sind weitere Verbesserungen des Ansatzes nötig, um das volle Potenzial der Methode ausschöpfen zu können.

Abstract

Numerical simulations of multiphase flows for industrial applications have become increasingly complex. The demand on the resolution of temporal and spatial scales has increased and more complex and numerically demanding thermodynamic states of the fluid are required. The aim of this study is to demonstrate the applicability of a high order method, i.e., the discontinuous Galerkin spectral element method, with an accurate equation of state, valid for a wide range of pressures and temperatures, e.g., the Helmholtz energy formulation. Although these two aspects have been intensely investigated separately, a combination of both in an efficient manner remains challenging for complex applications, e.g., cavitational flows or real gas jets. The present work presents the application of a novel approach, which uses a dense gas approach with a discontinuous Galerkin method with a tabulated equation of state including the gaseous, liquid and two-phase states of the fluid. This new approach allows for detailed investigations of flow phenomena, which require accurate fluid properties and have been unfeasible to simulate in the past. The investigated cases include supersonic real gas jets and cavitational flows.

Riemann-problems are investigated to demonstrate the differences between ideal and real equation of state approximations. The results show on one hand that at high pressures the ideal approximation of the equation of state shows large differences. On the other hand, a very good agreement of the applied method compared to analytical results is shown. The simulation results for the supersonic real gas jet suggest large differences for the applied cases between the real gas and ideal gas approximation. A difference are the shock structures which might lead to differences in acoustics and mixing. Further, the mass flow rates show significant differences. For the cavitational flow a detailed parameter study for single vapor bubble collapses in a liquid is executed. The presented results demonstrate difference influence quantities for such collapses, e.g., the influence of the grid resolution to the maximum collapse pressure. Subsequently, a micro channel flow simulation is conducted for water for many known effects could be reproduced by the simulation. An example is the shock propagation within the wet steam area, which is very slow compared to the mean flow velocities and is traveling in the upstream direction.

For both the real gas and cavitating flow, using the low dissipation discontinuous Galerkin scheme shows superior results compared to a second order finite volume scheme used in this work. The proposed framework shows great potential for the simulation of flows, that require an accurate representation of small spatial and temporal scales and multiparameter equation of states. First simulation results of industrially rel-

evant flows are presented for both single and multiphase application. However, to fully exploit the potential of the combination high order methods with accurate equation of states further development is necessary, e.g., stability and sub-grid scale models.

1. Introduction

1.1. Motivation

Numerical simulations of fluid dynamics have become an indispensable tool in product development. With their help properties, which are hard or impossible to obtain in experiments are available for interpretation. It has provided the opportunity to model the interaction between components. This allows for a better understanding of complex processes and can be used to solve problems more efficiently. Hence, the direct connection of parameters can be unfolded. Therefore, the environmental sustainability, profitability, durability and safety of new innovative products can be further improved.

Many of today's engineering tasks within an industrial context are of large scale and very complex. One example of the demanding type of simulation is multiphase flow within an injection system for internal combustion engines. During the injection of the fuel high pressure drop can occur, which might lead to cavitation. Cavitation causes strong pressure amplitudes, which can potentially harm components. Consequently, such effects need to be predicted by the simulation. Another example is the gas injection at high pressure. Here, the gas behaves differently than at low pressures and the modeling of the fluid properties is far more complicated. Therefore, much research has been done to improve Computational Fluid Dynamic (CFD) solvers to cater to the needs of component developers.

Here, a number of advances have been made in the last decades, however, many challenges remain for the coming decades. Two of the challenges, which are addressed in the present work, are the accurate representation of the fluid properties, e.g., Equation of State (EOS), and the usage of highly accurate schemes for the simulation, e.g., a Discontinuous Galerkin (DG) method.

1.2. Previous research

In the following, a brief overview of research done in the field of gas dynamics of supersonic flows, cavitation and thermodynamic properties of fluids is given.

1.2.1. Gas Dynamics of Supersonic Flows

Gas dynamics play an important role in industrial applications. In recent years, Natural Gas Injection (NGI) of automotive vehicles has moved into the research focus [28, 68].

With advances in NGI technology pollutions emission and operation costs can be reduced. A trend in the mobilities sector is to move towards lower carbon-to-hydrogen ratios [32]. Therefore, it is desirable to strive towards better designs for NGI systems. For this purpose, simulations are required to accurately predict NGI systems in the most efficient manner.

Research has been done in many different areas for compressible supersonic jets, e.g., noise emission [99, 117, 118, 120, 121], hazardous effects of gas leaks [64] or different transient stages of jet development [51, 54, 129]. Observations and investigations of supersonic jets date back to the nineteenth century during the Franco-Prussian War. For an artillery fire a new phenomena was observed, firing at high speeds resulted in two separate noises, i.e., the jet shock noise and the explosion of the gunpowder, and only a single sound pf the gunpowder explosion at low speeds [87]. From this starting point a number of studies were carried out; for both experiments and in recent years an increasing number of simulations.

Despite the increases in available computational resources Direct Numerical Simulations (DNS) are out of reach for high Reynolds number jet. However, Large-Eddy simulations (LES) have become feasible in recent years. An example of the advances was given by Yu et al. [139]. They investigated the transient behavior of a natural gas (NG) jet both experimentally and numerically in the ideal gas regime. The simulation results agreed well with the experimental data. Vuorinen et al. [129] conducted a study with variation in the ratio of inlet to outlet pressure. The resulting underexpanded jets ranged from pressure ratio 4.5 to 8.5 at Reynolds numbers (Re) of the order from 7.5×10^4 to 1.4×10^5. Their discussion included the transient stages of the jets and identified coherent structures downstream of the Mach disk.

Most of the studies have focused on jets at low pressures. At low pressure real gas effects only have a minor contribution to the jet behavior and its properties. Therefore, real gas effects are less frequently taken into account. However, Direct Gas Injection (DGI) for natural-gas-powered internal combustion engines operate at high pressures [79, 80], e.g., to increase the mass flow. Here the ideal gas approximation is no longer valid. Real gas effects such as pressure-dependent compressibility need to be considered. For the modeling of these effects cubic EOS are most commonly used in CFD [40]. The most prominent examples are Redlich-Kwong [101], Soave-Redlich-Kwong [110], Peng-Robinson [91], Beattie-Bridgeman [70] and Abel-Noble [27] EOS.

An example of the usage of such an EOS for CFD was given by Bonelli et al. [19] and Hamzehloo and Aleuferus [51]. Both demonstrated the necessity of a proper real gas EOS for a hydrogen jet at a high injection pressure $p_0 > 1 \times 10^7$ Pa. Their results underlined the necessity of a proper fluid property approximation for their cases. Similarly, Khaksarfard et al. [64] studied the high pressure release of a hydrogen storage tank. They used the Beattie-Brideman equation and the Abel-Noble equation and discussed the differences to the ideal gas formulation. Again, large differences were

observed in terms of accuracy, but also in stability of the simulation. This empasizes the importance, but also the challenges with incorporation of a nonlinear EOS. Pini et al. [94] used a look-up table to represent the real gas approximation. Their investigation comprised an accuracy analysis of the EOS and demonstrated the usability for CFD of turbine cascades.

1.2.2. Cavitation

The process of cavitation, i.e., volume filled with vapor in a local low pressure region in a liquid flow, can be observed in natural and many industrial applications. In nature the snapping shrimps use cavitational shock waves to stun or kill prey animals [75, 126]. Cavitation can also occur in trees [30], at the fins of dolphins [71] or in cracking joints [125]. In the industry cavitation is present in many application with liquids, e.g., ship propellers [26], diesel injection [90], turbines [69], and has been observed and studied intensively.

Early observations date as far back as to Sir Isaac Newton in 1704, however, he did not provide an explanation for the observation [124]. In 1754 Leonard Euler explained the physical background of cavitation and concluded that it might occur in turbines [116], this assumption was proven true. First publications of cavitation were published for the generation of vapor bubble at ship propellers and the resulting decrease in efficiency [138]. One of the first Finite Volume (FV) applications for cavitation was published by Iben et al. [62]. Since these first approaches, a vast number of different instigations have been done. Some examples of the investigated areas are analytical assessment of the collapse bubbles [47, 96, 97, 106], the analysis of cavitation erosion [82, 86, 93, 108] and highly resolved LES simulation of turbulent cavitational flows [37, 48, 49, 59, 113, 133].

A number of studies have been dedicated to accurately predict the collapse behavior of single bubbles and clouds of bubbles. Philipp and Lauterborn [93] investigated the movement of a bubble during the collapse for different wall distances. One of their key findings was that for certain distances of the initial wall distance the first collapse or with greater distance the second collapse, i.e., rebound, occur directly at the wall. Hence, the damage potential of such collapses is high.

Koch et al. [66] used a FV with a Volume Of Fluid (VOF) method to simulate the collapse behavior of a single bubble. The investigation included bubble collapses without a wall and close to a wall. Their findings were in good agreement with experimental data. Schmidt et al. [105] focused on the grid convergence of bubble cloud collapses. The findings demonstrated that for the used thermodynamic equilibrium model no grid convergences for the maximum pressure is present. On the other hand, the maximum wall pressure reaches a point of convergence. These findings show that with this type of model erosion prediction is feasible.

Different methods have been proposed in the literature to solve cavitational flows for

larger systems or components. Berg et al. [16] presented a model to predict homogeneous cavitation in a 1D gas-liquid pipe flow. In a number of test cases the model showed good agreement with analytical and experimental results. For the proposed cavitation model the compressible Euler equation was solved with the Lax-Friedrich (LF) Riemann method. The thermodynamic model for the evaporation assumes constant entropy during the process.

Dittakavi et al. [33] simulated a cavitating venturi throat with a sixth order compact Finite Difference (FD) scheme. The authors treated the stiffness problem of the simulation with an artificial increase of the Mach number (Ma). The test case of the water hammer displayed recognizable differences. Due to a vast decrease in computation time and focus on the cavitation-turbulence interaction the error was neglected. The authors further pointed out, that the vapor production suppresses the turbulence production at the throat and the collapse of the vapor contributes to the vorticity production. Salvador et al. [104] investigated a diesel injection with a Large Eddy Simulation (LES) solver. The authors used a Homogeneous Equilibrium Model (HEM) with a bartriopic EOS to model the cavitation. The differences of the mass flow, momentum flux and effective velocity compared to experimental data were about 10% for different operating points. The investigation showed a choking effect due to cavitation. The highest values of vorticies occurred at the liquid vapor interphase, therefore the authors concluded that the cavitation increases the turbulence level. Gnanaskandan and Mahesh [49] performed simulations of a flow over a wedge for which sheet cavitation is generated. The simulations were compared to experimental results of Ganesh [43,44]. The results were in good agreement with each other. Further, they showed that overall LES had better agreement to the experiment than Unsteady Reynolds-Averaged Navier-Stokes (URANS) calculations.

1.2.3. Thermodynamic Properties of Fluids

In most applications where some sort of fluid is involved, its thermodynamic properties are needed, e.g., to close governing equations and the representation of its attributes. The required accuracy, range of availability, e.g., pressure and temperature range, and accessibility, i.e., efficiency to obtain the properties, vary greatly with the application. In the past often simple look-up tables were sufficient, e.g., VID-Wärmeatlas. With the increasing popularity of simulations and especially CFD, which require to evaluate multiple data points, analytical equations and EOS libraries have been used more often. A number of different classes are available in the literature: ideal gas equation, cubic equations, Tait equations and relations based on thermodynamic potentials. Depending on the application and available computational resources either of those is sensible. The most accurate, however, computationally most expensive EOS approximations are based on the thermodynamic potentials. From this class, the Helmholtz free energy based formulations are the most widely used. The Helmholtz free energy formulation is valid over

a wide range of the fluid and is the state-of-the-art approximation of the fluid properties for many fluids. One of the most prominent examples is the approximation for water, which is defined in the International Association for the Properties of Water and Steam (IAPWS) standard [131]. For this the error margin of uncertainties is very low compared to other formulations, e.g., for specific volume the highest uncertainty is 0.3%. Several EOS evaluation programs are available which are based on the Helmholtz energy, e.g, RefProp [74], CoolProp [15], FPROPS [1] and FLUIDCAL [130].

1.3. Objective

The objective of this work is to demonstrate the capabilities of a high order scheme, DGSEM, and the usage of a highly accurate multiparameter EOS. A number of test cases are presented, including 1D shock tube experiments with real and ideal gas approximation, supersonic real gas jet simulation, single bubble cavitation collapses and micro channel flows with cavitation. These cases demonstrate on the one hand the capabilities of the proposed framework, i.e., low dissipation scheme coupled with accurate accurate EOS in a efficient manner, and give further insides and advice of the simulation with real gas properties on the other hand.

1.4. Outline

In this work, the application of a high order DG scheme with a tabulated EOS is presented. In Chapter 2 the fundamentals and background of the fluid flow are briefly summarized. Based on the compressible Navier-Stokes Equations (NSE) different EOS and the concept of the two-phase region are introduced. The fundamentals of supersonic flows and cavitation are assessed in Section 2.5 and Section 2.6, respectively. Chapter 3 addresses the background of the applied numerics. First, the applied numerical schemes, e.g., DG and FV, are briefly introduced. Section 3.2 to Section 3.4 cover the shock capturing, the applied Riemann solver and the de-aliasing in this work, respectively. The usage of the tabulated EOS is explained in Section 3.5 and the efficiency is evaluated. In the last subsection of this chapter, Section 3.6, the modeling of the multiphase flow is briefly discussed and the limitations of the used methods are summarized.

The results are divided into two chapters, gaseous flow and cavitation, Chapter 4 and Chapter 5, respectively. In Section 4.1 a shock tube experiment is carried out and the differences between ideal and real gas approximations for methane are discussed in detail. Section 4.2 first validates a simulation of a subsonic real gas jet and then analyzes the real gas effects of a supersonic jet in detail. In Section 5.1 a detailed parameter study for a bubble collapse is carried out, e.g., grid convergence and the influence of wall distance and vapor fraction. A micro channel flow is assessed in Section 5.2 to underline

the potential of the coupling of the DG with the tabulated EOS. In Chapter 6 the results of the present work are summarized and an outlook on research strategies is given.

In the present work, the standard notation for thermodynamic processes is used, e.g., subscripts of gradients or thermodynamics paths denote the constant property. For spacial coordinates $\vec{x}$ or velocity $\vec{w}$ an over-set with an arrow is used. Vectors of the governing equations are denoted with bolt letters, e.g., $\mathbf{U}$. For matrix with the dimensions of the spatial and the governing equations bolt letter with an over-set arrow are used. 3×3 - matrices quantities such as the stress tensor $\underline{\tau}$ are underlined. To distinquishe between the physical and the reference space for the DGSEM, the reference space quantities are written in calligraphy, e.g., $\vec{\mathbf{F}}$ for the flux in the physical space and $\vec{\boldsymbol{\mathcal{F}}}$ in the reference space.

1.4.1. Contributions of other authors

In Section 4.2 part of the results were published to the "Journal Computers and Fluids" under the title "Simulation of real gas effects in supersonic methane jets using a tabulated equation of state with a discontinuous Galerkin spectral element method" [52] and in the "High Performance Computing in Science and Engineering '16" under the title "Real-Gas Jet and Throttle Flows at High Pressure as Simplified Gas Injector Models with a Discontinuous Galerkin Method" [53]. The corresponding figures and tables have been cited accordingly (Figures 4.10, 4.12 to 4.17 and 4.19 to 4.22, Section 4.2.2, and Tables 4.3 and 4.4). For this content the co-authors have contributed to the published work and hence, to the results presented in the present thesis. While all co-authors have contributed with comments and helped with fruitful discussion, namely two have contributed in form and content to the results reproduced in this thesis. First, Dipl.-Ing. Malte Hoffmann contributed with further improvements to the applied numerical framework and separately published his findings in [57]. Second, Dr. rer. nat. Sebastian Boblest contributed to post-processing of the results, an example can be found in [17]. Further, part of the results in Section 5.1 have been published in similar form in [81]. This Master thesis was supervised and supported by the author of the present work.

2. Fundamentals

In the present work, the fundamentals and methodology are separated into two main chapter. This chapter provides the basis for the theoretical framework of this work. The governing compressible NSEs and a fundamental discussion of the approximation of fluid properties are presented. Further, supersonic gaseous flows and cavitation are briefly introduced. In the methodology chapter numerical methods used to describe the phenomena in the fundamentals chapter are presented and reasoning for the made choices are given.

2.1. Compressible Navier-Stokes Equations

The NSEs describe the motion for a compressible, viscous, heat-conducting fluid [109]. In this thesis the expression NSE is used as done commonly in numerical fluid mechanics. This was that the continuity equation of the energy equation are included when we speak of NSE. For spacial coordinates an over-set with an arrow is used and the vectors of the NSEs are denoted with bolt letters. A matrix consisting of the NSEs in all spatial dimensions are in bolt letter over-set with an arrow. In their conservative formulation they consist of the conservation of mass, momentum and energy and can be written as:

$$\mathbf{U}_t + \vec{\nabla}_x \cdot \vec{\mathbf{F}}(\mathbf{U}, \vec{\nabla}\mathbf{U}) = 0, \tag{2.1}$$

where $\mathbf{U}$ denotes the vector of conservative quantities

$$\mathbf{U} = \begin{pmatrix} \rho \\ \rho w_1 \\ \rho w_2 \\ \rho w_3 \\ \rho e \end{pmatrix}, \tag{2.2}$$

where the first, second to fourth and fifth entry denote the mass, momentum and energy term, respectively. $\vec{\nabla}\mathbf{U}$ is a tensor for which the divergence is applied line by line. The flux $\vec{\mathbf{F}}(\mathbf{U}, \vec{\nabla}\mathbf{U}) = \vec{\mathbf{F}}^{\mathrm{A}}(\mathbf{U}) - \vec{\mathbf{F}}^{D}(\mathbf{U}, \vec{\nabla}\mathbf{U})$ consists of the advection flux $\vec{\mathbf{F}}^{\mathrm{A}}(\mathbf{U})$ and

the diffusive flux $\vec{\mathbf{F}}^D(\mathbf{U}, \vec{\nabla}\mathbf{U})$. The advection flux is given as

$$\mathbf{F}_i^{\mathrm{A}}(\mathbf{U}) = \begin{pmatrix} \rho w_i \\ \rho w_1 w_i + \delta_{1i} p \\ \rho w_2 w_i + \delta_{2i} p \\ \rho w_3 w_i + \delta_{3i} p \\ \rho e w_i + w_i p \end{pmatrix} \tag{2.3}$$

and the diffusive flux as

$$\mathbf{F}_i^{\mathrm{D}}(\mathbf{U}, \vec{\nabla}\mathbf{U}) = \begin{pmatrix} 0 \\ \tau_{1i} \\ \tau_{2i} \\ \tau_{3i} \\ \tau_{ij} u_j - q_i \end{pmatrix}, \tag{2.4}$$

with the indices $i, j = 1, 2, 3$ denoting the spatial orientation. The physical quantities are ρ, $\vec{w} = (w_1, w_2, w_3)^T$, p and e representing the density, the velocity vector, the pressure and the specific total energy, respectively. Density, pressure and the static temperature colligate by an EOS. EOSs are discussed in further detail in Section 2.2.
The shear-stress tensor $\underline{\tau}$ for a Newtonian fluid, which is assumed to be correct for the applied fluids in the present work, can be written as:

$$\underline{\tau} := \eta \left(\vec{\nabla}_x \vec{w} + \left(\vec{\nabla}_x \vec{w} \right)^T - \frac{2}{3} \left(\vec{\nabla}_x \cdot \vec{w} \right) \underline{I} \right), \tag{2.5}$$

where η is the dynamic viscosity. The dynamic viscosity is the momentum exchange between the molecules with a different bulk velocity. For a number of ideal gas simulations the change in dynamic viscosity is neglected or a function of the temperature (Sutherland's law). For the present work, this assumption is not valid for the investigated flows.

In the diffusive flux (Equation (2.4)) $\vec{q}$ denotes the conductive heat flux leaving the fluid element. By assuming the Fourier heat conduction relationship the heat conduction may be written as:

$$\vec{q} = -\lambda \vec{\nabla}_x T, \tag{2.6}$$

where the thermal conductivity λ varies with pressure and temperature.
To close the NSE and obtain fluid properties, i.e., dynamic viscosity and heat conductivity, the fluid needs to be represented adequately. For example, an air flow with low Ma, i.e., dimensionless ratio of flow velocity $\vec{w}$ to the local speed of sound a, and at moderate temperatures and pressures, i.e., around the Standard Ambient Temperature and

Pressure (SATP), the ideal gas approximation with constant transport properties leads for most cases to very accurate results. However, for a similar scenario with Ma > 1 the change of transport properties with temperature might be important to approximate. Considering a fluid flow with phase changes, e.g., cavitation of a liquid, the EOS and transport properties should be approximated by complex multiparameter equations. The different levels of simplification are discussed in the following sections.

2.2. Equation of states

To close the NSEs, i.e., to connect the density and temperature to the pressure, an EOS is needed. For viscous flows additionally the transport properties are required, i.e., dynamic viscosity and thermal conductivity (see Section 2.4). The fluid properties of gases are often categorized. To categorize the fluid properties the compressibility factor Z

$$Z = \frac{p}{\rho R T}, \tag{2.7}$$

the specific heat capacity at constant pressure

$$c_{\mathrm{p}} = \left(\frac{\partial h}{\partial T}\right)_p \tag{2.8}$$

and the specific heat capacity at constant volume

$$c_{\mathrm{v}} = \left(\frac{\partial u}{\partial T}\right)_v \tag{2.9}$$

are used.

For a perfect gas or a calorically perfect the compressibility factor is always $Z = 1$ and c_p and c_v only depend on the fluid type and not on the pressure or temperature. For an ideal gas or thermally perfect gas all fluid properties are independent of pressure, but vary with temperature and the fluids, i.e., $Z = 1$, $c_p\left(T, \text{fluid}\right)$ and $c_v\left(T, \text{fluid}\right)$. Consequently, for a real gas the fluid properties depend on pressure, temperature and is different for different fluids, i.e., $Z\left(p, T, \text{fluid}\right)$, $c_p\left(p, T, \text{fluid}\right)$ and $c_v\left(p, T, \text{fluid}\right)$. A summary is given in Table 2.1. Note that in the two-phase region p and T do not clearly determine the state of the fluid. Hence, here an additional parameter is required.

Whilst this gives a brief classification of the fluid type, each class could be approximated with different levels of accuracy. In the following, a brief overview of different approximations is given. The given examples are not a complete list, but aim to give a basic understanding of the most commonly used ones. The interested reader is refereed to Baehr and Kabelac [10] amongst other fundamental literature for a more detailed discussion.

Table 2.1.: Distinction between perfect, semi-perfect, ideal and real gas.

	perfect calorically perfect	ideal thermally perfect	imperfect real
Z	1	1	$Z(p,T)$
c_p	const.	$c_p(T)$	$c_p(p,T)$
c_v	const.	$c_v(T)$	$c_v(p,T)$
$\kappa = \frac{c_p}{c_v}$	const.	$\kappa(T)$	$\kappa(p,T)$
ideal gas laws	yes	yes	no

2.2.1. Ideal gas law

Here, the idea is that the distance of the gas molecules is large enough so that forces of attraction and repulsion can be neglected. The pressure can be derived from T and ρ

$$p = \frac{RT}{v} = \rho RT = (\kappa - 1)\,\rho c_v T. \tag{2.10}$$

Further, for an ideal gas the specific thermal capacities, c, and the specific gas constant, R, have a direct relation.

$$R = c_p - c_v \tag{2.11}$$

The isentropic coefficient, κ, for an ideal gas is directly related to the ratio of the specific thermal capacities

$$\kappa = \frac{c_p}{c_v} \tag{2.12}$$

and is often used to characterize changes of thermodynamic properties in shocks or expansions. An example for the expansion wave is given in Section 4.1 in further detail.

Further, due to the simplicity of the ideal gas law, temperature is only a function of the specific inner energy u. For constant c_v one obtains:

$$T = \frac{\kappa - 1}{R} u. \tag{2.13}$$

Similarly, the speed of sound, a, can directly be derived from the temperature and can be expressed as

$$a = (\kappa RT)^{\frac{1}{2}}\,. \tag{2.14}$$

These equations are all relatively simple and are not complex to implement into a fluid dynamics solver. Therefore, where appropriate ideal gas EOS approximation is desirable. However, the range of validity is very limited, e.g, it is not applicable for the liquid state or at high pressures.

2.2.2. Tait equation

For the representation of the liquid state of a fluid a relatively simple expression is the Tait equation. The Tait equation is widely used to represent the equation of state of a compressible liquid [35, 63] in the compressible regime. It reads

$$v\left(p\right) = \rho_0^{-1}\left[1 + C\ln\left(\frac{p+B}{p_0+B}\right)\right], \tag{2.15}$$

where ρ_0, B and C can be chosen as constants. The constants can be replaced with temperature dependent functions, i.e.,

$$\rho_0\left(T\right) = \sum_{i=0}^{3} a_i T^i, \tag{2.16}$$

$$B\left(T\right) = \sum_{i=0}^{2} b_i T^i \quad \text{and} \tag{2.17}$$

$$C\left(T\right) = \sum_{i=0}^{1} c_i T^i, \tag{2.18}$$

where the constants a_i, b_i and c_i are derived from fits to experimental data.

The Tait equation can be fitted to a number of fluids, e.g., water, normafluid ISO 4113 [29] or others and yields good results. However, it is only applicable to the liquid phase. In applications where only the liquid phase is relevant it is widely used [35].

2.2.3. Cubic equations of states

Another class of EOS are the cubic formulations. With this class of EOS the complete fluid range can be approximated in an efficient manner. Here, only a few experimental data points are necessary to fit the coefficients [10]. These equations account for the forces of attraction and repulsion and were first proposed by van der Waals in 1873 [115]. Current state of the art cubic EOS are the Redlich-Kwong [101], Soave-Redlich-Kwong [110], and the Peng-Robinson [91] equations of state. In the present work, only the Peng-Robinson equation of state is presented in more detail. The interested reader is referred to Baehr and Kabelac [10] for a detailed analysis of a general cubic EOS [9].

A common expression for the Peng-Robinson equation is

$$p = \frac{RT}{V_m - b} - \frac{a\alpha}{V_m^2 + 2bV_m - b^2} \tag{2.19}$$

with

$$a = \frac{0.4572R^2T_c^2}{p_c} \tag{2.20}$$

and

$$b = \frac{0.07780 R T_c}{p_c}, \tag{2.21}$$

where V_m denotes the molar volume, T_c the critical temperature and p_c the critical pressure of the fluid. The expressions for a and b account for the attraction between particles and their volume, respectively. The correction term α can be expressed as

$$\alpha = \left(1 + \left(0.3746 + 1.542\omega - 0.2699\omega^2\right)\left(1 - T_r^{0.5}\right)\right)^2, \tag{2.22}$$

where $T_r = T/T_c$ is the reduced temperature and ω is an acentric factor. The acentric factor accounts for the non-sphericity of molecules [95].

2.2.4. Helmholtz free energy formulation

Further, many of the most accurate multiparameter EOS are expressed with a thermodynamic potential. Some examples of such potentials are inner energy, enthalpy, Helmholtz energy or Gibbs energy [103]. Span [114] showed that a formulation from the specific Helmholtz free energy, f, is the most practical, i.e., the fundamental variables ρ and T are easy to obtain and allow for a thermodynamically defined state for all fluid phases.

In the present work, the fluid data for the multiparameter real fluids are obtained from CoolProp, an OpenSource fluid library [15]. Fluid data from this library is also based on the specific Helmholtz free energy formulation. The coupling with the used numerical framework is later discussed in section 3.5.

The Helmholtz free energy in its dimensionless form, $\phi = f/(RT)$, can be expressed as

$$\frac{f(\rho, T)}{RT} = \phi(\delta, \tau) = \phi^0(\delta, \tau) + \phi^{\mathrm{r}}(\delta, \tau), \tag{2.23}$$

where ϕ^0 and ϕ^{r} are an ideal-gas and a residual part, respectively. The split of the equation in ideal-gas and residual part is done to reduce the complexity of the used terms. By slitting them up it is possible to fit the different parts individually. Without the split very complex functional forms, as used today, would be unfeasible for practical use [114]. With the use of reference constants, here the critical values of density ρ_c and temperature T_c and the specific gas constant R, $\delta = \rho/\rho_c$ and $\tau = T/T_c$ are given. The expressions of the ideal-gas part of the Helmholtz energy and especially the residual part can be very complex. To illustrate this the expressions of ϕ^0 and ϕ^r for water without the constants are shown in the following. The complete definitions can be found in Wagner and Pruß [131].

The reference constants for water are $T_c = 647.1\,\mathrm{K}$, $\rho_c = 322\,\mathrm{kg\,m^{-3}}$ and $R = 0.4615\,\mathrm{kJ\,kg^{-1}\,K^{-1}}$. The ideal-part of the Helmholtz free energy was developed by

Cooper [31] and can be written as

$$\phi^0 = \ln\delta + n_1^0 + n_n^0\tau + n_3^0 \ln\tau + \sum_{i=4}^{8} n_i^0 \ln\left[1 - e^{-\gamma_i^0 \tau}\right], \tag{2.24}$$

where n_i^0 are adjustable coefficients, γ_i^0 are precorrelation factors, which are given in [131].

The residual part ϕ^r can be expressed as

$$\begin{aligned}\phi^{\mathrm{r}} = &\sum_{i=1}^{7} n_i \delta^{d_i} \tau^{t_i} + \sum_{i=8}^{51} n_i \delta^{d_i} \tau^{t_i} e^{-\delta^{c_i}} \\ &+ \sum_{i=52}^{54} n_i \delta^{d_i} \tau^{t_i} e^{-\alpha_i(\delta-\epsilon_i-)^2 - \beta_i(\tau-\gamma_i)^2} + \sum_{i=55}^{56} n_i \Delta^{b_i} \delta\Psi\end{aligned} \tag{2.25a}$$

with

$$\Delta = \Theta^2 + B_i\left[(\delta-1)^2\right]^{a_i}, \tag{2.25b}$$

$$\Theta = (1-\tau) + A_i\left[(\delta-1)^2\right]^{\frac{1}{2\beta_i}}, \tag{2.25c}$$

$$\Psi = e^{-C_i(\delta-1)^2 - D_i(\tau-1)^2}. \tag{2.25d}$$

where c_i and d_i are density exponents, t_i are temperature exponents, a_i, b_i, A_i, B_i, C_i, n_i, α_i, β_i and ϵ_i are adjustable coefficients and γ_i are pre-correlation factors, which are given in [131].

Other thermodynamic properties can be derived from Equation (2.23) with combination of ϕ^0, ϕ^r and their derivatives. Table 2.2 summarizes the thermodynamic properties, which are most relevant for the present work. A complete list can be found in [114].

2.2.5. Equation of state comparison

Having introduced a number of commonly used EOS, a brief comparison for two fluids is carried out, i.e., water and methane. For water the comparison is limited to the Tait equation, the ideal gas formulation and the Helmholtz free energy formulation. The density over pressure for water is presented in Figure 2.1a. At high pressures the Tait and the Helmholtz formulations have a similar trend, however show observable differences. The focus is here not on the difference at high pressure, which could result from the fits to different experiment data (fit from [39] for Tait and [131] for the Helmholtz formulation), but on the usability at low pressures. Here, the Tait equation is not representing the phase change and cannot be used for the gaseous phase. To use the Tait equation for the whole fluid regime it can be blended at low pressures to the ideal gas approximation, which has been done by Reboud et al. [100] for a barotropic model.

Table 2.2.: Relation of the thermodynamic properties to the dimensionless Helmholtz free energy (ideal and residual part) Equation (2.23) and their derivatives [114]. Here ρ and v are interchanged to remain a compact representation.

Property		Relation	
$p(\rho,T)$	$= -\left(\frac{\partial f}{\partial v}\right)_T$	$\frac{p(\delta,\tau)}{\rho RT}$	$= 1+\delta\phi^{\mathrm{r}}_\delta$
$u(\rho,T)$	$= f - T\left(\frac{\partial f}{\partial T}\right)_\rho$	$\frac{u(\delta,\tau)}{RT}$	$= \tau\left(\phi^0_\tau+\phi^{\mathrm{r}}_\tau\right)$
$h(\rho,T)$	$= u+pv$	$\frac{h(\delta,\tau)}{RT}$	$= 1+\tau\left(\phi^0_\tau+\phi^{\mathrm{r}}_\tau\right)+\delta\phi^{\mathrm{r}}_\delta$
$c_p(\rho,T)$	$= \left(\frac{\partial h}{\partial T}\right)_p$	$\frac{c_p(\delta,\tau)}{RT}$	$= -\tau^2\left(\phi^0_{\tau\tau}+\phi^{\mathrm{r}}_{\tau\tau}\right)+\frac{\left(1+\delta\phi^{\mathrm{r}}_\delta-\delta\tau\phi^{\mathrm{r}}_{\delta\tau}\right)^2}{1+2\delta\phi^{\mathrm{r}}_\delta+\delta^2\phi^{\mathrm{r}}_{\delta\delta}}$
$a(\rho,T)$	$= \left(\frac{\partial p}{\partial \rho}\right)_s^{\frac{1}{2}}$	$\frac{a^2(\delta,\tau)}{RT}$	$= 1+2\delta\phi^{\mathrm{r}}_\delta+\delta^2\phi^{\mathrm{r}}_{\delta\delta}-\frac{\left(1+\delta\phi^{\mathrm{r}}_\delta-\delta\tau\phi^{\mathrm{r}}_{\delta\tau}\right)^2}{\tau^2\left(\phi^0_{\tau\tau}+\phi^{\mathrm{r}}_{\tau\tau}\right)}$

$$\phi^{\mathrm{r}}_\delta = \left[\frac{\partial\phi^{\mathrm{r}}}{\partial\delta}\right]_\tau, \phi^{\mathrm{r}}_{\delta\delta} = \left[\frac{\partial^2\phi^{\mathrm{r}}}{\partial\delta^2}\right]_\tau, \phi^{\mathrm{r}}_\tau = \left[\frac{\partial\phi^{\mathrm{r}}}{\partial\tau}\right]_\delta, \phi^{\mathrm{r}}_{\tau\tau} = \left[\frac{\partial^2\phi^{\mathrm{r}}}{\partial\tau^2}\right]_\delta,$$

$$\phi^0_\delta = \left[\frac{\partial\phi^0}{\partial\delta}\right]_\tau, \phi^0_{\delta\delta} = \left[\frac{\partial^2\phi^0}{\partial\delta^2}\right]_\tau, \phi^0_\tau = \left[\frac{\partial\phi^0}{\partial\tau}\right]_\delta, \phi^0_{\tau\tau} = \left[\frac{\partial^2\phi^0}{\partial\tau^2}\right]_\delta$$

Similarly, in Figure 2.1b the approximation of density over pressure in the gaseous phase is shown for methane. At low pressures the ideal gas approximation is relatively accurate, however at higher pressure the neglect of compressibility effects leads to strong derivations. The Peng-Robinson equation on the other hand is capable to represent the real gas effects adequately, despite some differences to the Helmholtz formulation. Once the two-phase region is reached, the Peng-Robinson equation becomes invalid. Hence, from the proposed EOS the Helmholtz formulation is the only one, which represents the fluid for all phases with a high accuracy.

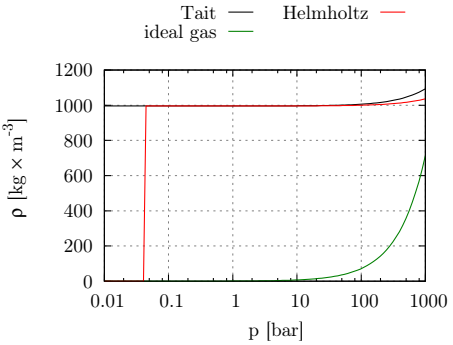

(a) Water

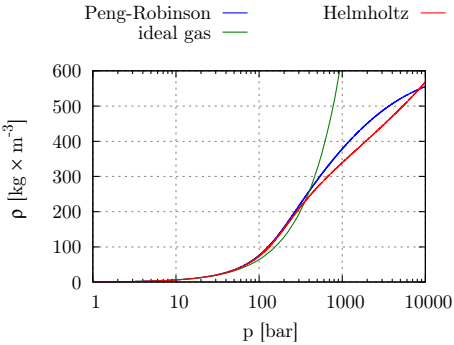

(b) Methane

Figure 2.1.: Comparison of different EOS approximations for water and methane at constant temperature $T = 300\,\mathrm{K}$.

2.3. Liquid vapor mixture region

In the present work, the liquid vapor mixture, or wet steam, region is discussed. Therefore, a few key aspects and considerations are given to the reader with a brief introduction of the topic and the arising challenges. A more details can be found in the literature [10, 115].

The thermodynamic process of phase change in the two-phase region for boiling is presented in Figure 2.2. A liquid (1) is heated at constant pressure. The temperature

increases until it reaches its boiling temperature (2) and a first steam bubble is generated. By adding additional heat more steam is generated at constant temperature and pressure. This process occurs in the wet steam region (3), until the last liquid droplet evaporates (4) and the steam is saturated. If the system is heated further, the temperature increases again and the steam is superheated and fully gaseous (5).

Similarly, Figure 2.3 illustrates the thermodynamic process of cavitation. A liquid (1) is expanded and constant temperature is assumed. When the vapor pressure is reached, a first steam bubble (2) is generated. By expanding the fluid further more and more steam is created (3), until the last liquid droplet evaporates (4). Afterwards only the gaseous phase is expanded (5).

In the present work, the liquid vapor mixture is assumed to be always in equilibrium. Hence, in a process as described above, both phases are assumed to be in a mixture state and in equilibrium. The fluid properties are obtained for the mixture. To give the reader more details on the properties of specific fluids, different fluid diagrams are presented in Chapter B.

2.3.1. Maxwell line reconstruction

As above, for an isothermal path through the two phase region in equilibrium the pressure remains constant. For a van der Waals type gas the theoretical isothermal path, however,

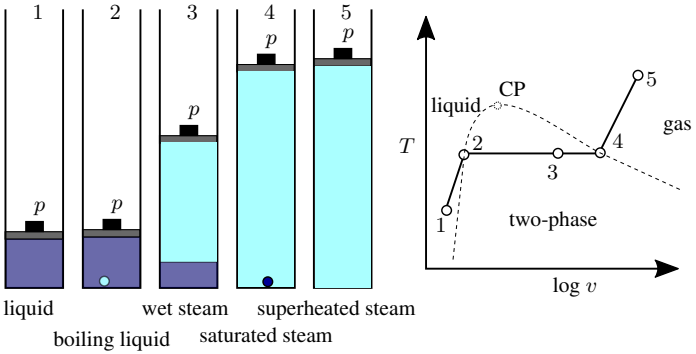

Figure 2.2.: Schematic of the thermodynamic path of boiling (cf. [10]).

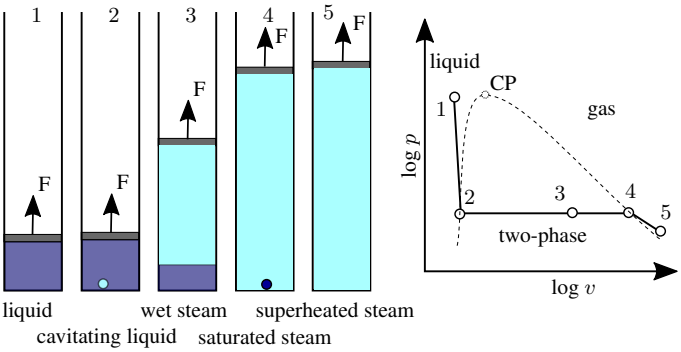

Figure 2.3.: Schematic of the thermodynamic path of cavitation.

is not isobar. Within the spinodale this would violate the stability criteria

$$\left(\frac{\partial p}{\partial v}\right)_T < 0, \tag{2.26}$$

see [10] for a derivation and results in a none homogeneous mixture. While a stable state outside the spinodale line would be possible in the present work the Maxwell line reconstruction is applied. Therefore, the states within the two phase region are always limited to an equilibrium state.

2.3.2. Vapor mass and vapor volume fraction

For fluids generally two variables are used to characterize the position on such a line within the two phase region, the vapor mass x and the vapor volume fraction α. Both values range from 0 to 1, from liquid to vapor, respectively. The vapor mass fraction x can be written as

$$x := \frac{m''}{m' + m''}, \tag{2.27}$$

where m' denotes the liquid mass and m'' the vapor mass of mixture. The vapor mass fraction is often used to scale fluid properties inside the two phase region with a lever principle, e.g., enthalpy or entropy.

The vapor volume fraction

$$\alpha := \frac{V''}{V' + V''} = \frac{\rho''(T) - \rho}{\rho''(T) - \rho'(T)}, \tag{2.28}$$

with V' as the liquid mass and V'' as the vapor mass of mixture and ρ' and ρ'' denote the density at saturated gas and liquid line, respectively. It is proportional to the density and therefore, straight forward obtainable from experiments, e.g., x-ray measurements [44].

Both of these values can be found in the literature and are used in the present work. Consequently, it is important to interpret these values correctly, since they can have significant differences. For example, a very high value of $\alpha = 0.999$ might result in a low value in $x = 0.1$ for water at 330 K.

2.3.3. Speed of Sound

The definition of the speed of sound for different EOS approximations has been discussed prior. However, the behavior of the speed of sound, a, in the two phase regions is of great importance and discussed in more detail in the following. While for an ideal gas the definition is rather simple Equation (2.14), the definition for the Helmholtz formulation becomes more complex. Generally, a sound wave is a periodic pressure and density fluctuation with a small amplitude. By assuming that the process is isentropic this propagation speed can be written as [10]

$$a\left(\rho, T\right) = \left(\frac{\partial p}{\partial \rho}\right)_s^{\frac{1}{2}}. \tag{2.29}$$

It can further be transformed into isothermal and isochoric expressions

$$a^2 = -v^2 \left(\frac{\partial p}{\partial v}\right)_s = v^2 \left[\frac{T}{c_v}\left(\frac{\partial p}{\partial T}\right)_v^2 - \left(\frac{\partial p}{\partial v}\right)_T\right] \tag{2.30}$$

$$= -v^2 \left(\frac{\partial p}{\partial v}\right)_T \frac{c_p}{c_v} = \left(\frac{\partial p}{\partial \rho}\right)_T \frac{c_p}{c_v}. \tag{2.31}$$

And for an ideal gas this expression be used to derive the speed of sound in Equation (2.14):

$$p = \rho R T \tag{2.32}$$

$$\left(\frac{\partial p}{\partial \rho}\right)_T = RT \tag{2.33}$$

$$a^2 = RT\frac{c_p}{c_v} = \kappa R T \tag{2.34}$$

In a mixture a decreases, dependent on the pressure, below the speed of sound of the mixture components [65], e.g., liquid-gas or air-water mixture. The time scales of the pressure waves within this region are orders of magnitudes lower than in the liquid and even in the pure gaseous region.

2.4. Transport properties

To solve the diffusive part of the NSEs the transport properties μ and λ are needed. For those a number of different approximations are possible and used. For the present work, a brief summary is given.

2.4.1. Viscosity

In the present work, the viscosity is limited to Newton fluids, i.e., the viscose stresses are linear functions of the strain rates. For an ideal gas the dynamic viscosity is consider as constant

$$\mu = \text{const.} \tag{2.35}$$

If the fluid needs to consider the change of viscosity with temperature, which might be appropriate for shocks, the Sutherland formulation is often used

$$\mu = \mu_{\text{S}} \frac{T_{\text{S}} + S}{T + S} \left(\frac{T}{T_{\text{S}}} \right)^{\frac{3}{2}}, \tag{2.36}$$

where the index S indicates the reference states and S is the Sutherland temperature. With this expression the variation due to a change in temperature can be well approximated. However, this is only the case at lower pressures. For example, methane are at pressures higher than 100 bar the viscosity is inversely proportional to the change in temperature and strongly depends on pressure, see Figure 4.12.

More complex dynamic viscosity approximations can also be described with the Helmholtz free energy formulation. Again, water is used to illustrate this kind of formulation as stated by Huber et al. [61]. For the dynamic viscosity the approximation consists of three parts: temperature dependent μ^0, temperature and density dependent μ^r and a correction term close to the critical point μ^c:

$$\mu = \mu^0(\tau)\mu^{\text{r}}(\tau, \delta)\mu^{\text{c}}(\tau, \delta) \tag{2.37}$$

However, it is recommended for industrial applications to neglect μ^c to increase computation speed.

2.4.2. Thermal Conductivity

For an ideal gas the thermal conductivity can be expressed as

$$\lambda = \frac{R\mu}{1 - \frac{1}{\kappa}\mathrm{Pr}}, \tag{2.38}$$

where $\mathrm{Pr} = \frac{\mu c_\mathrm{p}}{\lambda}$ is the dimensionless Prandtl number. It is a dimensionless number, which denotes the ratio of momentum to the thermal diffusivity. For most fluids Pr is known in the ideal gas regime, e.g., at $T = 273.15\,\mathrm{K}$ and $p = 1\,\mathrm{bar}$: $\mathrm{Pr}_\mathrm{air} = 0.7108$ and $\mathrm{Pr}_{\mathrm{CH}_4} = 0.7365$.

An expression based on Equation (2.23) was described in [60]

$$\lambda = \lambda^0(\tau)\lambda^\mathrm{r}(\tau, \delta) + \lambda^\mathrm{c}(\tau, \delta), \tag{2.39}$$

where similar to Equation (2.37), the superscript denotes different terms, i.e., the ideal, the residual and the critical point correction terms. In contrary to the viscosity, the critical enhancement cannot be neglected, even well away from the critical point and needs to be considered. Therefore, Huber et al. [60] suggest for industrial purposes to replace λ^c with a simpler expression without significant increases in the approximation error.

2.5. Supersonic gas dynamics

Having introduced the general properties of a moving fluid and its properties, an important and also challenging flow regime - the supersonic flow - is introduced in the following. Supersonic flows, i.e., $\mathrm{Ma} > 1$, are of great importance for many gas dynamics applications. In aerospace, gas turbines, automotive gas injection and many other areas an understanding of supersonic flow is essential to develop proper components and products. To continue the above discussion about ideal and real gas, in many applications it is sufficient to consider the gas as ideal. However, for a DGI of an internal combustion engine the pressures are high enough, so real gas effects need to be taken into account.

2.5.1. Shock waves for ideal and real gases

A supersonic flow is often associated with the presence of shocks. Large pressure gradients steepen into shock waves. Shock waves, in contrast to sound waves, are nonlinear waves and change the state of the medium. First, the difference between a sound wave and a shock wave is shown. Figure 2.4 illustrates the difference of shock and sound waves in terms of a change in pressure p, specific volume v and entropy s. From its initial state (1), the gas oscillates during a sound wave along the constant entropy line S_1. For a normal shock wave the pressure, density and entropy increase from (1) to (4). The connecting curve is called Hugoniot curve. After the shock the pressure decreases on an

adiabatic passage to its initial pressure (5). Temperature and entropy are higher than before and consequently the specific volume has increased. A shock front is non-adiabatic and irreversible.

For a better understanding the change of thermodynamic properties across a normal shock is discussed for a perfect and real gas as proposed by Rist [102]. The indexes 1 and 2 denote the states before and after the shock, respectively. The total enthalpy h_t is assumed to be unchanged across the shock for both perfect and real gas, because the shock thickness is assumed to be negligible. For a perfect gas the total temperature T_t remains constant, too. However, a real gas experiences a drop in T_t across the shock. The temperature and pressure rise across the shock is higher for the real gas than for a prefect gas. Further, the drop in total pressure p_t and velocity w is greater for the real gas than for the ideal gas. A summary for the changes in thermodynamic properties across a normal shock is given in Table 2.3.

2.5.2. Supersonic jet

In the present work, a supersonic underexpanded jet is analyzed under real gas conditions. Therefore, to keep this work self-contained a brief introduction is given. A circular

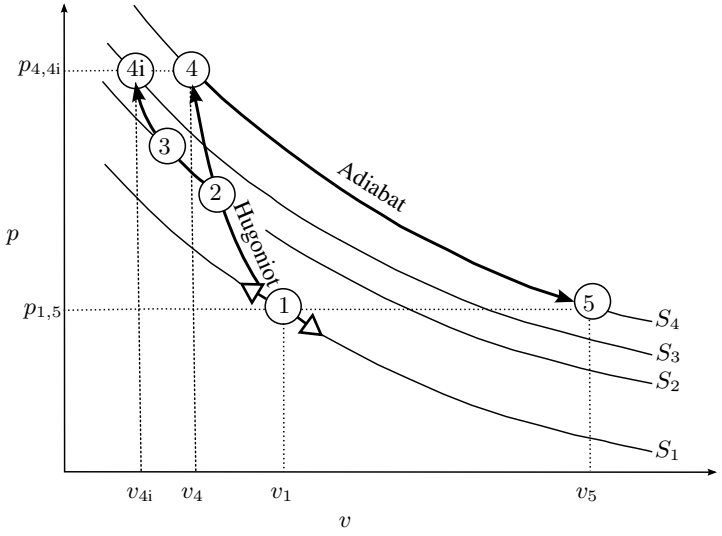

Figure 2.4.: Passage of a sound and shock wave (adapted from Norman et al. [87]).

Table 2.3.: Change of the thermodynamic properties across a normal shock for a perfect and real gas.

	perfect gas	real gas
h_{t1}	$= h_{t2}$	$= h_{t2}$
T_{t1}	$= T_{t2}$	$> T_{t2}$
T_1	$< T_2$	$< T_2$
p_{t1}	$> p_{t2}$	$> p_{t2}$
p_1	$< p_2$	$< p_2$
w_1	$> w_2$	$> w_2$

supersonic jet can be characterized by its state of expansion. The pressure ratio of pressure at the nozzle orifice p_n and the ambient pressure p_a indicates the different states; pressure matched $p_n/p_a = 1$, underexpanded $p_n/p_a > 1$ or overexpanded $p_n/p_a < 1$. The features of a supersonic jet are explained by means of a highly underexpanded jet (see Figure 2.5). The interested reader is referred to Norman and Winkler [87] for a more detailed description of other expansions states.

For an underexpanded jet the boundaries oscillate due to the attempt of the gas to reach ambient pressure. For a higher pressure ratio an incident shock forms instead of crisscrossed shock waves. A so-called shock triple point is present, at which incident shock, reflected shock and Mach disk meet. In Figures 2.4 and 2.6 for path (1) to (4) the gas is expanded more than for path (1) to (2) and (3) to (4i). As a result a slip discontinuity forms. Further, the local Ma number fluctuates between super- and subsonic

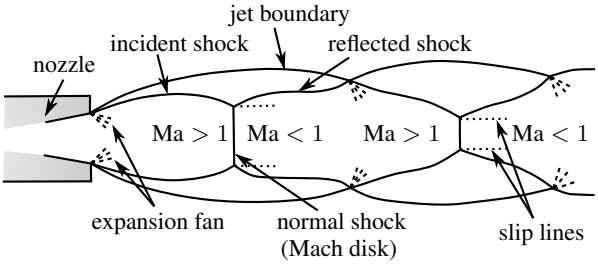

Figure 2.5.: Schematic of a highly underexpanded nozzle jet (cf. [88]).

conditions within the jet. In front of a shock the fluid accelerates gradually due to the lower ambient pressure and across the shock the Ma number drops abruptly to subsonic conditions.

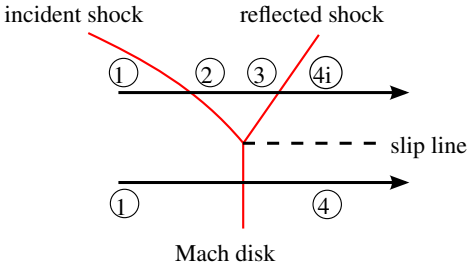

Figure 2.6.: Path through a normal and incident shock with slip discontinuity.

2.5.3. Noise sources in supersonic jets

Noise emitted by supersonic jets is important for many applications. The noise emitted by a supersonic jet has three major contributors: turbulent mixing noise, broadband shock-associated noise and screech tones [117]. Turbulent mixing noise is most dominant downstream of the jet. Large and small scale turbulent structures are responsible for the noise generation [118]. In a more upstream position the broadband shock-associated noise is the dominant noise source and further upstream screech is the most dominant source and it is a very disturbing sound. Detailed discussions on supersonic jet noise for fully- and underexpanded jets can be found in Tanna [120, 121] and Tam [117].

While acoustics are an important topic of supersonic jets, the present work does only briefly discuss possible implications of acoustics. Nonetheless, the CFD solver of the present work has been assessed for supersonic jet noise with very good agreement to experimental data [54].

2.6. Cavitation

In the prior section, supersonic gas dynamics with the focus on supersonic flows have been introduced. In the following, multiphase flow with the focus on cavitation are assessed. Cavitation is a complex phenomena which occurs in nature [30, 126, 138], medicine [23, 73] and industrial application [16, 108]. A fluid flow with cavitation is always highly transient, i.e., the generation and collapse of vapor regions is in the order

of nano and micro seconds and within very small spatial scale. Further, the difference in density or speed of sound (cf. Section 2.3.3) can also be orders of magnitude across a very small spatial scales. Pressure waves with a strong amplitude are emitted, due to the compressibility of the liquid during the rapid collapse process. These waves or shocks can be very strong and lead to high wall loadings which can potentially damage components.

To gain a fundamental understanding of cavitation a brief overview of a single cavitation bubble throughout its "life cycle" is given. For a more detailed discussion on cavitation the reader is refereed to Brennen [21], Brujan [23], Franc and Michel [41] and Young [138].

2.6.1. Nucleation

A pure liquid is capable of sustaining a certain amount of tension. This can be a stable state, as long as no vapor or small particles are present. However, homogeneous nucleation can occur at which small temporary gaps form due to the movement of the molecules. An other type of nucleation is caused by the interface between the liquid and solids, e.g. small particles or a surface in contact with the liquid. This is commonly referred to as heterogeneous nucleation. Other roots of "weaknesses" in the fluid can be small bubbles or radiation from the outside.

Due to the weaknesses the tension at which the formation of vapor bubbles occurs decreases. Here, two different types of phase changes are considered as illustrated in Figure 2.7. Heating the liquid at constant pressure is referred to as boiling if the vapor temperature is reached. The term cavitation is used when the local pressure decreases below the vapor pressure at the given temperature.

2.6.2. Inception

A common characterization of the likeliness of caviation to occur in a flow is the cavitation number

$$\sigma = \frac{2\left(p_\infty - p_v\right)}{\rho_l w_\infty^2}, \tag{2.40}$$

where p_∞ is the reference pressure, p_v is the vapor pressure at a reference temperature, ρ_l is the liquid density and w_∞ is a reference velocity. If σ is reduced to the point at which cavitation is present, then it is denoted as inception cavitation number σ_i. When cavitation actually occurs depends on a number of factors. Some of which are listed below [22]:

- ability of the liquid to sustain tension
- residence time

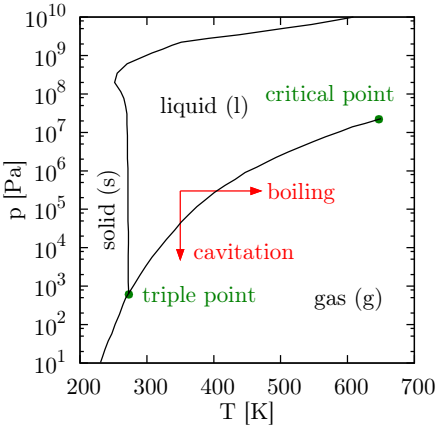

Figure 2.7.: Phase diagram for water (fluid data from [132]).

- local state of the liquid, since cavitation is highly transient phenomena and such correlations usually assume an averaged flow
- thermodynamic path, because of cavitation hysteresis, i.e., increase and decrease of throttle pressure ratios to the same operating point might lead to different flows [58]

A more detailed discussion of cavitation inception can be found in [21].

2.6.3. Growth and collapse

The Rayleigh-Plesset equation is often used to describe the bubble growth in a liquid. A spherical bubble with radius $r(t)$ as a function of time is considered in an infinite domain. The pressure and temperature in the far field are $p_\infty(t)$ and T_∞, respectively. In this context, ρ_l, T_∞ are assumed to be constant and uniform. Further, the pressure $p_B(t)$ and the temperature $T_B(t)$ inside the bubble are assumed to be homogeneous and uniform. With these assumptions a generalized Rayleigh-Plesset equation in the absence of thermal effects for the dynamics of a single bubble can be derived [97]

$$\frac{p_\mathrm{v}(T_\infty) - p_\infty(t)}{\rho_\mathrm{l}} + p_{\mathrm{g},0}\left(\frac{R_0}{r}\right)^{3k} = r\frac{\partial^2 r}{\partial t^2} + \frac{3}{2}\left(\frac{\partial r}{\partial t}\right)^2 + \frac{4\mu_\mathrm{l}}{\rho_\mathrm{l} r}\frac{\partial r}{\partial t} + \frac{2\gamma}{\rho_\mathrm{l} r}, \quad (2.41)$$

where γ is the surface tension and k a constant that represents the polytropic behavior. With $k = 1$ the bubble temperature remains constant and $k = \kappa$ represents an adiabatic behavior. A more detailed derivation and discussion can be found in the literature [21, 41, 97].

Based on Equation (2.41) the influence of the different terms, e.g, gas inside the bubble, viscosity effects and surface tension, for a collapse can be assessed. For the initial states of $T_\infty = 330\,\mathrm{K}$, $p_\infty = 1 \times 10^6\,\mathrm{Pa}$ the gas in the bubble has the most dominant effects. The collapse time and the minimum radius depend strongly on the gas inside the bubble, while the surface tension and the viscosity have only marginal influence. However, 3D collapses can not be described with the 1D approximation of the Rayleigh-Plesset expression, i.e., jet and shock wave are not included in the expression. A number of studies have been carried out concerning single bubble collapse experimentally and numerically [3, 47, 66, 72, 84, 93].

3. Methodology

3.1. Numerical schemes

The present work focuses on the Discontinuous Galerkin Spectral Elements Method (DGSEM). The DGSEM is a specific form of the Disontiuous Galerkin (DG) method.

3.1.1. Discontinuous Galerkin Spectral Elements Method

The DGSEM discretizes the compressible Navier-Stokes Equation (2.1)

$$\mathbf{U}_t + \vec{\nabla}_x \cdot \vec{\mathbf{F}}(\mathbf{U}, \vec{\nabla}\mathbf{U}) = 0, \tag{3.1}$$

which was introduced in Section 2.1. For the DGSEM the equation has to be transformed from the physical into a reference space. The notation used in Hoffmann et al. [57] is applied. In the physical space the cartesian coordinates x_1, x_2, x_3 and in the reference space $(\xi^1, \xi^2, \xi^3)^T$ are used. Therefore, the solution is mapped to a reference element $E \in [-1, 1]^3$ and back with a polynomial mapping function $\vec{x}(\vec{\xi})$. Based on this, a Jacobian is calculated $J(\vec{\xi}) = \det(\frac{\partial \vec{x}}{\partial \vec{\xi}})$.

From this definition of the transformation, the transformed NSE can be written as

$$\mathbf{U}_t + \frac{1}{J(\vec{\xi})} \vec{\nabla}_\xi \cdot \vec{\boldsymbol{\mathcal{F}}}(\mathbf{U}, \vec{\nabla}_x \mathbf{U}) = 0, \tag{3.2}$$

where $\vec{\nabla}_\xi = (\partial_{\xi^1}, \partial_{\xi^2}, \partial_{\xi^3})^T$ is the divergence operator in the reference space. Further the flux from the physical space $\vec{\mathbf{F}}$ is transformed into the reference space $\vec{\boldsymbol{\mathcal{F}}}$ and can be split into its inviscid and viscous parts $\vec{\boldsymbol{\mathcal{F}}} = \vec{\boldsymbol{\mathcal{G}}}(\mathbf{U}) - \vec{\boldsymbol{\mathcal{H}}}(\mathbf{U}, \vec{\nabla}_x \mathbf{U})$. The solution $\mathbf{U}$ is approximated by a tensor product of 1D Lagrange polynomials ℓ^N with a nodal interpolation ansatz

$$\mathbf{U}(\vec{\xi}, t) \approx \sum_{i,j,k=0}^{N} \hat{U}_{ijk}(t) \psi_{ijk}^N(\vec{\xi}) \tag{3.3}$$

with

$$\psi_{ijk}^N(\vec{\xi}) = \ell_i^N(\xi^1) \ell_j^N(\xi^2) \ell_k^N(\xi^3), \tag{3.4}$$

$\hat{U}_{ijk}(t)$ denotes the time dependent nodal Degrees Of Freedom (DOF) and $\ell_i^N(\xi)$ the standard Lagrange polynomial with degree N. The Lagrange polynomial is described by a set of nodal points $\hat{U}_{ijk}(t)$, e.g., Gauss or Gauss-Lobatto [56]. Here, the Gauss-Legendre points are applied for the interpolation, which consist of $N+1$ points per 1D Lagrange polynomials. This leads to $(N+1)^3$ DOF for each DG element. For the flux $\vec{\boldsymbol{\mathcal{F}}}$ a nodal interpolation ansatz can equally be chosen.

Continuing the brief derivation of the DGSEM, a test function $\phi(\vec{\xi})$ is multiplied to Section 3.1.1. The test function is integrated over the reference element E and the variational formulation for the reference element can be written as

$$\int_E \left(J\mathbf{U}_t + \vec{\nabla}_\xi \cdot \vec{\boldsymbol{\mathcal{F}}}(\mathbf{U}, \vec{\nabla}_x \mathbf{U}) \right) \phi(\vec{\xi})\, d\vec{\xi} = 0. \tag{3.5}$$

By further transformation the weak formulation is obtained

$$\int_E J\mathbf{U}_t \phi\, d\vec{\xi} + \oint_{\partial E} \underbrace{(\boldsymbol{\mathcal{G}}_n^* - \boldsymbol{\mathcal{H}}_n^*)}_{\boldsymbol{\mathcal{F}}_n^*} \phi\, ds - \int_E \vec{\boldsymbol{\mathcal{F}}}(\mathbf{U}, \vec{\nabla}_x \mathbf{U}) \cdot \vec{\nabla}_\xi\, \phi\, d\vec{\xi} = 0, \tag{3.6}$$

where $\vec{\boldsymbol{\mathcal{G}}}_n^* := \vec{\boldsymbol{\mathcal{G}}}_n^*(\mathbf{U}^+, \mathbf{U}^-)$ denotes the inviscid numerical flux function. Here, across the element interfaces discontinuities are allowed and the corresponding flux is solved with a classical Riemann solver. The superscripts $\pm$ are used to indicate both sides of the element interface.

Again, following the derivation from Hoffmann et al. [57], the viscous flux term is derived. For this purpose, the variable $\vec{\mathbf{S}}$ is introduced. With the additional variable Equation (3.1) is rewritten

$$\begin{aligned} \vec{\mathbf{S}} - \vec{\nabla}_x \mathbf{U} &= 0, \\ \mathbf{U}_t + \vec{\nabla}_x \cdot \vec{\mathbf{F}}(\mathbf{U}, \vec{\mathbf{S}}) &= 0. \end{aligned} \tag{3.7}$$

With this, the weak formulation is derived as

$$\int_E J\mathbf{U}_t \phi\, d\vec{\xi} + \oint_{\partial E} (\boldsymbol{\mathcal{G}}_n^* - \boldsymbol{\mathcal{H}}_n^*)\, \phi\, ds - \int_E \vec{\boldsymbol{\mathcal{F}}}(\mathbf{U}, \vec{\mathbf{S}}) \cdot \vec{\nabla}_\xi \phi\, d\vec{\xi} = 0. \tag{3.8}$$

The numerical flux of the viscous term $\boldsymbol{\mathcal{H}}_n^* = \boldsymbol{\mathcal{H}}_n^*(\mathbf{U}^+, \mathbf{U}^-, \mathbf{S}^+, \mathbf{S}^-)$ is therefore expressed with the additional variable. Based on Bassi and Rebay (BR) [12], the numerical viscous flux can be written as

$$\boldsymbol{\mathcal{H}}_n^* = \alpha_{\text{visc}}\, \boldsymbol{\mathcal{H}}_n(\mathbf{U}^+, \mathbf{S}^+) + (1 - \alpha_{\text{visc}})\, \boldsymbol{\mathcal{H}}_n(\mathbf{U}^-, \mathbf{S}^-), \tag{3.9}$$

where $\vec{n}$ is the surface normal and α_{visc} is a weighting factor for the lifting. According to [12] this factor can be chosen as 0.5, which is referred to as BR1 lifting. This type of lifting is also applied to the calculation of the temperature gradient ΔT.

3.1.2. Finite-Volume-Method

To keep this work self-contained, the FV method is briefly summarized. The FV method is a widely used approach for discretization in CFD [5]. The Equation (3.1) in the integral form for a sub-domain or element E can be written as:

$$\frac{\delta}{\delta t}\int_E \mathbf{U}\,\mathrm{d}V = -\oint_{\delta E}\vec{\mathbf{F}}(\mathbf{U})\cdot\vec{n}\,\mathrm{d}s, \tag{3.10}$$

where $\vec{n}$ is the outward facing normal vector and S is the surface. $\mathbf{U}_i^n$ and $\mathbf{U}_i^{n+1}$ denote the conserved quantities at t_n and t_{n+1}, respectively.

The method is based on the integral form of the continuity equations. The solution is approximated with the integral average, which allows discontinuities between the computational cells. A key element is the calculation of the flux between the neighboring cells. Riemann solvers calculate generally these numerical fluxes [85].

3.2. Stabilization for shocks and aliasing

The DG scheme and any high order projection based methods can suffer from instabilities due to high gradients in the solution. These instabilities, i.e., Gibbs type oscillations, can be caused by shocks or ailising. To counter these instabilities two classes of stabilization are common: introduction of artificial viscosity [4] or a local reduction of the polynomial degree in the vicinity of shocks or strong gradients [13, 25]. Latter has been chosen for the present work. However, a reduction of the polynomial degree, without further measures, leads to resolution reduction and consequently a lower accuracy. To counteract the reduced polynomial degree local mesh refinement is often applied in the affected areas.

Here, a shock capturing method is applied based on the idea of Sonntag and Munz [111, 112] and further developed as described by Hoffmann et al. [57]. Within a 'troubled' DG reference element (Figure 3.1a) sub-cells are superinduced. The 'split' element consists of $(N+1)^3$ equally distributed sub-cells, as shown in Figure 3.1b. For these sub-cells a second-order Total Variation Diminishing (TVD) FV scheme is applied. In that way the number of DOF and the resolution inside are kept constant; the reduction in accuracy is therefore limited to the influence of the order reduction. Gassner and Kopriva [46] showed that for a given dissipation error less DOF are required for higher order than for lower order schemes. Additionally, the memory layout remains unchanged, which avoids major interventions in the code structure and general performance. Notably a reference element is computationally more expensive with shock capturing than a DG element. This leads to load imbalances. The treatment of these load imbalances are acknowledge, however, is beyond the scope of this thesis.

The detection of shocks is achieved by an indicator. Here, the indicator proposed by Persson and Peraire [92], which can also detect oscillating polynomials due under-resolved scales is applied and can be written as

$$S_{\mathrm{P}} = \frac{\left(U_i - \hat{U}_i, U_i - \hat{U}_i\right)_e}{\left(U_i, U_i\right)_e}, \tag{3.11}$$

where U_i denotes an arbitrary conservative or primitive variable, commonly pressure or density are used, and $(.,.)_e$ is the standard inner product in $L_2(\Omega_e)$. For the applied cases of this work, density has been proven to obtain satisfactory results.

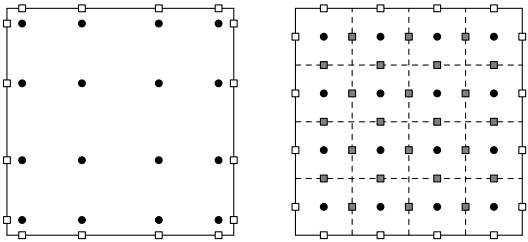

(a) 4th order DG element **(b)** FV-subcell approach

Figure 3.1.: Schematic of the shock capturing with the Finite-Volume subcell approach for a 4th order DG element (cf. [57, 111, 112]).

3.3. Riemann solvers

The previously introduced DG and FV methods require numerical fluxes. These fluxes can be calculated with a Riemann solver. At each DG element and FV subcell surface at each side two states are present, $\mathbf{U}^+$ and $\mathbf{U}^-$. The Riemann solver provides the intermediate state of those two. More details on Riemann solvers can be found in Toro [123]. In the present work, two Riemann solvers are used, the Local Lax Friedrich (LF) and the Harten-Lax-van Leer-Contact (HLLC) and therefore are introduced in the following. The different states are illustrated in Figure 3.2.

3.3.1. Local Lax-Friedrich (LF) solver

One of the simplest Riemann solvers is the local Lax-Friedrich (LF). Here, the signal speed of the rarefaction wave and the shock are assumed to be the same. In reality the

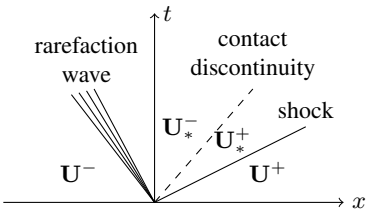

Figure 3.2.: Notation for the states of Riemann scheme.

rarefaction wave is a fan, however, in the LF it is approximated as a single wave. The contact discontinuity is neglected. This leads to an additional smearing in the two-phase region, since two states in this region are separated by their difference in entropy and can be viewed as a sort of contact discontinuity. Nonetheless, since the governing equations contain a contact discontinuity, they can be represented even with a LF, however they are smeared. The maximum shock speed and consequently the rarefaction wave propagation velocities are guessed as

$$s = \max(|w^-|, |w^+|) + \max(a^-, a^+), \tag{3.12}$$

where $w^\pm$ and $a^\pm$ are velocities normal to the element interface and sound speeds at both sides of the element interface, respectively. Since the sound speed can vary strongly between the liquid and the two-phase region, the approximation of a single propagation speed for both sides can lead to large errors at the interface to the two-phase region. Figure 3.3 illustrates the local LF scheme. With this propagation speed guess the numerical flux for the local Lax-Friedrich is expressed as

$$\boldsymbol{\mathcal{G}}_n^* = \frac{1}{2}\left(\mathbf{F}_n^{A-} + \mathbf{F}_n^{A+}\right) - s\left(\mathbf{U}_n^+ - \mathbf{U}_n^-\right). \tag{3.13}$$

Since the approximation of the flux uses only a small number of operations this Riemann solver demands only little computational time. In the present work, it is the most stable, but also most dissipative Riemann solver, i.e., introduces the largest approximation errors.

3.3.2. Harten-Lax-van Leer-Contact (HLLC) solver

The Harten-Lax-van Leer-Contact (HLLC) Riemann solver is more complex than LF. The complexity results in higher computational costs and also, HLLC tends to be not as stable as the LF Riemann solver. However, the numerical dissipation is less due to

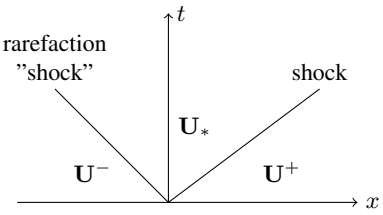

Figure 3.3.: Scheme of the local Lax-Friedrich.

a better approximation of the contact discontinuity. In contrast to the LF, the HLLC approximates two different propagation speeds, s^+ and s^-, which are written as

$$s^- = \min(w^-, w^- - a^-, w^- + a^-, w^+, w^+ - a^+, w^+ + a^+), \tag{3.14}$$

$$s^+ = \max(w^-, w^- - a^-, w^- + a^-, w^+, w^+ - a^+, w^+ + a^+). \tag{3.15}$$

Further, the propagation speed of the contact discontinuity is calculated by

$$s_* = \frac{p^+ - p^- + \rho^- w^-(s^- - w^-) - \rho^+ u^+(s^+ - w^+)}{\rho^-(s^- - w^-) - \rho^+(s^+ - w^+)}. \tag{3.16}$$

However, this approximation is incorrect for the two-phase region. The numerical flux depends on these approximations

$$\boldsymbol{\mathcal{G}}_n^* = \begin{cases} \mathbf{F}^{a-} & \text{if} \quad 0 \le s^- \\ \mathbf{F}_*^{a-} & \text{if} \quad s^- \le 0 \le s_* \\ \mathbf{F}_*^{a+} & \text{if} \quad s_* \le 0 \le s^+ \\ \mathbf{F}^{a+} & \text{if} \quad 0 \ge s^+ \end{cases}, \tag{3.17}$$

where the $*$ indicates the states in the star region, i.e., states between the rarefaction wave and shock, which are split by the contact discontinuity. The flux in the star region is

$$\mathbf{F}_*^{a\pm} = \mathbf{F}^{a\pm} + s^{\pm}(\mathbf{F}_*^{\pm} - \mathbf{U}^{\pm}). \tag{3.18}$$

The states in this region can be expressed as

$$\mathbf{U}_*^{\pm} = \rho^{\pm}\left(\frac{s^{\pm} - w^{\pm}}{s^{\pm} - s_*}\right)\begin{pmatrix} 1 \\ s_* \\ w_y^{\pm} \\ w_z^{\pm} \\ \frac{E^{\pm}}{\rho^{\pm}} + (s_* - w^{\pm})\left[s_* + \frac{p^{\pm}}{\rho^{\pm}(s^{\pm} - w^{\pm})}\right] \end{pmatrix}, \tag{3.19}$$

where $w_{y,z}^{\pm}$ denote the velocity components parallel to the element interface at both sides of the element interface.

3.4. De-aliasing

The DGSEM is a high-order method with low inherent numerical dissipation. For these type of methods aliasing issues can result in oscillation and instabilities of simulations. DNSs are out of reach for the high-Re flows in the present work, therefore the under-resolution leads to potential aliasing. Further, the non-linearity of the real gas approximation might increase the tendency to aliasing issues. In the majority of DGSEM simulations linear EOSs are used, e.g., ideal gas approximations. However, a detailed analysis of the different aliasing potential due to EOS approximation is beyond the scope of this work.

To realize the stable simulation de-aliasing needs to be applied in some form. Here, in regions with relatively low aliasing the dissipation of the DGSEM is sufficient to suppress an escalation of the approximation errors. However, in areas with high aliasing potential and possible instability due to the aliasing the FV sub-cell scheme is applied. The sub-cells have TVD properties and therefore stabilize aliasing and the applied Persson indicator is capable of also detecting oscillation due to aliasing. This procedure is similar to the Monotonically Integrated Large Eddy Simulation (MILES) approach introduced by Boris et al. [20] and Grinstein et al. [50]. It is important to emphasize that explicit de-aliasing schemes, e.g., over-integration [14, 18, 45] or others [11, 136], would very likely be able to further improve the simulation results. A drawback of such a explicit de-aliasing scheme are the additional computational costs. Further, the focus of this work was on the evaluation of new physical insides of very complex and demanding flows, hence the here proposed very stable solution was chosen.

3.5. Efficient usage of multi-parameter equation of state

Previously several different EOS approximations have been introduced in Section 2.2. Whilst the simple ideal gas equation is very fast to analyze in a simulation program, it is very limited to a small range of pressures and temperatures. Consequently, other approximations are needed for real gas flows or cavitation, which are more computationally demanding. Without further measures a direct evaluation of, for example, the Helmholtz free energy formulation would be infeasible for a CFD simulation of reasonable size. The evaluation is orders of magnitude slower than for an ideal gas. It is needed several times per time step and DOF in CFD simulations; this adds up to many millions evaluations even for small simulations.

Therefore, in the present work the EOS data is tabulated. The data is tabulated in the pre-processing and only read in the actual simulation. The idea is based on Dumbser

et al. [34] and further improved as presented by Hoffmann et al. [57]. A detailed description is provided by the latter [57], however, to keep this work self-contained a brief description is given in the following.

3.5.1. Choice of Equation of state approximation

For every type of modeling and approximation it is relevant to find the correct balance between computational costs and accuracy. Hence, the choice of EOS approximation is discussed in the following. A brief summery of different EOS approximations is given in Section 2.2.

First, it is important to analyze what type of fluid is used and under which conditions it occurs within the simulations. In the present work, two different fluids are assessed, e.g., methane at high pressures and water in different states of matter. For both cases an ideal gas approximation is unfeasible and a more complex EOS is required. Whilst cubic equations offer satisfactory accuracy for the gaseous phase, their approximation within the two-phase region is incorrect and cannot be used for cavitational simulations. Hence, it is desirable to use the Helmholtz formulations. The evaluation of such a high-accuracy multiparameter EOS, however is computationally very expensive and cannot be applied directly for CFD simulations in its analytical form. Therefore, EOS data is tabulated as part of the pre-processing.

Here, the evaluation time is very important. The evaluation times of a ideal gas law, a cubic equation, i.e., the Peng-Robinson was chosen as an example, and a Helmholtz equations formulation are compared with each other. The Helmholtz equations are both assessed as direct evaluation and in the proposed tabulated form. For the Helmholtz equations the Open Source library CoolProp version 4.2.6 is used. Later the implementation of the tabulated EOS is discussed in further detail. For the table evaluation different depths or levels of the table are evaluated, i.e., depending on the fluid properties different table levels are required to reach a certain accuracy. The evaluation is in all cases from the variables density ρ and inner energy e to pressure. To obtain the pressure, in the context of a density based solver, the temperature needs be calculated iteratively, i.e, e is guessed, for both the cubic equations and the Helmholtz formulation. Table 3.1 summarizes the evaluation times of each approach. The computational cost for the direct evaluation for ideal gas, Peng-Robinson and the Helmholtz equation increases with their complexity. It is interesting to notice, that with the table approach the computational costs can be reduced significantly even compared to the cubic equation. These findings allow it to use the higher accuracy EOS and reduce the simulation costs compared to cubic real gas approximation. Of course, the computational costs are increased to the direct evaluation of ideal gas, which is unavoidable.

Table 3.1.: Evaluation times for the different EOS approaches. Data for ideal gas and Helmholtz (direct) are take from Hoffmann et al. [57].

EOS type	Time [1×10^{-6} s]
Ideal gas	0.01712
Peng-Robinson	3.200
Helmholtz (direct)	232.0
Helmholtz (tabulated with level 6)	0.1953
Helmholtz (tabulated with level 15)	0.2868

3.5.2. Implementation of tabulated Equation of State

Having motivated the choice of tabulated Helmholtz equation as an EOS approximation, the used implementation is introduced. The interested reader is referred to Hoffmann et al. [57] for a more detailed discussion. The provided EOS from CoolProp is coupled with the currently used CFD code, which is based on the conservative form (Equation (2.1)). From density and inner energy the other variables are calculated, i.e., pressure, temperature, speed of sound, viscosity and thermal conductivity and from pressure and temperature the density and inner energy. These variables are needed for the flux calculation. In the implementation, CoolProp is evaluated prior to the simulation and the calculated values are stored in a table. In the present work depending on the application, three or four different conversion tables are required. For fluids with high gradients at small densities, e.g., water, it was found beneficial to split the conversion from density and inner energy to temperature into two tables, $\rho \geq 1\,\mathrm{kg\,m^{-3}}$ and $\rho < 1\,\mathrm{kg\,m^{-3}}$. The conversion from the conservative to the primitive variables is split into two steps. First, the temperature is evaluated from ρ and e, afterwards ρ and T are used to evaluate the other primitive variables. The main reason for this split is in the pre-processing and the total table size, the evaluation of T is very expensive. Therefore, the table refinement is done separately, which increases the pre-processing speed significantly and reduces the overall memory requirement of the tables in the simulation. An overview of the different tables is given in Table 3.2.

The table approach is based on a quad-tree domain decomposition strategy. The primitive variables are represented by polynomials within each cell. The solution is discontinuous across the cell interfaces. For each cell for the thermodynamic variable, Φ, the approximation error

$$\epsilon = \left| \frac{\Phi_{\text{table}} - \Phi_{\text{CoolProp}}}{\Phi_{\text{table}}} \right|, \tag{3.20}$$

to the CoolProp solution is calculated. Based on the error the table is locally refined.

Table 3.2.: Conversion tables for the EOS approximation.

Input varibles	Output varibles	Usage criteria
$\rho \quad e$	T	$\rho \geq 1\,\mathrm{kg\,m^{-3}}$
$v \quad e$	T	$\rho < 1\,\mathrm{kg\,m^{-3}}$
$\rho \quad T$	$p \quad a \quad \lambda \quad \mu$	
$T \quad p$	$\rho \quad e$	

The process is illustrated in Figure 3.4. In the domain, e.g., (ρ, e), the approximation error is compared to the error threshold ϵ_{th} (Figure 3.4a). For $\epsilon > \epsilon_{\text{th}}$ a sub quad-tree is generated, i.e., the domain is refined, and the approximation error is again compared in the sub quad-tree to the threshold (Figure 3.4b). This process is repeated until the criteria is satisfied in the whole table or the maximum level is reached.

The error threshold, ϵ_{th} for the table strongly depends on the application. For real gas approximation an $\epsilon < 10^{-4}$ is sufficient, however when phase changes are involved it might be necessary to decrease the threshold further. For the present study, this level of accuracy for the entire variable range was achieved with a maximal refinement-cell level of 19. Of course, the accuracy of the tabulated EOS is always limited by the accuracy of the original formulation, here the Helmholtz formulation.

The construction process of the table is completely parallelized and can run on an arbitrary number of processors. For the tables used in Chapter 4, methane is tabulated for

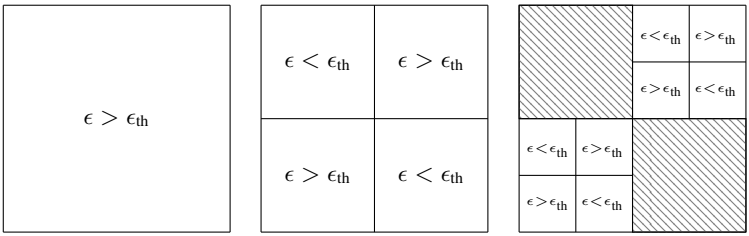

Figure 3.4.: Schematic of the building process of an EOS table with the quad-tree approach (hatched box: no further action), a) initial domain b) check after refinement, c) check the refined sub quad-tree.

densities in the interval $1 \times 10^{-4}\,\mathrm{kg\,m^{-3}}$ to $1200\,\mathrm{kg\,m^{-3}}$ and for temperatures ranging from $91\,\mathrm{K}$ to $624\,\mathrm{K}$, respectively. This kind of table can be built within a few minutes on 2400 cores. It is vital that the table can be evaluated efficiently during the calculation. With this approach the evaluation of the EOS is decoupled from the actual simulation and allows to efficiently use any EOS. Compared to analytical ideal gas implementation the required computational costs of a simulation increase roughly by a factor of 3 to 4 for the present implementation.

For methane the different tables for $(\rho, e) \rightarrow (T)$, $(\rho, T) \rightarrow (p, a, \lambda, \mu)$ and $(T, p) \rightarrow (\rho, e)$ have a size of 116MB, 49MB and 2.9MB, respectively. For water the used table sizes were $(\rho, e) \rightarrow (T)$: 302MB, $(v, e) \rightarrow (T)$: 1.4GB, $(\rho, T) \rightarrow (p, a, \lambda, \mu)$: 3.9GB and $(T, p) \rightarrow (\rho, e)$: 325M. Each core stores each table, a node with 24 cores has a total of 128GB of storage on the used system of the Hazel Hen supercomputer of the High Performance Computing Center Stuttgart (HLRS). Therefore, the available memory is sufficient, however, cache effects [119] are out of reach with this implementation.

3.6. Modeling of multiphase flows for cavitation

The modeling of multiphase flows is very challenging and depending on the purpose of the simulation different methods need to be considered. In the following, a brief overview of different types of models are given.

3.6.1. Thermodynamic state model

Kolev [67] uses three different classes of approximations, i.e., barotropic, homogeneous equilibrium and inhomogeneous non-equilibrium. In Table 3.3 the three classes are summarized.

The barotropic and homogeneous equilibrium approximations are both based on an averaged state within a reference cell. Barotropic models are the most simple of the three classes. For the barotropic EOS the density is only a function of pressure $\rho = \rho(p)$. Further effects such as dissolved air in the liquid can be incorporated into the EOS. Despite the simplifications of the model good results can be achieved and have been published [36, 100].

However, with large pressure differences the fluid can experience changes in temperature. This can influence the behavior of the EOS and other fluid properties and might lead to not negligible effects. From the conservative variables ρ and e, p and T can be derived. Here, the velocities, the pressure and the temperature are assumed to be the same in both phases. Therefore, both phases have no slip with each other, which is a simplification. Nonetheless, the homogeneous equilibrium model is well suited for the present work and is applied in Chapters 4 and 5.

The last of the three classes is the inhomogeneous non-equilibrium model. It is the most complex and numerically most demanding, i.e., computational resources and complexity. Once slip between the phase becomes important this class should be applied. Both phases need to be considered separately and are coupled with each other.

3.6.2. Evaporation and condensation models

In the following, a brief summery is given of the mass transfer at phase boundaries. There are a number of different evaporation models in the literature [83]. Here, these are categorized in three different classes, e.g., thermodynamic equilibrium model discontinuous, thermodynamic equilibrium continuous and thermodynamic non-equilibrium model. These are briefly summarized in Table 3.4.

The current work is based on the thermodynamic equilibrium discontinuous model. The terminology discontinuous refers to the fact that here the phase boundary is assumed to be plain. Consequently, the surface boundary is in this assumption discontinuous. In

Table 3.3.: Modelling of two-phase flows.

model	varible assumptions
barotrop	$\rho, p, \vec{w}$
homogen	$\rho_g, \rho_l, \vec{w}_g = \vec{w}_l, T_g = T_l, p$
inhomogen	$\rho_g, \rho_l, \vec{w}_g, \vec{w}_l, T_g, T_l, p_g, p_l$

Table 3.4.: Comparison of evaporation models.

model	therm. equilibrium	therm. non-equilibrium
discontinuous model	flat phase boundary $p_g = p_l = p$ $T_g = T_l = T$	
continuous model	curved phase boundary $p_g - p_l = 2\sigma/r_B$ $T_g = T_l = T$	$p_g - p_l = 2\sigma/r_B$ $T_g \neq T_l$
	no kinematic of heat transfer	kinematic of heat transfer

the thermodynamic equilibrium model it is assumed that all thermodynamic process are instantaneous and hence always in equilibrium.

3.6.3. Limitations of the applied method

The HEM introduces a number of limitations, which are briefly discussed for cavitation. The discussion is limited to effects most relevant for the present work. Most of the discussed limitations could be appointed by specific numerical methods. However, the computational costs and the complexity of the models are out of range for the present work.

Surface tension

The surface tension and the curvature of the interface between liquid and gas are neglected. In reality, the curvature of an interface introduces a pressure difference across the interface.

$$\Delta p = 2\gamma H, \tag{3.21}$$

where H denotes the curvature of the interface. For a spherical bubble the curvature corresponds to $1/R$. Hence, the pressure difference due to surface tension and curvature becomes important for very small radii. Comparing Equation (2.41) with and without the surface tension part shows only little difference for the collapse time and minimum radius of a bubble. Therefore, the influence on the simulation in the current work are acceptable. However, to overcome this limitation the interface between the liquid and gas needs to be traced and modeled. In the literature, different approaches are presented, e.g., sharp interface representation [38].

Superheating or boiling delay

In most cases the energy required for a phase change from liquid to gaseous state can be influenced by a so called superheating or boiling delay. Here, the required energy is extracted from the liquid phase and the local temperature drops. Therefore, the temperature at which a phase change occurs changes; this $\Delta T = T_f - T_f'$ is called the boiling delay, where T_f denotes the fluid temperature and T_f' the local temperature of the fluid of the boiling delay. The effect is most dominant close to the critical point [41]. The effect of boiling delay is neglected in the current work.

Dissolved air and diffusion

All technically relevant liquids contain a certain content of dissolved air. Over a long period of time it is possible to reduce this air, however, it is impossible to reduce it to 0. During the growth of a cavitation bubble the dissolved air diffuses into the vapor. From

Equation (2.41) it is apparent that the term with the dissolved air has a major impact on the bubble behavior. First, it limits the minimum radius of the bubble and acts as a damper for the collapse [134]. Consequently, neglecting it makes the collapse faster and more rapid. Further, it reduces the ability of the fluid to sustain tension and cavitation could occur at earlier stages.

4. Influence of fluid properties on gas dynamics

Many simulations of gas dynamics problems found in the literature treat the gas as ideal or at least use strong simplifications of the fluid properties, e.g., the equation of state or the transport values. To determine where an ideal gas expression is valid often ball park values for pressure and temperature are used. These values can vary significantly depending on both the problem to solve and the fluid. For example, the point at which the compressibility effect cannot be neglected changes for different fluids. The compressibility factor Z is shown in Figure 4.1 for different pure and pseudo-pure gases. All gases behave differently, however, at a certain pressure the ideal gas approximation becomes invalid for all gases. It can be further noted, that generally the decrease in Z is more dominant at lower temperatures.

A simple example of the possible implications of an incorrect approximation of Z is a high pressure storage tank for methane: with a storage tank of a volume of $V = 1\,\mathrm{m}^3$ and assuming a constant temperature $T = 290\,\mathrm{K}$, the storable mass strongly depends on the compressibility of the real gas: $m_{p=1\,\mathrm{bar}} = 0.6666\,\mathrm{kg}$, $m_{p=10\,\mathrm{bar}} = 6.783\,\mathrm{kg}$,

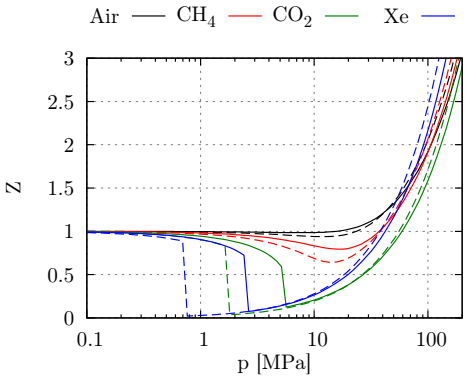

Figure 4.1.: Compressibility factor Z over pressure at a constant temperature $T = 290\,\mathrm{K}$ (solid) and $T = 250\,\mathrm{K}$ (dashed) for air, carbon dioxide (CO_2), methane (CH_4) and xenon (Xe).

$m_{p=100\,\mathrm{bar}} = 79.89\,\mathrm{kg}$ and $m_{p=1000\,\mathrm{bar}} = 347.4\,\mathrm{kg}$. Hence, an ideal gas approximation of the available gas stored in the tank based on the pressure, would lead to an overestimation of almost a factor of two at $p = 1000\,\mathrm{bar}$.

In the following, the importance of real gas modeling is demonstrated on the basis of 1D and 3D test cases. It is shown that at low pressures the real gas approximation with the Helmholtz free energy formulation blends into the ideal gas approximation. It is also pointed out that the fitting of the Helmholtz free energy formulation in the region of low pressures are still dependent on temperature, which prevented a perfect blend to the ideal gas approximation. Further, a fully turbulent 3D free stream jet is examined for its real gas behavior. It is demonstrated that significant differences are between real gas and ideal gas approximations.

4.1. Riemann problem with perfect and real gases

For many everyday flows considering the gas as ideal or perfect is sufficient. However, in nature and industry many applications do not allow for a perfect gas assumption and the fluid needs to be treated with its real gas properties, i.e., an appropriate approximation of the fluid.

A Riemann problem simulation is carried out with perfect and real EOS approximations to gain a better understanding of their differences. Here, the aim is to underline the necessity of a proper real gas modelling where necessary.

For the 1D Riemann problem test case three different cases are considered, i.e., variation in pressure while the pressure ratio remains constant. The domain has a length of $1\,\mathrm{m}$. The fluid is methane and remains gaseous throughout all cases. For the modeling of perfect gas the ideal gas laws Equations (2.10), (2.13), (2.14), (2.35) and (2.38) are used to generate the EOS tables. Here, the specific gas constant is $R = 518.3\,\mathrm{J\,kg^{-1}\,K^{-1}}$, $\kappa = 1.303$ and $\mathrm{Pr} = 0.7305$. The thermodynamic properties for the perfect gas table are taken from CoolProp V6 at $10\,\mathrm{Pa}$ and $300\,\mathrm{K}$.

The EOS and the transport properties of the real gas simulation are based on the Helmholtz energy formulation as implemented in CoolProp V4. For methane CoolProp fits the parameter of the Helmholtz equation to the experimental data from Setzmann and Wagner [107] for the EOS and data from Friend et al. [42] and from Quinones-Cisneros and Deiters [98] for the thermal conductivity and the viscosity, respectively.

The EOS tables are generated with an accuracy of 1×10^{-8} for both perfect and real gas. The threshold is chosen very low to avoid errors introduced by the table in this very detailed study. For the simulations the HLLC Riemann solver is applied. The mesh consists of 800 elements and $N = 5$, which leads to 4800 DOF in x-direction. Since a part of the purpose of these simulations is the validation of the 3D Flexi code, the 3D framework is used and the momentum in y- and z-direction are set to 0 ($U_2 = U_3 = 0$). The initial conditions for the different cases are summarized in Table 4.1. The initial

velocity is set to $w_1 = 0\,\mathrm{m\,s^{-1}}$.

The notation for the different states is summarized in Figure 4.2 with the typical wave pattern of the Riemann scheme. In the star region two intermediate states exist separated by a contact discontinuity.

The different simulation results for the real gas table are shown in Figure 4.3 at $t = 1 \times 10^{-4}\,\mathrm{s}$. The pressure and density graphs are normalized with the corresponding initial state Φ_L. Only little differences in pressure are observed for Case 3 for the star region and the propagation velocity of the shock front. Since the speed of sound decreases with pressure, the shock propagates slower at higher pressures. For the temperature the differences are more significant for Case 3 compared to the other cases. The temperature decreases more with increasing pressure and the position of the contact discontinuity varies, due to the slower velocity. The expansion wave shows observable differences for the density for Case 3. Here, at lower pressures the difference is only marginal.

Table 4.1.: Initial conditions for the Riemann problem cases.

Case	Case 1		Case 2		Case 3	
EOS modeling	PG	RG	PG	RG	PG	RG
p_L	1	1	10	10	100	100
p_R	0.1	0.1	1	1	10	10
T_L	300	300	300	300	300	300
T_R	300	300	300	300	300	300
ρ_L	0.6431	0.6443	6.431	6.542	64.31	75.18
ρ_R	0.06431	0.06432	0.6431	0.6443	6.431	6.542

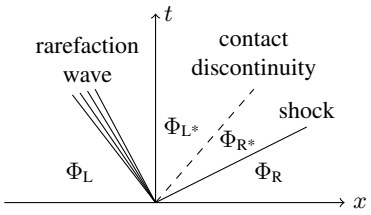

Figure 4.2.: Notation for the states of the Riemann problem.

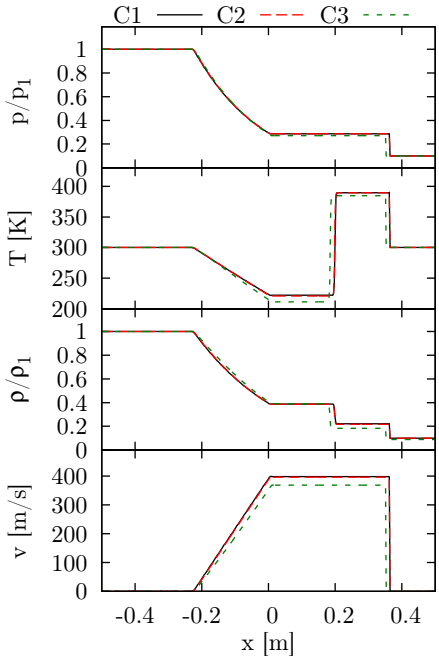

Figure 4.3.: Riemann problem Cases 1 to 3 for real gas at $t = 1 \times 10^{-4}$ s.

Figure 4.4 shows a comparison between the perfect gas and the real gas approximation for Case 1. For most values there is no noticeable difference, with the exception of $T_{\mathrm{L,R^*}}$. Even though the pressure is in a range which is appropriate for the perfect gas approximation the real fluid approximation is depended on temperature at very low pressures, too. This is due to the temperature dependence of the inner degrees of freedom of a methane molecule and is discussed in further detail in Section 4.1.1. The difference in shock propagation is due to the difference in $T_{\mathrm{R^*}}$. The expansion wave speeds are almost identical, since the difference for $T_{\mathrm{L^*}}$ is small. At lower temperatures the speed of sound is less temperature dependent than for higher temperatures.

Case 2 is shown in Fig. 4.5. Similar to Case 1 the change in temperature can be observed clearly. However, since the pressure is higher, differences for all values are visible. For example, ρ_{L} varies a little due to the change of compressibility. The speed of sound is almost the same at the shock. The velocity varies and consequently the

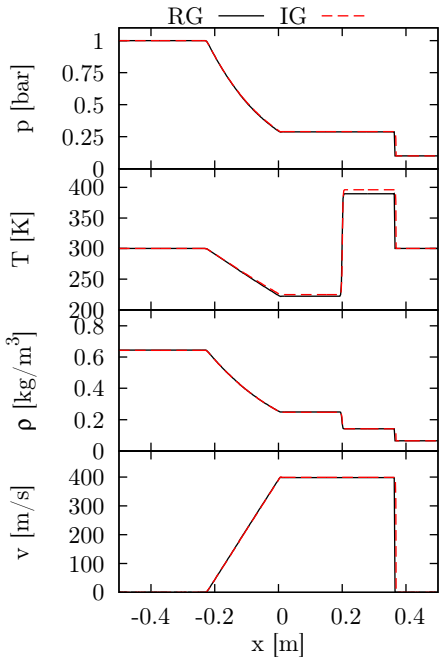

Figure 4.4.: Riemann problem case 1 at $t = 1 \times 10^{-4}$ s.

propagation of the contact discontinuity.

For Case 3 p_L is well in the real gas regime. Strong real gas effects are shown in Figure 4.6. For all values within the star region Φ_{L,R^*} strong differences are observed, e.g., velocity, sound speed, pressure. Due to the strong influence of compressibility, the density varies strongly. Overall, especially for Case 3 a real gas approximation is necessary to predict the flow properties. Important values for industrial applications, e.g., mass flow and jet penetration, would be inaccurate given the strong deviation.

4.1.1. Isentropic expansion

Following the above discussion, the expansion process of Cases 1 to 3 is analyzed in further detail. Here, a comparison between three different expressions is carried out, perfect gas formulation, an approximation for real gases from the literature [102] and an exact

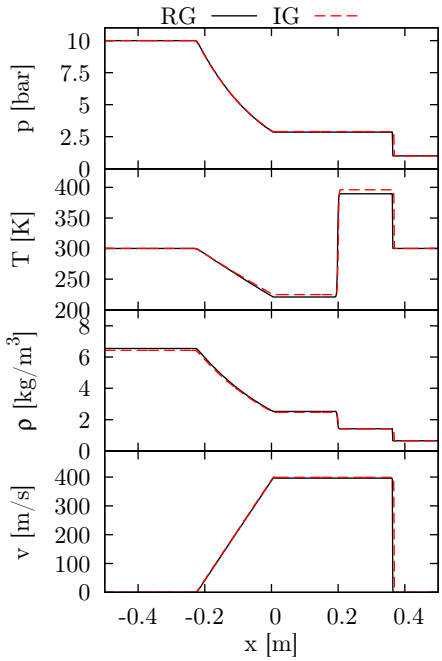

Figure 4.5.: Riemann problem case 2 at $t = 1 \times 10^{-4}$ s.

expression for the isentropic relation. The general expression with the states 1 and 2 are presented in Equations (4.1) to (4.3). For the comparison with the 1D Riemann problem the states Φ_L and Φ_{L^*} replace the notation for the conditions 1 and 2, respectively.

For a perfect gas the isentropic relation between temperature and pressure can be expressed as [115]

$$\frac{T_2}{T_1} = \left(\frac{p_2}{p_1}\right)^{\frac{\kappa-1}{\kappa}} . \tag{4.1}$$

To account for real gas effects Rist [102] introduced an approximation of the isentropic

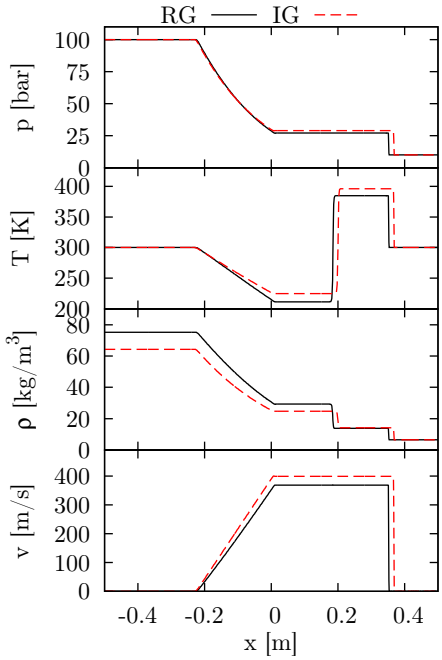

Figure 4.6.: Riemann problem case 3 at $t = 1 \times 10^{-4}$ s.

relation. It can be written as[I]

$$\frac{T_2}{T_1} = \left(\frac{p_2}{p_1}\right)^{\left(\frac{\kappa-1}{\kappa}\right)_{1,2}} \left(\frac{Z_1}{Z_2}\right)^2, \tag{4.2}$$

where $1, 2$ denotes the average state of conditions 1 and 2. Since the values at the state 2 are unknown, a Newton iteration is applied.

Further, from the fundamental equation for enthalpy and the Maxwell relations the

[I] [102] uses $K = Z/Z_N$ the gas law deviation coefficient in its formulations. Z_N is the compressibility factor at standard conditions. In the current work, only Z is used, which is interchangeable with K for the applied cases.

isentropic relation can be expressed as derived in Jungemann [63]

$$\left(\frac{\partial T}{\partial p}\right)_s = \left(\frac{\partial v}{\partial T}\right)_p \frac{T}{c_p}. \tag{4.3}$$

For both Equations (4.2) and (4.3) the fluid properties from COOLPROP V6 are used. For Equation (4.3) MATLAB is used and coupled to COOLPROP V6 to solve the differential equation.

In Table 4.2 the simulation results for the isentropic expansion for the Riemann problem are summarized and compared to Equations (4.1) to (4.3). The temperature ratio $T_\mathrm{L}/T_{\mathrm{L}^*}$ for the perfect gas approximation is constant throughout the cases and matches Equation (4.1). Compared to the real gas approximation the difference increases with p_L, which is expected due to real gas effects. The simulation results fit the direct evaluation from Equation (4.3) perfectly. Therefore, the obtained results are able to represent this thermodynamic process very well. The approximation from Equation (4.2) accounts for the real gas effects. However, the effects are overestimated.

From the Riemann problem analysis for Case 1 at low pressures, which is often considered as perfect gas regime, a difference between the perfect and real gas approximation is found. By further analyzing the temperature ratio $T_\mathrm{L}/T_{\mathrm{L}^*}$ with a fixed pressure ratio of $p_\mathrm{L}/p_{\mathrm{L}^*} = 3.487$, which corresponded to $p_\mathrm{L}/p_{\mathrm{L}^*}$ for Case 1 with real gas, the temperature dependence of the used Helmholtz free energy formulation at lower pressure is apparent. Figure 4.7 shows $T/T_\mathrm{isentropic}$ over pressure for different temperatures. Even at very low pressures the flow is temperature dependent. At higher pressure a

Table 4.2.: Isentropic expansion for the Riemann problem.

Case	1		2		3	
EOS modeling	IG	RG	IG	RG	IG	RG
p_L	1	1	10	10	100	100
p_{L^*}	0.2889	0.2868	2.889	2.856	28.89	26.99
$p_\mathrm{L}/p_{\mathrm{L}^*}$	3.461	3.487	3.461	3.501	3.461	3.705
T_L	300	300	300	300	300	300
T_{L^*}	224.8	222.0	224.8	220.9	224.8	211.5
$T_\mathrm{L}/T_{\mathrm{L}^*}$	1.335	1.351	1.335	1.358	1.335	1.418
from Equation (4.1)	1.335		1.335		1.335	
from Equation (4.2)		1.352		1.379		1.503
from Equation (4.3)		1.351		1.358		1.418

strong increase in temperature ratio is observed. The ratio reached an abrupt peak due to phase change.

Figure 4.8 shows c_p as a function of pressure for different temperatures for methane. c_p is directly connected to the isentropic relation and the responsible value for the temperature dependency at low pressures. For the present study data from Setzmann and Wagner [107] are used. They fitted the data for the ideal gas part of the isobaric specific heat capacities to McDowell and Kruse [78], which can be expressed as

$$\frac{c_p^0}{R} = n_0 + \sum_{i=1}^{5} n_i \frac{(A_i/T)^2 \, e^{A_i/T}}{(A_i/T - 1)^2}. \tag{4.4}$$

Hence, c_p is temperature dependent for methane. However, for the noble gas argon Tegeler et al. [122] showed that it depends only little on temperature, i.e., the contribution of electronic excitation is only $0.01\,\%$ at $10\,000\,\mathrm{K}$. Consequently, treating non-noble gases as caloric perfect gases introduces a derivation even for very low densities. However, the differences are only marginal and are most likely only observable for simple 1D test cases.

Further, the compressibility factor Z is at very low pressure independent of the temperature and remains 1, since a derivations are due to intermolecular forces. This is also represented in the relation to the Helmholtz free energy, which has no ideal gas part (see Table 2.2). Figure 4.9 shows the compressibility over pressure for different temperatures. Z remains independent of temperature up to about 1×10^5 Pa.

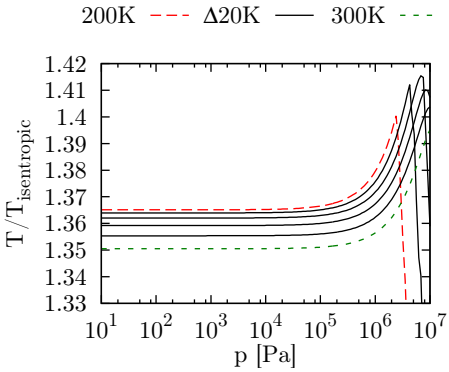

Figure 4.7.: Temperature ratio for the isentropic relation from Equation (4.3) for a fixed pressure ratio of $p_1/p_2 = 3.487$.

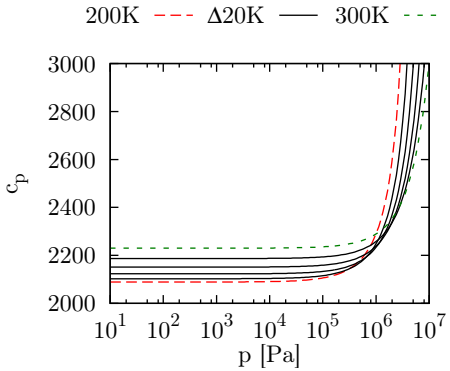

Figure 4.8.: Specific heat capacity at constant pressure c_p as a function of pressure for different temperatures of methane.

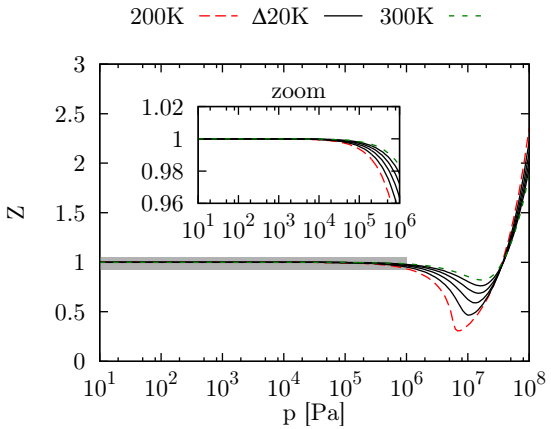

Figure 4.9.: Compressibility factor Z of methane as a function of pressure for different temperatures.

A more detailed discussion on isentropic (Section A.1) and isenthalp (Section A.2) expansions is in Chapter A. In this chapter expansions at different pressures, temperatures and pressure ratios are assessed for different fluids, e.g., methane, air and water.

4.2. Micro channel flow of a simplified direct gas injector

In this section, a 3D simulation with real gas approximation is carried out. As a test case a micro channel flow is chosen. The simulation represents a simplified DGI, i.e., the dimensions of the micro channel and the operating pressures are in the order of a modern DGI. However, before examining a supersonic jet, a subsonic jet at high pressure is analyzed and compared to commonly used self-similar jet results.

4.2.1. Numerical setup

The simulation framework is used for two different scenarios: a subsonic jet flow and a developing supersonic jet. The subsonic jet flow is used as a validation case. To verify the results, self-similar velocity profiles are evaluated and compared to literature values. The main focus, however, is on the simulation of a developing supersonic underexpanded jet. Here, the influence of real gas effects are investigated and compared to the properties of the supersonic jet for different temperatures and pressure levels.

Similar setups are used for both the subsonic and supersonic jet. The flow passes through a throttle, with diameter $D = 5 \times 10^{-4}\,\mathrm{m}$ and a throttle length $L_{\text{throttle}} = 4D$ and expands into a reservoir. For the subsonic jet, the domain length is set to $L_{\text{domain}} = 100D$ and for the supersonic jet to $L_{\text{domain}} = 40D$. A sketch of the used geometry is given in Fig. 4.10a.

For the simulation an unstructured hexahedral grid is used. For the subsonic jet the grid is only refined at the boundaries of the throttle, see Figure 4.10b, whereas for the supersonic jet the flow area with shocks is simulated with a higher resolution, see Figure 4.10c. The distance from the inlet to the throttle is $6D$.

The used meshes have 4.670×10^4 and 4.733×10^5 elements for the subsonic and supersonic jet, respectively, corresponding to 2.989×10^6 and 3.029×10^7 DOF. For the supersonic jet the throttle exit has 34 elements in radial direction with refinement at the wall and for the subsonic jet 14 elements.

For the inlet and outlets weakly imposed Dirichlet type boundaries are applied, which have been used successfully for this kind of flow [54]. At the throttle wall and at the lip of the throttle a no-slip condition is used, while the lateral walls upstream of the throttle are defined to be inviscid. Damping layers for the subsonic jet are used to avoid non-physical reflections at the outflow boundaries. Within the damping layer the solution is relaxed towards the outflow condition. Larger scale eddies are resolved, however, under-resolved turbulence scales lead to instabilities of the scheme. These instabilities are

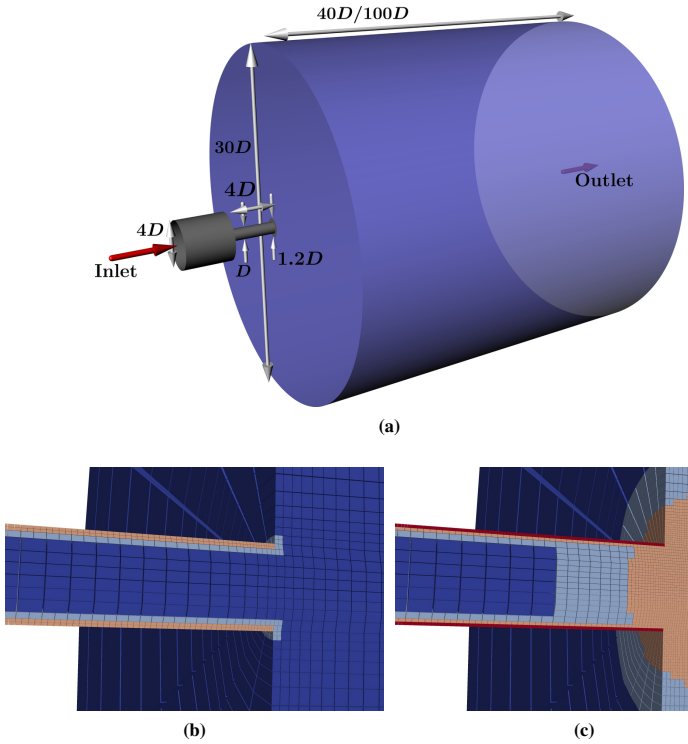

Figure 4.10.: Geometry of the simulation domain. The domain length is $L_{\text{domain}} = 40D$ for the supersonic jet and $L_{\text{domain}} = 100D$ for the subsonic jet (a). Mesh refinement for the subsonic jet (b) and the supersonic jet (c). Reproduced from [52] with permission.

detected with the Persson indicator and FV-subcells are applied at the affected elements, see Section 3.4 for a more detailed discussion.

4.2.2. Subsonic jet

To verify the methodology and numerical setup a subsonic jet is used and compared to experimental data of self-similar turbulent jets [89, 137]. The inlet pressure is set to $p_{\text{in}} = 100\,\text{bar}$, the outlet pressure to $p_{\text{out}} = 75\,\text{bar}$ and the temperature in the en-

tire domain to $T = 300\,\mathrm{K}$. Hence, the pressures are much higher than common for self-similar jets. The results, however, suggest nonetheless a good agreement with the general theory. The initial parameters lead to average throttle exit conditions for the velocity of $u_a = 227.5\,\mathrm{m\,s^{-1}}$, a density of $\rho_a = 60.40\,\mathrm{kg\,m^{-3}}$ and a Reynolds number based on the diameter of $Re_D = 5 \times 10^5$. Therefore, the flow is considered as fully turbulent within the throttle and further downstream. However, the boundary layer within the throttle is far from being fully developed, since the throttle is relatively short. The focus is on the decay rate of the velocity at the centerline and also on the radial profiles and their comparison with experimental values. As EOS the tabulated real gas data of methane is used. The simulation results are averaged over time until the profiles converged ($3 \times 10^{-3}\,\mathrm{s}$).

Figure 4.11a shows the self-similar radial velocity profile, where w is the axial velocity, w_0 is axial velocity at the centerline, r is the radius and $r_{0.5}$ is the half width of the jet. The profile is averaged in axial direction (from 35 to 45D) and additionally in radial direction. The results show good agreement to the experimental data from Panchapakesan and Lumley [89].

The inverse of the mean axial velocity is presented in Figure 4.11b, together with experimental data [89, 137], where w_J denotes the centerline velocity at the throttle exit. Again, good agreement is found between our numerical results and the experiment. The gradient of the inverse of the velocity matches the experimental data [137], but the potential core length of the jet differs. Babu and Mahesh [7, 8] concluded that by allowing for entrainment in the simulation the potential core length becomes shorter, which is observable in our results. The absence of a distinct boundary layer [6] and potential real gas effects may also contribute to a change in potential core length. Additionally, for the given Re_D an increase in DOF might lead to even better results, due to the long average time this is out of reach for the present study. To the author's knowledge, there are only little investigations self-similar jets at high pressures available. Hence, the possible influence of real gas effects to the self-similar jet is unknown.

4.2.3. Supersonic throttle flow and underexpanded jet

In the following, the real gas effects of an underexpanded supersonic jet with a pressure ratio $p_{\mathrm{in}}/p_{\mathrm{out}} = 5$ are investigated. Table 4.3 summarizes the different cases that are studied. Here, the following notation is used: RG or IG denote the type of EOS modelling. Either the tabulated Helmholtz formulation for real gas (RG) is used or the ideal gas law (IG). The numbers 500, 100, 50 denote the inlet pressure and the suffix either the viscosity model (A,B or C) or the temperature difference to the reference case RG500 (- or +). The viscosity models used are constant viscosity at $100\,\mathrm{bar}$, Sutherland formulation with a reference viscosity at $\approx 0\,\mathrm{bar}$ and Sutherland formulation with a reference viscosity at $100\,\mathrm{bar}$ for A, B and C, respectively. For all cases tabulated values are used with a sufficient accuracy. The influence of the EOS and of the different ther-

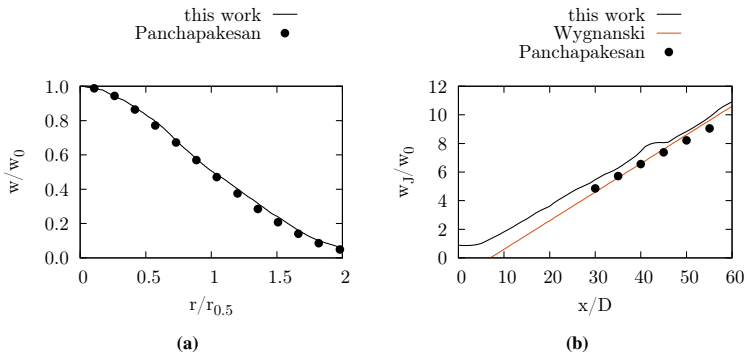

Figure 4.11.: Profiles for mean axial velocity in radial (a) and axial (b) direction. Reproduced from [52] with permission.

modynamic states are studied, i.e., variation of pressure and temperature for inlet and outlet. The simulations were run on 2400 processors and require on average approximately 1.76×10^{-5} s per time step for one DOF. The chosen thermodynamic states of the inlet and outlet are similar to modern gas injection systems. Further, at these states the thermodynamic properties of methane are particularly interesting. The compressibility factor Z for the different cases is shown in Figure 4.12a. Clearly, an accurate description of real gas properties of the fluid is required for all cases. The dynamic viscosity (Figure 4.12b) is almost pressure-independent for low pressures as for ideal gases. However, it shows a strong pressure dependence for $p \gtrsim 200\,\mathrm{bar}$. These two figures clearly show that the real thermodynamic properties differ strongly from ideal gas and Sutherland formulation and need to be taken into account for a realistic simulation.

Grid convergence

To ensure that all scales which are represented, relevant to the investigation of the supersonic jet, a grid convergence study is made. A fully grid independent solution for all scales is beyond reach for this type of scale resolving simulation. Therefore, the focus is on the representation of key features. For this purpose four different resolutions are investigated, a coarse, medium, fine and very fine grid. The coarse grid is the one used for the subsonic jet validation (cf. Fig. 4.10b), which achieved good agreement with experimental data. The medium grid is refined in the area of the shocks by a factor of two in each spatial direction in respect to the coarse grid. The fine grid is again refined by the

Table 4.3.: Investigated cases for the simulation of supersonic methane jet. Reproduced from [52] with permission.

Case	p_{in} [bar]	p_{out} [bar]	T_0 [K]	EOS
RG500	500	100	300	tabulated real gas (RG)
IG500A	500	100	300	ideal gas (IG); $\kappa = 1.234$ $\mu_0 = 1.381 \times 10^{-5}\,\text{Pa s}$
IG500B	500	100	300	IG (Suth.); $\kappa = 1.234$, $\mu_S = 1.236 \times 10^{-5}\,\text{Pa s}$
IG500C	500	100	300	IG (Suth.); $\kappa = 1.234$, $\mu_S = 1.381 \times 10^{-5}\,\text{Pa s}$
RG50	50	10	300	RG
RG100	100	20	300	RG
RG500-	500	100	275	RG
RG500+	500	100	350	RG

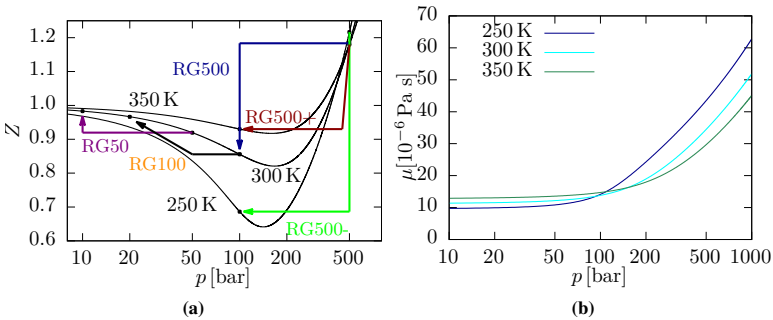

Figure 4.12.: Compressibility factor Z (a) and dynamic viscosity μ (b) of methane as functions of pressure p at different temperatures. Points and arrows indicate the conditions of the different cases. Reproduced from [52] with permission.

same factor from the medium grid and is the grid used in the following for the parameter study of the supersonic jet (cf. Figure 4.10c). Again, for the very fine grid the area of the shocks is refined. The different grid convergence simulations have 2.142×10^6, 5.358×10^6, 3.029×10^7 and 1.342×10^8 DOF, respectively.

Figure 4.13 shows the simulation results of the developing jet on different grids. At $t = 1.0 \times 10^{-5}\,\mathrm{s}$ for all grids the key features are identified, e.g., Mach disk, bow shock and tip vortex. Moving towards finer grids the structures become more clear, however, from the fine to the very fine mesh only marginal differences are present. For the next time frame the instabilities within the shear layer and the slip lines are clearly present, whilst these features become only slightly more dominant on the finest grid. It is worth noting that for the two finest grids a second tip vortex is present. Therefore, no new features are identified from the fine to the very fine grid. Similar at $t = 2.5 \times 10^{-5}\,\mathrm{s}$ for the two finest meshes the key features agree well with each other.

Further, 3D iso surfaces of the density are compared for the different grid resolutions. Figure 4.14 shows the iso surfaces for density $\rho < 55\,\mathrm{kg\,m^{-3}}$ and $\rho > 90\,\mathrm{kg\,m^{-3}}$ at $1.5 \times 10^{-5}\,\mathrm{s}$ for the different grids. With the coarse grid only the shock, i.e., regions with very low and very high density, are visible in the simulation results. With the middle resolution grid very large turbulent structures in the area of the second high density zone are present. The structures are less axis symmetric than for the coarser grid. The fine grid shows far more turbulent structures compared with the coarser meshes. Further, these structures are most dominant around the first shock location, i.e., between the first low density and second high density zone. For this grid resolution, two important features are represented by the simulation, e.g., the second shock and a second tip vortex, c.f., the discussion for Figure 4.13. The simulation results for the finest grid show higher resolution for the turbulent scales and structures of the first tip vortex. However, the location remains unchanged compared to the fine grid. Consequently, the fine gird is capable of representing all important effects and therefore it is used for the parameter study.

Flow development

Here, the transient flow development of the supersonic under-expanded jet is analyzed. The reference case RG500 is used to demonstrate the core features of such a jet. The initial pressure in the domain is set to the outlet pressure. Consequently, the high pressure propagates through the throttle. Figure 4.15 illustrates the density downstream of the throttle at different times t. At the early stages of the jet development a bow shock propagates downstream, as shown in Figure 4.15a. It is caused by the pressure pulse through the throttle. At this stage a tip vortex forms. First shock structures develop: a Mach disk, an expansion wave and oblique shocks. At this stage the jet propagates approximately two diameters downstream of the throttle exit.

In Figure 4.15b, at $t = 1.5 \times 10^{-5}\,\mathrm{s}$, the jet propagated to $5D$ downstream of the

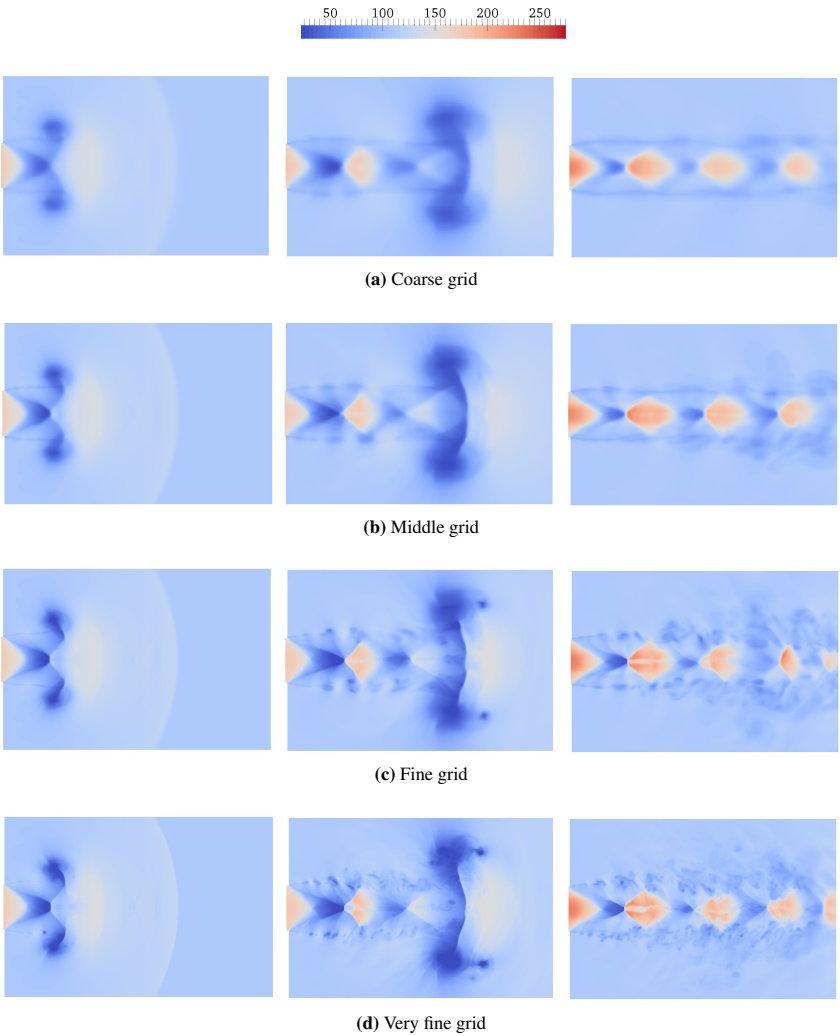

(a) Coarse grid

(b) Middle grid

(c) Fine grid

(d) Very fine grid

Figure 4.13.: Density for different grid resolutions at different times, $t = 1.0 \times 10^{-5}$ s, 1.5×10^{-5} s and 2.5×10^{-5} s from left to right. Figures for $t = 1.5 \times 10^{-5}$ s, reproduced from [52] with permission.

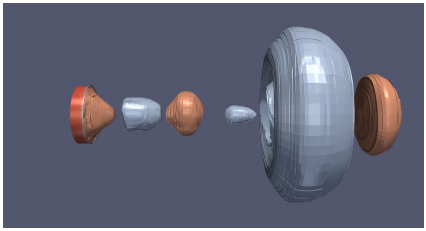

(a) Coarse grid

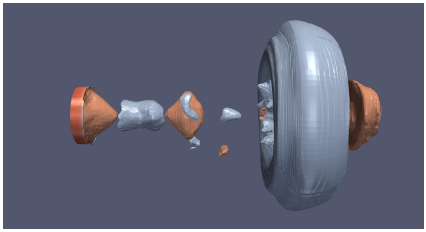

(b) Middle grid

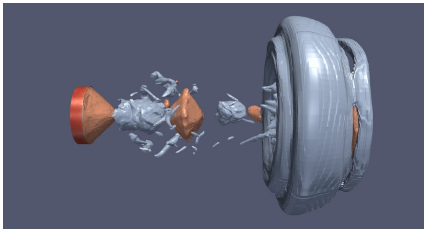

(c) Fine grid

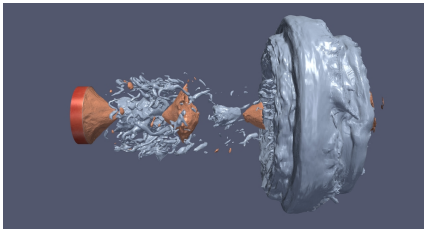

(d) Very fine grid

Figure 4.14.: Grid convergence study iso surfaces for density smaller than $55\,\mathrm{kg\,m^{-3}}$ and larger than $90\,\mathrm{kg\,m^{-3}}$ at $1.5 \times 10^{-5}\,\mathrm{s}$. Reproduced from [52] with permission.

throttle exit. The width of the first shock shrinks and two very close slip lines are generated at these Mach reflection triple points. Further, a typical diamond shape with two shock fronts develops, and turbulent instabilities are generated at the shear layer. The tip vortex spreads in radial direction in addition to its propagation downstream and has also induced a second smaller ring vortex.

From $t = 2.5 \times 10^{-5}$ s to 3.0×10^{-5} s (Figures 4.15d and 4.15e) two normal shocks are generated. There, slip discontinuities can be observed. With a decreasing pressure at the throttle exit, the normal shock shrinks and is no longer present at $t = 3.5 \times 10^{-5}$ s. Additionally, the density increases within the jet.

Later (Figure 4.15g) the under expansion of the jet at the throttle exit is only marginal. The jet becomes narrower than at the earlier stages. Two oblique shocks are present, which move further upstream. At $t = 6.0 \times 10^{-5}$ s these shocks move from the throttle exit into the throttle. Hence, the simulation predicts a pressure decrease at the throttle exit at a certain stage in the jet development and the jet is no longer under-expanded and free of normal shocks.

Figure 4.16 shows the transient behavior of the ratio of the pressure at a given position compared to the pressure at the outlet within the throttle. At $t = 1.0 \times 10^{-5}$ s (Figure 4.16a) a small pressure drop occurs downstream of the throttle inlet. In Figure 4.16b a shock begins to form at the throttle inlet. Consequently, the pressure within the throttle drops and influences the flow field downstream of the throttle.

Later, at $t = 3.0 \times 10^{-5}$ s in Figure 4.16c, oblique shocks form at the throttle inlet. Here, the pressure drop signal travels through the throttle, as shown in the figure at approximately the middle of the throttle. At $t = 6.0 \times 10^{-5}$ s four oblique shocks and their reflections contribute to a strong pressure drop within the throttle. This caused the throttle exit pressure to be almost equal to the outlet pressure. At the exit two shocks are very close to each other. The first is a shock reflection from within the nozzle. Consequently, only weak under-expanded jet phenomena are present downstream of the exit (cf. Figure 4.15h).

An important parameter for the gas injection is the mass flow. The mass flow rate at the throttle exit is shown in Figure 4.17. Until about $t = 1.1 \times 10^{-5}$ s the critical cross section is at the throttle exit, due to the expansion of the jet. Afterwards, a critical cross section develops at the throttle inlet, which is the limiting factor for the mass flow rate. This change causes a slight dent of the mass flow curve. From $t = 1.5 \times 10^{-5}$ s to 8.0×10^{-5} s mass flow increases at an almost constant rate. The simulation results suggest that this is caused by the development of a converging flow at the throttle inlet. First, the flow from the inlet propagates almost homogeneously towards the throttle. However, parts of the flow stagnate at the wall and increase the temperature. Later, the flow adjusts and the temperature and Z at the throttle inlet decrease, due to the aforementioned converging flow. At $t = 8.0 \times 10^{-5}$ s the flow within the throttle reaches a quasi-steady state and the mass flow remains almost constant.

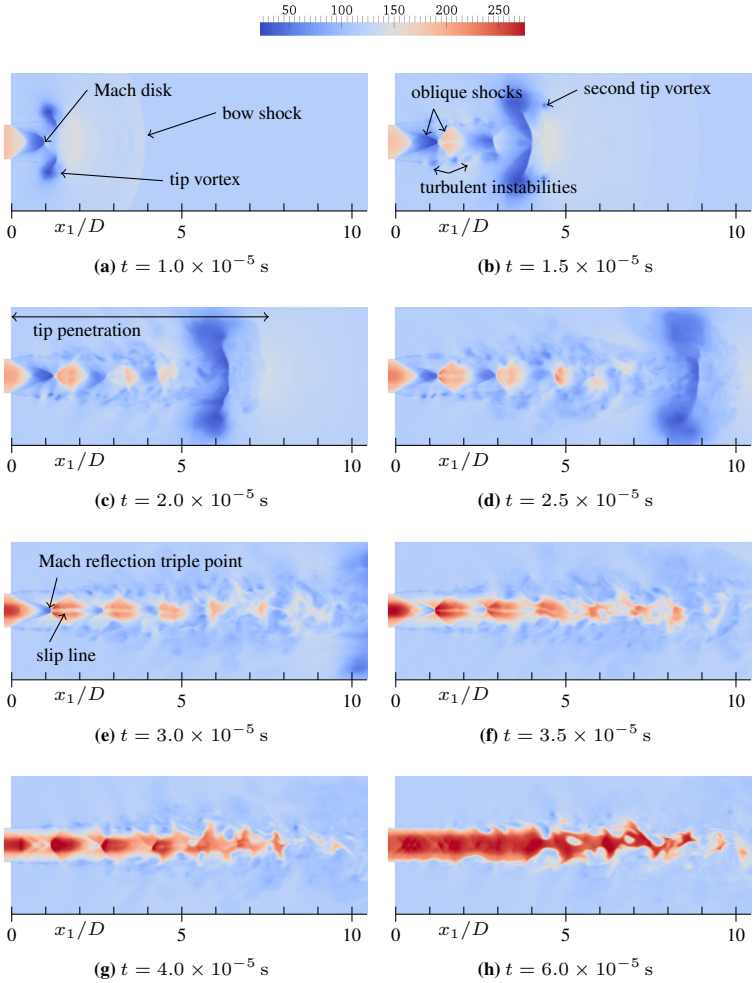

(a) $t = 1.0 \times 10^{-5}$ s **(b)** $t = 1.5 \times 10^{-5}$ s

(c) $t = 2.0 \times 10^{-5}$ s **(d)** $t = 2.5 \times 10^{-5}$ s

(e) $t = 3.0 \times 10^{-5}$ s **(f)** $t = 3.5 \times 10^{-5}$ s

(g) $t = 4.0 \times 10^{-5}$ s **(h)** $t = 6.0 \times 10^{-5}$ s

Figure 4.15.: Density [$\mathrm{kg\,m^{-3}}$] contours during the development of the supersonic jet. Reproduced from [52] with permission.

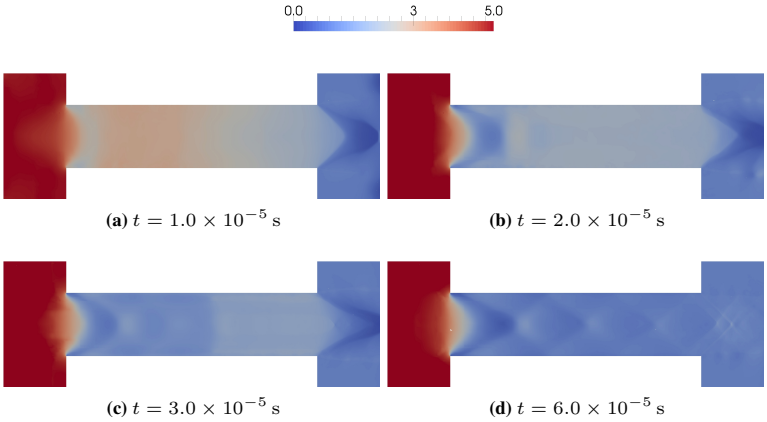

Figure 4.16.: Pressure ratio (p/p_{out}) within the throttle for RG500 at different times t. Reproduced from [52] with permission.

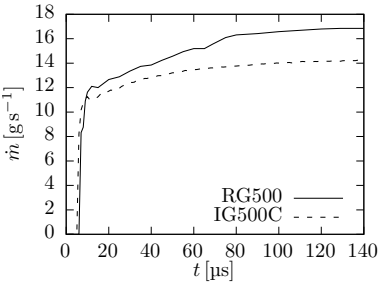

Figure 4.17.: Mass flow at the throttle exit for RG500. Reproduced from [52] with permission.

Further, the velocity and temperature field is presented in Figure 4.18. From the velocity the shocks are clearly visible and the turbulence generation in the shear layers is represented. Downstream of the shocks the velocity field resembles a subsonic jet. The temperature varies strongly from the initial temperature of $T_0 = 300\,\text{K}$. Especially before the first shock the temperature drops strongly and rises across the shock. In the shear layer the temperature increases from the initial condition.

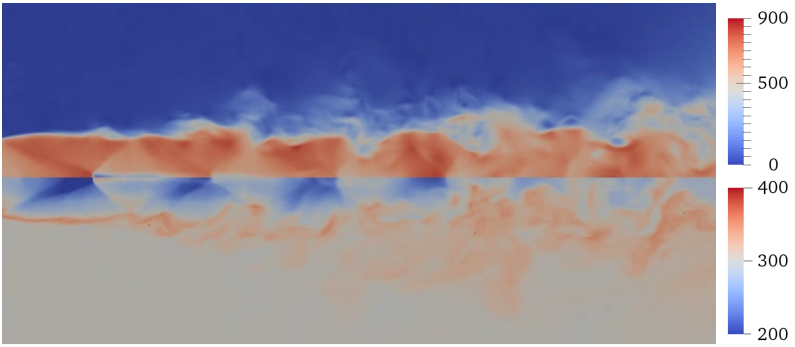

Figure 4.18.: Velocity [$\mathrm{m\,s^{-1}}$] (top) and temperature [K] (bottom) for the RG500 at $t = 3.0 \times 10^{-5}\,\mathrm{s}$.

It is worth noting, that the methane jet enters the two-phase region, where liquid and gas coexist in an equilibrium state, during two different times at two different locations: From $t = 2.4 \times 10^{-5}\,\mathrm{s}$ to $4.0 \times 10^{-5}\,\mathrm{s}$ before the first shock and for $t > 7.3 \times 10^{-5}\,\mathrm{s}$ within the throttle upstream of the shock position. The thermodynamic path into the two-phase region is from the gaseous phase and remains in a region with a high mass vapor fraction. In the early stages, the phase change is responsible for a limitation of the temperature before the shock, i.e., T_{min}, which is discussed in greater detail in Section 4.2.3.

Influence of real gas and viscosity effects

As aforementioned, commonly used real gas EOS representations are, e.g., the Peng-Robinson model [91] and similar approaches. However, with the use of a tabulated EOS the evaluation is done as part of the pre-processing. Therefore, computationally expensive, but highly accurate EOS become feasible, i.e., the Helmholtz formulation. The proposed framework is compared to the fastest available EOS, e.g., ideal gas in tabulated form and commonly used viscosity models. For the ideal gas case IG500A a constant viscosity $\mu_0 = 1.381 \times 10^{-5}\,\mathrm{Pa\,s}$ is used and for the temperature-dependent viscosity models (IG500B/C), the Sutherland formulation Equation (2.36) is applied; here, $T_{\mathrm{S}} = 300\,\mathrm{K}$ and $S = 190\,\mathrm{K}$. Two different μ_{S} are used; $1.125 \times 10^{-5}\,\mathrm{Pa\,s}$ ($p \approx 0$ Pa) and $1.381 \times 10^{-5}\,\mathrm{Pa\,s}$ (p_{out}) for IG500B and IG500C, respectively. The flow at $t = 3.0 \times 10^{-5}\,\mathrm{s}$ is compared for a detailed evaluation of different initial conditions or EOS modelings, because at this stage the throttle exit conditions generate an under-expanded supersonic jet, which allows a comparison of the shock positions and

the corresponding flow structures. Additionally, the mass flow rate over time and the jet development of the IG500C case with the real gas case is analyzed.

The focus is on the flow regime downstream of the throttle exit. In Figure 4.19 the pressure ratio (p/p_{out}) is shown. First, the location and width of the first shock are examined, see Table 4.4. The most distinct feature is the difference in shock width. Whilst for RG500 only a very small shock front is present, the shocks for an ideal gas are wider. The normal shock for RG500 is 2 to 3 times smaller than for IG500A and IG500B/C, respectively. It is also located closer to the throttle exit than for the ideal gas cases in the simulation. For IG500A the normal shock is wider than for IG500B/C. For RG500 a second, very narrow, normal shock is present, whilst for the ideal gas cases only oblique shocks with a low intensity can be observed.

The ideal gas cases emit pressure waves, which originated from the throttle exit and the generated shear layer. For RG500 these pressure waves are less intense. This is due to the different throttle exit pressures and consequently, a more under-expanded jet for the ideal gas [120].

Figure 4.20 shows the density for the development of the supersonic jet for the ideal gas case IG500C. During the early stage, $t < 3.5 \times 10^{-5}$ s, the jet shows similar features as with the real gas EOS. A difference is the more distinct normal shock front of the first shock. This is discussed for Figure 4.19c and is due to the larger expansion in the throttle inlet. The most dominant differences occur for $t > 3.5 \times 10^{-5}$ s. For the real gas EOS the under-expansion of the jet vanishes, however, for the ideal gas cases the under-expansion remains throughout the analyzed time steps. Within the throttle no shocks are present for the IG500C and consequently the pressure drop within the throttle

Table 4.4.: First shock width W and height H compared to the throttle diameter D. Reproduced from [52] with permission.

Case	W/D	H/D
RG500	0.1098	1.169
IG500A	0.3218	1.279
IG500B	0.2392	1.289
IG500C	0.2358	1.286
RG50	0.2255	1.264
RG100	0.1082	1.375
RG500-	II	1.074
RG500+	II	1.291

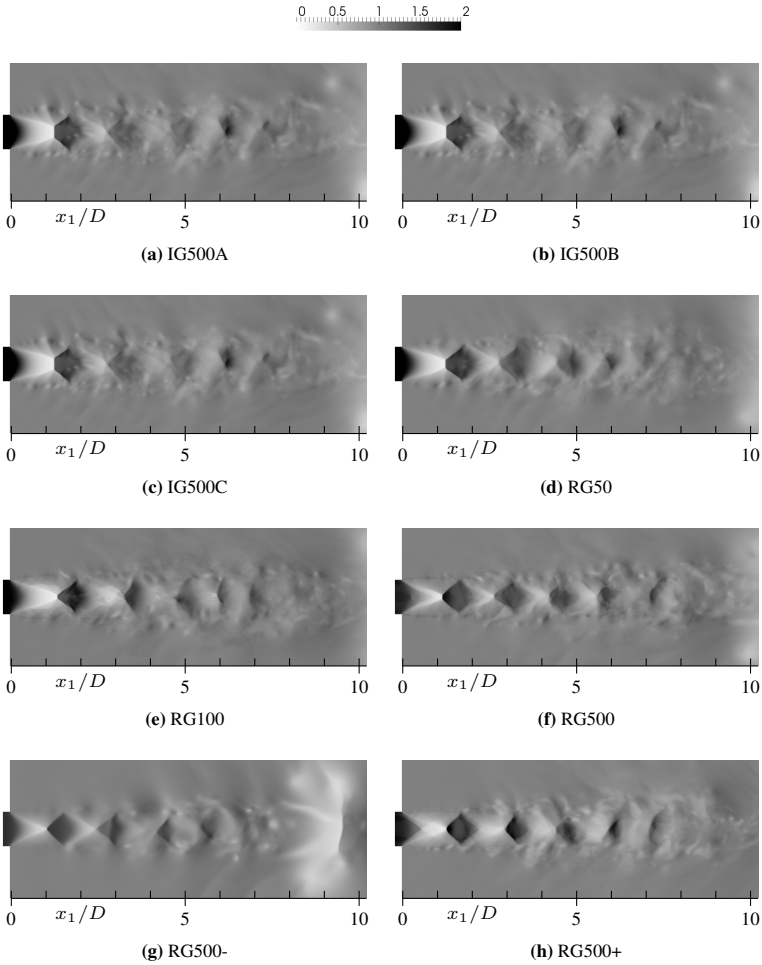

(a) IG500A **(b)** IG500B

(c) IG500C **(d)** RG50

(e) RG100 **(f)** RG500

(g) RG500- **(h)** RG500+

Figure 4.19.: Pressure ratio (p/p_{out}) at $t = 3 \times 10^{-5}$ s for different EOS models. Reproduced from [52] with permission.

is far less.

Table 4.5 gives an overview of the mass flow, the maximum and minimum T, p and ρ and the maximum velocity u at $t = 3.0 \times 10^{-5}\,\mathrm{s}$ and $x > 0$. The mass flow for RG500 amounts to $13.36\,\mathrm{g\,s^{-1}}$ and to $12.9\,\mathrm{g\,s^{-1}}$, $12.06\,\mathrm{g\,s^{-1}}$ and $12.63\,\mathrm{g\,s^{-1}}$ for IG500A/B/C, respectively. This is a deviation of $3.2\,\%$ to $9.7\,\%$ with the Sutherland formulations showing the largest differences. The more the dynamic viscosity differs from RG500 upstream of the throttle, the greater is the difference in the mass flow. This suggests a strong influence of the viscosity for the mass flow. Clearly, real gas effects influence the flow behavior, whilst the influence of the viscosity modeling for ideal gas is only notable within the throttle. In Figure 4.17 the mass flow over time for IG500C is compared to RG500. The general trend is similar, however, at later stages the difference in mass flow increases due to the compressibility.

Influence of pressure ratio to mass flow rate

A key value for the design of components is the mass flow rate. Therefore, the influence of different pressure differences between the inlet and outlet is examined and the mass flow rate over time are discussed. Here, the mesh from the subsonic jet was used to reduce the computational costs, because the simulation time needed to be relatively long to ensure converged mass flow rate. The investigated pressure ratios PR $= p_{\mathrm{in}}/p_{\mathrm{out}}$ were 1.25, 1.67, 2.50, 2.86, 3.33 and 5.00 at a constant $p_{\mathrm{in}} = 500\,\mathrm{bar}$. Figure 4.21a shows the mass flow rate over time for the different PR. At a PR $= 1.25$ the flow is fully subsonic and the mass flow rate reaches a quasi-constant value at around $t > 2.3 \times 10^{-5}\,\mathrm{s}$. Similarly, at PR $= 1.67$ the mass flow rate converges to an almost constant value very early compared to the higher pressure ratios. However, here the mass flow has increased from about $10.5\,\mathrm{g\,s^{-1}}$ to $14.0\,\mathrm{g\,s^{-1}}$ for PR $= 1.25$ and PR $= 1.67$, respectively. For a PR $= 2.50$ the mass flow rate rises very rapidly at first. After this first increase, the mass flow rate continues to rise slowly until approximately $t = 12.0 \times 10^{-5}\,\mathrm{s}$. At this time the flow is not fully chocked, however, the limitation of the mass flow rate, i.e., the critical cross section, has moved from the throttle outlet to the throttle inlet. By increasing the pressure ratio to PR $= 2.86$ and higher the mass flow rate becomes chocked and the mass flow is not further increased with a higher pressure ratio. Similarly, Figure 4.21b shows the average mass flow rate for the different operating points.

Influence of inlet pressure with constant pressure ratio

The influence of varying inlet pressures on the jet is studied, while maintaining a constant pressure ratio between inlet and outlet, $p_{\mathrm{in}}/p_{\mathrm{out}}$. Figures 4.19d to 4.19f show the pressure ratio for RG50, RG100 and RG500, respectively. The shock width of RG50

[II] No normal shock present ($W/D < 0.05$).

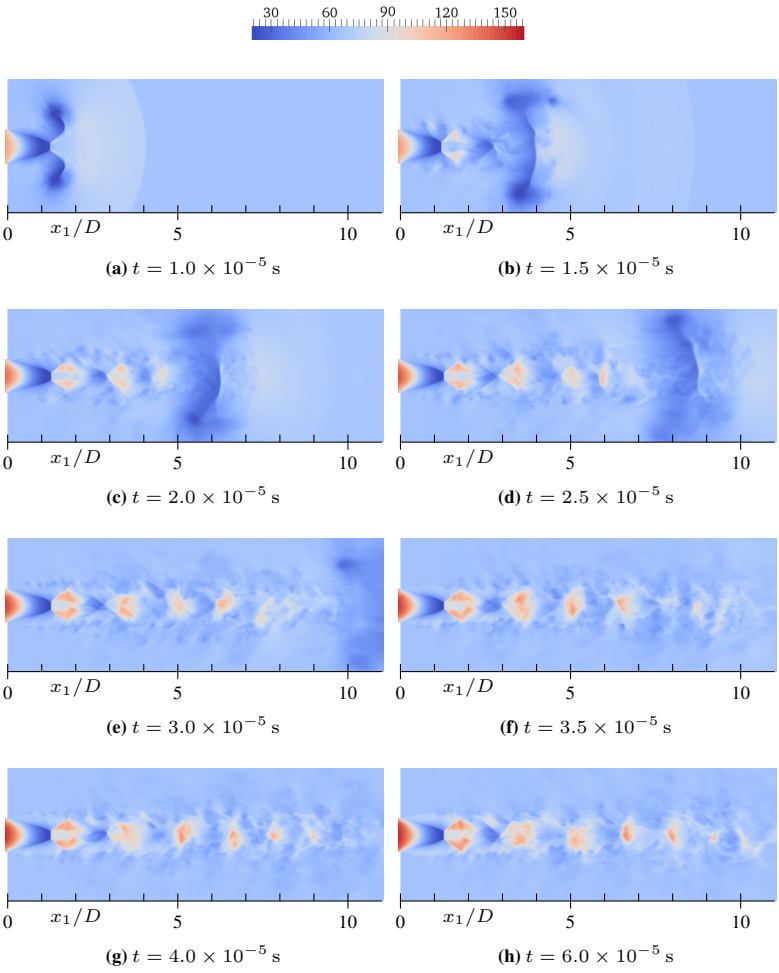

(a) $t = 1.0 \times 10^{-5}$ s **(b)** $t = 1.5 \times 10^{-5}$ s

(c) $t = 2.0 \times 10^{-5}$ s **(d)** $t = 2.5 \times 10^{-5}$ s

(e) $t = 3.0 \times 10^{-5}$ s **(f)** $t = 3.5 \times 10^{-5}$ s

(g) $t = 4.0 \times 10^{-5}$ s **(h)** $t = 6.0 \times 10^{-5}$ s

Figure 4.20.: Density [$\mathrm{kg\,m^{-3}}$] contours during the development of the supersonic jet for IG500C. Reproduced from [52] with permission.

Table 4.5.: Summary of the simulation results for the investigated cases ($t = 3.0 \times 10^{-5}$ s, $x_1 > 0$).

		T [K]		p [MPa]		ρ [kg m^{-3}]		w [m s^{-1}]
Case	$\dot{m}$ [g s^{-1}]	max	min	max	min	max	min	max
RG500	13.36	353.5	164.6	19.14	1.905	160.7	34.22	865.1
IG500A	12.93	382.9	167.8	22.52	1.588	157.0	18.26	915.0
IG500B	12.06	339.7	165.4	20.71	1.554	147.3	18.00	917.8
IG500C	12.63	340.5	166.1	20.63	1.567	147.0	18.12	916.9
RG50	1.294	344.0	132.7	2.114	0.1436	16.27	2.128	864.7
RG100	2.690	353.1	124.3	4.028	0.2420	33.48	3.997	856.9
RG500-	15.15	298.7	179.1	16.52	2.717	182.6	38.92	812.6
RG500+	11.85	399.3	163.5	22.75	1.798	144.7	26.88	913.4

is closest to the ideal gas cases. RG100 has the smallest normal shock, but it is furthest downstream. A possible reason could be the low compressibility and the absence of a phase change. RG500 shows the highest pressure increase across the shock. The shock location starts to vary for the different cases, see Table 4.4. For many properties, e.g., temperature or mass flow the trend from RG50 to RG100 cannot be extrapolated to RG500. Since there is no phase change for RG50 and RG100 no latent heat of evaporation is required. Additionally, viscosity and compressibility are significantly different at pressures higher than 100 bar. The change in compressibility causes the mass flow to be no longer proportional to the pressure (see Table 4.5). For RG100 and RG500 the mass flow compared to RG50 is over- and under-proportional to pressure, respectively. Further, T_{min} is significantly lower for RG100 and RG50 than for RG500. The cases with lower pressure experience no phase transition and therefore the temperature drops further before the first shock.

Influence of temperature

The compressibility factor depends weakly on temperature at 500 bar. However, at 100 bar the influence is significant (see Figure 4.12a). Within the flow the gas in the jet experiences a phase change in the RG500- and RG500 cases. The equation of state must cover this two-phase region even though this occurs only in a small region.

Figures 4.19f to 4.19h show the pressure ratio (p/p_{out}) at $t = 3 \times 10^{-5}$ s for RG500, RG500- and RG500+, respectively. The jet with the lower temperatures has a shorter tip penetration, but an increased mass flow. For RG500+ the rarefraction wave, which crosses the jet centerline before the first shock, is clearly present. At the position, where

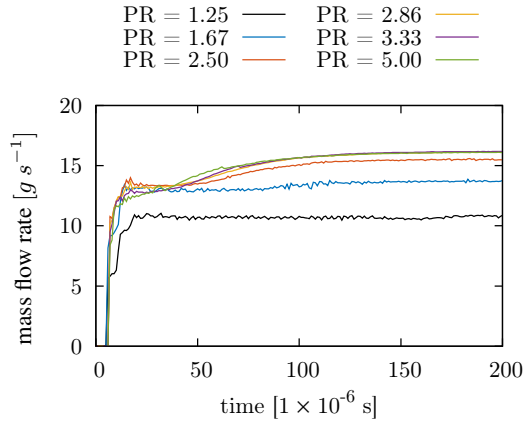

(a)

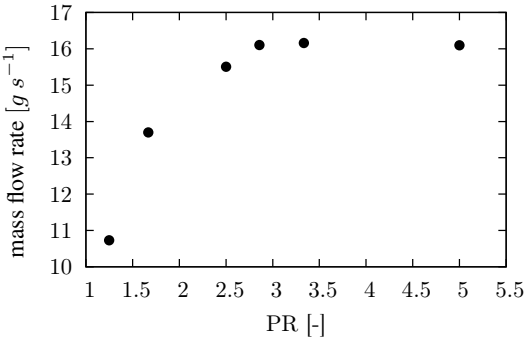

(b)

Figure 4.21.: Mass flow rate for different pressure ratios with a fixed $p_{\text{in}} = 500\,\text{bar}$. Reproduced from [53] with permission.

the oblique shocks meet, no normal shock occurs for RG500-/+.

The higher T_{min} for RG500 and RG500- compared to RG500+ is due to the phase change. During the phase change the temperature change is limited. To illustrate the thermodynamic path during the phase change, the RG500- at the location of the first

shock was analyzed. Fig. 4.22 shows temperature T, pressure p, speed of sound a, Mach number Ma and vapor mass fraction x along the center line downstream of the throttle exit. There the jet entered the two-phase region the most out of all cases and therefore the effects are the clearest. For RG500- the slope, at which the temperature decreases before the shock becomes shallow as soon as the medium is in the two-phase region, i.e., with a vapor mass fraction $x < 1$. For the pressure the influence is less clear. Further, the phase change limits the decrease of the speed of sound. Hence, the local Mach number increases only marginally shortly before the shock position.

Case RG500- enters the two-phase region at a higher temperature; therefore, the heat of evaporation is higher. Consequently, the temperature drop is limited most significantly and T_{min} is higher than for the other cases. Further, the simulation results suggest that the phase change has a strong influence on the local Mach number and other flow properties.

4.2.4. Shock capturing and treatment of under resolved scales

In the present work, the discontinuous Galerkin method is used. To avoid Gibbs type oscillations a FV subcell technique is applied [111]. To detect the affected DG elements a indicator proposed by Persson and Peraire [92] is applied. This detection is independent of the EOS approximation. Therefore, the shock capturing is only analyzed for the RG500 case.

Figure 4.23 shows the indicator values and the FV elements for the developing RG500 jet (cf. Figure 4.15). At $t = 1.0 \times 10^{-5}$ s (in Figure 4.23a) downstream of the bow shock the values of the indicator are very low. The fluid is at rest and therefore no oscillations are detected. The indicator is able to detect the instabilities nicely. Only occasionally elements without shocks or strong gradients are detected. However, the tip vortex also needs stabilization due to the lack of an explicit Subgrid Scale (SGS) model. Here, the FV subcells increase the dissipation and represent a very simple implicit SGS model. With this technique good agreement for similar flows of the supersonic jet with acoustics was achieved [54]. For Figure 4.23b and Figure 4.23c the shocks and other instabilities are detected. The flow becomes more turbulent and more FV elements are present to stabilize under-resolved turbulent scales. At $t = 1.0 \times 10^{-5}$ s (in Figure 4.23d) only very weak shocks are present downstream of the throttle exit and therefore the majority of the FV subcells are present in the shear layers of the jet.

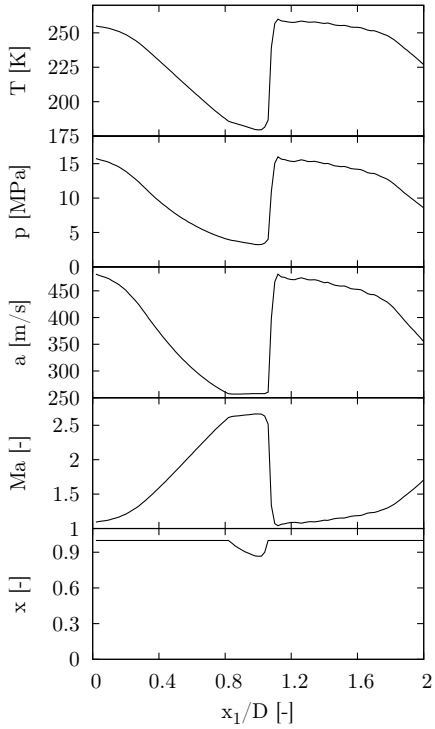

Figure 4.22.: Thermodynamic variables along the centerline at the first shock location at $t = 3 \times 10^{-5}$ s for RG500-. Reproduced from [52] with permission.

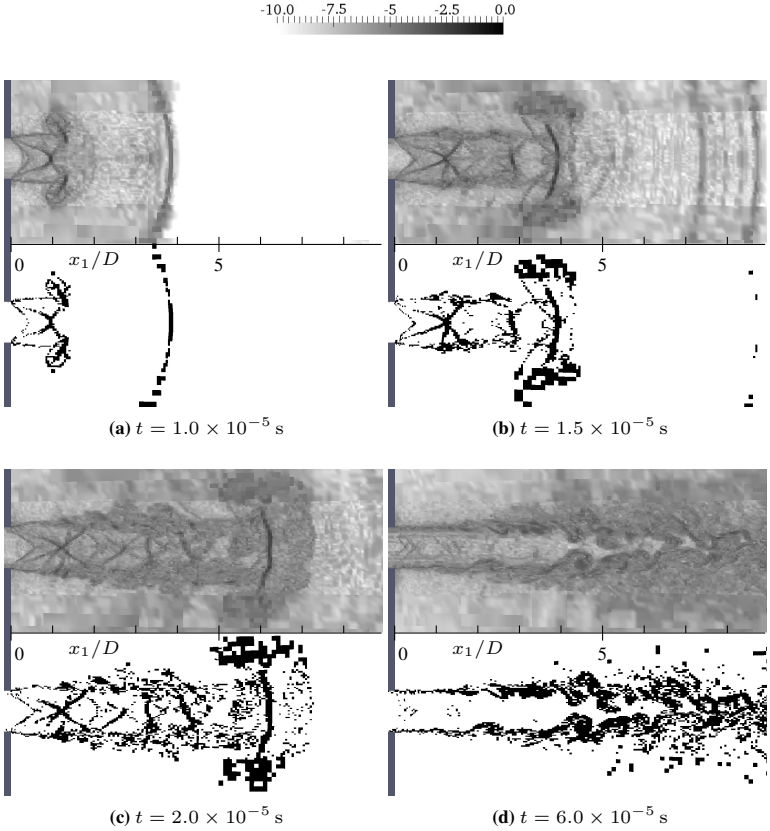

(a) $t = 1.0 \times 10^{-5}\,\mathrm{s}$ **(b)** $t = 1.5 \times 10^{-5}\,\mathrm{s}$

(c) $t = 2.0 \times 10^{-5}\,\mathrm{s}$ **(d)** $t = 6.0 \times 10^{-5}\,\mathrm{s}$

Figure 4.23.: Shock indicator value (top, with label) and FV elements (bottom, FV elements in black) for the developing real gas jet RG500.

4.3. Conclusion of the gas dynamics simulation

In this section the influence of real gas effects was assessed for 1D shock tube experiments and 3D high Reynolds number supersonic jets. The simulations show a strong derivation to the ideal gas implementation for high pressures and even small differences at low pressures for non-noble gases.

From the shock tube experiment it was found that the simulations were thermodynamically consistent with the analytical results for the isentropic relation. Further, for the real gas approximation the results converged at low pressures and showed very little difference. However, even at very low pressures differences between the ideal and real gas approximation was observed.

In the present chapter, the effects of the used real gas modeling for the simulation of methane jets were examined, e.g., on temperature, pressure and viscosity. Code validation was carried out for a subsonic jet with a tabulated equation of state and good agreement was found with the experimental data [89, 137].

Further, the development of the high pressure supersonic jet showed well-resolved results and similar features could be identified as described in the literature [129]. The position of the critical cross section, which limits the mass flow, changed during the transient jet development. The mass flow rate increase occurred at different stages over time: first a rapid increase due to initial flow and second a moderate increase as a result of the adjusting to a quasi-steady state with constant mass flow. The Helmholtz free energy EOS was compared with the ideal gas formulation. It has been shown that the flow structure, e.g., shock locations, were very sensitive to the modeling of the viscosity in the present simulation. Therefore, for high pressure jets, the dependence of pressure on the viscosity cannot be neglected, i.e., the standard Sutherland formulation is inadequate here. At flow regions with higher pressures real gas modeling was required. The mass flow and other fluid properties showed significant differences for the different EOS and the dynamic viscosity modeling. The importance of the modeling of real gas properties was demonstrated, e.g., Z and $\mu(p, T)$. Additionally, the pressure level of the inlet and outlet were examined, while the pressure ratio was kept constant for all supersonic jets. A strong influence was found for a number of flow features, e.g., the shock location and width. Further, the influence of the inlet and outlet temperature was analyzed. It was found that for cases with temperatures $250\,\mathrm{K}$ and $300\,\mathrm{K}$ a phase change occurred, while for $350\,\mathrm{K}$ the fluid remained slightly above the evaporation line. The transition of phases before the first shock had a strong influence on the thermodynamic properties, e.g., T_{min}.

To summarize the key findings of the present chapter:

- The proposed tabulated EOS representation is a flexible and efficient alternative for an analytical real gas EOS and allows for multi-phase EOS
- The simulation results suggest that real gas effects strongly influence flow features, e.g. mass flow, shock location and pressure ratio

- The position of the two-phase region changed during the stages of the jet development

5. Cavitation

The following chapter gives further insights into the behavior of the applied method, i.e., dense gas approach with the thermodynamic equilibrium model. First, bubble collapses are investigated in a detailed parameter study. The focus is here to validate and verify the used framework and gain a better understanding of the implication towards more complex flows. Such complex flows, e.g., micro channel flow, are investigated in the second part of the chapter. Here, the high potential of the high-order DG scheme for cavitational flows is shown.

5.1. Single bubble collapse

The thermodynamic process, which occurs during cavitation can be very complex. To get a better understanding on the phenomena itself and its representation by the applied methodology a detailed analysis of its fundamentals is necessary. Therefore, a single bubble collapse is analyzed in detail both in 2D and 3D. The investigations included without limitation: a comparison of vapor bubbles and bubble clouds[I], validation to analytical and experimental data for collapses with and without wall interactions, grid dependency study and comparison of different cross flow velocities.

5.1.1. Numerical setup

The computational domain is large enough so no reflection of the rarefaction wave interacts with the bubble. For both 2D and 3D cases the far field boundary condition is set to weakly imposed Dirichlet, so entrainment is possible. However, the computational domain is chosen large enough so only very little entrainment occurs within the simulation. The viscose effects are neglected at the wall. The computational meshes surrounding the bubble event are uniform and grid stretching is only applied in the far-field. For the 3D case, hanging nodes are introduced in the far field to reduce the computational costs. The different meshes are characterized by then number of DOF which discretize the initial bubble in one axis, i.e., $\text{length}_{\text{cell edge}} = D_{\text{bubble}}/\text{DOF}$.

Figure 5.1 summarizes the notation of the numerical setup. The simulation is initialized with the maximum bubble radius $R_0 = 1 \times 10^{-3}\,\text{m}$ and $r(t)$ denotes the bubble

[1]The term bubble cloud is used when the fluid is in a vapor mixture state, i.e, $0 < x < 1$. Due to the averaging of the homogeneous state model the single small vapor bubbles are approximated as a vapor mixture region, here called bubble cloud.

radius which is a function of time. For a collapse without a wall the initial wall distance H and collapse distance h are meaningless. The cross flow velocity is denoted as u_0 and is set to 0 unless otherwise mentioned.

5.1.2. Spherical vapor bubble versus spherical bubble cloud collapses

As discussed in Section 3.6.1, pure gas in a liquid flow due to cavitation rarely occurs with the HEM. Averaging the states over a finite volume can result in a corresponding state within the two phase region. In the literature values for the vapor volume fraction range over a wide spectrum, e.g., in Egerer et al. [36] $\alpha = 1 \times 10^{-4}$, Hickel et al. [55] $\alpha = 1 \times 10^{-5}$, Mihatsch et al. [82] $\alpha = 1 \times 10^{-1}$ and Wei et al. [135] $\alpha = 0.9$. Similarly, Ganesh et al. [44] showed experimentally that the volume fraction, α, can range over a wide spectrum. Since all these states within the two phase region are mixtures or cloud cavitation, a comparison of a vapor bubble collapse and bubble cloud collapse is carried out.

First, a 2D simulation of a collapsing bubble without a wall is performed. Here only two different initial states are chosen, i.e., a vapor bubble and a bubble cloud with $x = 1 \times 10^{-5}$ respectively $\alpha = 0.0798$. The initial states are summarized in Table 5.1.

To avoid unintentional interactions between DG and FV only the FV scheme is used for this case. The LF Riemann solver[II] is used in a combination with a low CFL number, CFL $= 0.1$, to maintain a stable simulation[III].

The time t is non-dimensionalized by the collapse time t_{col}

$$t^* = \frac{t}{t_{\text{col}}} \tag{5.1}$$

The time of the 2D collapse for the vapor bubble is $t_{\text{col,VB}} = 6.593 \times 10^{-5}\,\text{s}$ and for the bubble cloud is $t_{\text{col,BC}} = 1.618 \times 10^{-5}\,\text{s}$. This is a difference for the collapse time of a factor of more than 4. By neglecting the surface tension and gas inside the bubble Equation (2.41) can be written as

$$\frac{p_{\text{B}}(t) - p_\infty(t)}{\rho_{\text{l}}} = r\frac{\partial^2 r}{\partial t^2} + \frac{3}{2}\left(\frac{\partial r}{\partial t}\right)^2 + \frac{4\mu_{\text{l}}}{\rho_{\text{l}} r}\frac{\partial r}{\partial t}. \tag{5.2}$$

In Figure 5.2 a collapse for a 2D simulation is presented. The purpose is here to verify the results achieved with a 2D setup. Here, three different cases, Bubble Cloud (BC), Vapor Bubble (VB) and a VB at $T = 293\,\text{K}$ are compared to Equation (5.2). The time at the abscissa is normalized with the collapse time of each case. The general trend matches the analytical Equation (5.2). The difference between the different temperatures

[II] For the bubble cloud case only the LF is able to remain stable.

[III] For the bubble cloud case a CFL $= 0.9$ would have been possible. However, it is set to the same as for the vapor bubble to remain consistent.

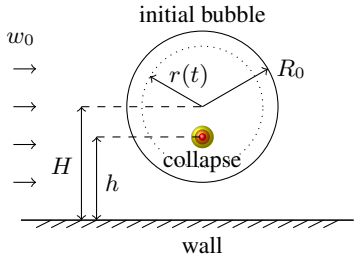

Figure 5.1.: Schematic of a initialization of the bubble collapse simulation, where $r(t)$ denotes the bubble radius over time, $R_0 = r(t = 0)$ the initial bubble radius, H the distance of the initial bubble center to the wall, h the collapse distance to the wall and w_0 the cross flow velocity.

Table 5.1.: Initial states of spherical vapor bubble and spherical bubble cloud collapses.

	far field ∞	vapor bubble (VB)	bubble cloud (BC)
$\rho(t=0)$ [kg m^{-3}]	985.2	0.0989	906.2
$T(t=0)$ [K]	330.0	330.0	330.0
$p(t=0)$ [Pa]	1.000×10^6	1.500×10^4	1.721×10^4

is only marginal. Compared to the analytical equation the curve is slightly lower and consequently not as steep shortly before the final collapse. For the bubble cloud, i.e., the initial state is in the two-phase region, the curve is lower than for the vapor bubble. Concluding for the comparison of the 2D simulation, the results compare well with the analytical equation. However, the observed difference is might partly be due to the reduction in dimension.

Figure 5.2 shows the collapse of a 3D vapor bubble in comparison with different Rayleigh-Plesset equations. The initial states correspond to VB in Table 5.2. The abscissa is time in micro seconds and the ordinate is the dimensionless bubble radius. The constant k in Equation (2.41) denotes the thermal effects of the air within the bubble, i.e., $k = 1.4$ is adiabatic and $k = 0$ is for no thermal effects. The simulation results agree well with both versions of Equation (2.41). Due to the lack of desolved gas the bubble collapses in the simulation until it completely vanishes. Compared to Equation (5.2) the duration of the collapse in the simulation takes longer. Equation (5.2) represents the simplification of the HEM best. However, in the simulation thermal effects of the liquid

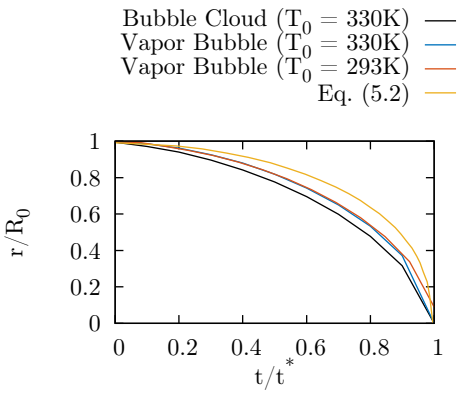

Figure 5.2.: Radius for the 2D collapse of a bubble cloud, a vapor bubble and Rayleigh-Plesset Equation (5.2).

and the gaseous phase are considered. This and the general derivation of the Rayleigh-Plesset equation therefore might lead to different results. Generally, the agreement of the simulation is very good and is able to represent the collapse dynamics.

In the following, the change in density, temperature, pressure, velocity and sound speed, from $r = 0$ to 2 R_0 are discussed for the bubble cloud and the vapor bubble simulation in 2D. Figure 5.4 shows the results for the bubble cloud at different times. The density, ρ, at $t^* = 0.0$ the initial jump across the bubble cloud interface is present. During the collapse of the interface, i.e., the position where the ρ reaches the initial outside state, moves towards the center. The density at the center also remains almost constant during the collapse before the interface reaches the center. Further, the jump between the inner and the outside condition remains very steep, only across a few DOF. At the collapse time $t^* = 1.0$ the density increase is clearly observable.

For the temperature only three different stages are present, before, at and after the collapse. Before the collapse the temperature remains almost unchanged until the collapse. At the moment of collapse the temperature rises by about 2 K. After the shock the temperature in the plotted area has risen slightly compared to the initial state. Overall, the effects in temperature are relatively small; for a collapse with non-condensable gas the thermal effects would be expected to be significant.

Due to the initial states a rarefaction wave travels from the interface in outward direction and results in a rapid decreases in pressure. The interface pressure has dropped

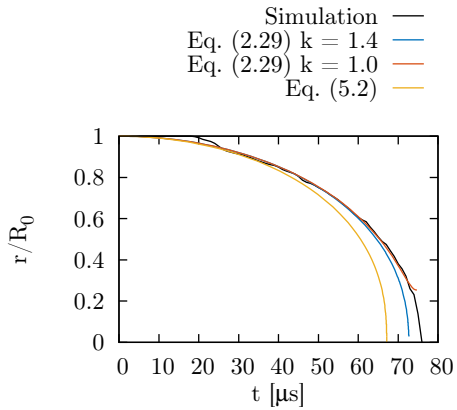

Figure 5.3.: Radius for the 3D collapse of the spherical vapor bubble, for the simulation the HLLC Riemann solver was used and compared to Rayleigh-Plesset equations.

by about an order of magnitude at $t^* = 0.4$. During the collapse a shock front steepens and the pressure rises as a consequence. The pressure information, however, can only travel in outward direction and adjusts to almost the initial pressure at $t^* = 0.9$. At the collapse the pressure increases significantly. The inward impulses are being transformed into pressure at their stagnation point in the collapse center. After the collapse the pressure shock wave travels outwards and results in a generally higher pressure compared to the initial state.

For the velocity positive values denote an outward and negative value an inward directed velocity. The velocity at the interface is always highest and increases during the collapse. At the collapse time the velocity decreases, until the flow reaches the stagnation point. After the shock a small outwards velocity is observed.

The speed of sound has the biggest jump across the interface. The general trend is very similar to the density with the difference that it decreases even a bit further at the interface on the two-phase side. Since the speed of sound is much smaller than the velocity of the phase interface, the states inside and outside of the interface are almost hydraulically decoupled. This is observable for all investigated properties.

In Figure 5.5 the initial state of the bubble is fully in the gaseous state. Compared to the previous simulation, the jump of the density becomes steeper during the collapse after an initial drop. Contrary to the bubble cloud the density at the bubble center increases

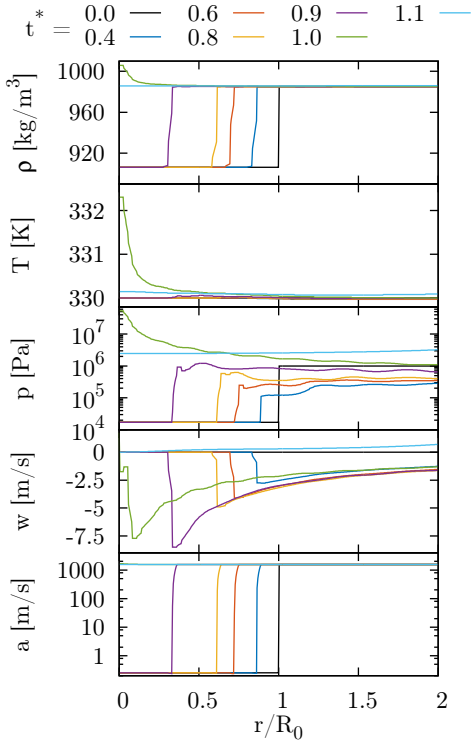

Figure 5.4.: Collapse of the spherical bubble cloud along x-axis for different times.

before the interface reaches the center. The temperature in the center increase before the actual collapse. At the collapse the temperature rises far more than for the bubble cloud and afterwards a thermal wave is observed in the results. The pressure is similar in its general trend, but the center is influenced before the collapse occurs. The velocities towards the center are about an order of magnitude higher. The speed of sound shows that for the initial state both phases are not fully hydraulically decoupled. However, due to the inwards traveling shock wave, the saturation pressure is reached. This leads to a rapid decrease in speed of sound and then a hydraulic decoupling of the inner and outer side of the interface occurs.

With the here assessed collapse of the bubble cloud and vapor bubble, which are essen-

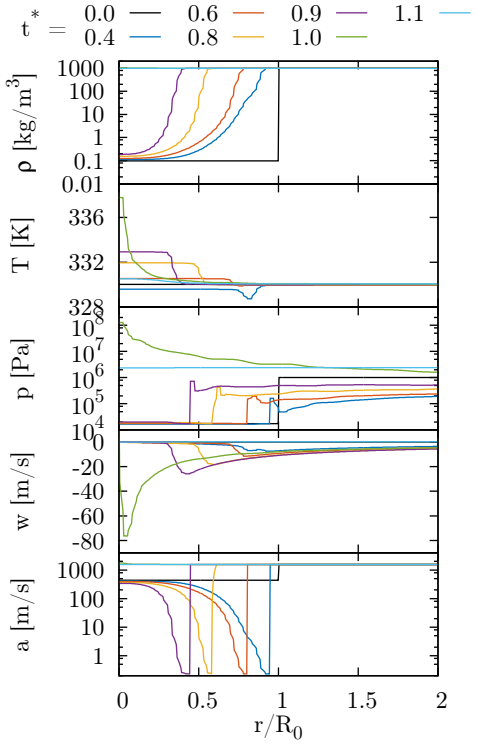

Figure 5.5.: Collapse of the spherical vapor bubble along x-axis for different times.

tially a 2D multi-phase numerical shock experiment, different effects are identified and need to be considered. First, in an experiment of a bubble collapse an initial condition in the two-phase state is very hard to obtain. To the author's knowledge no experiment with a isolated single spherical bubble cloud has ever been performed. Therefore, the bubble cloud state is an artificial numerical experiment for a single bubble collapse. However, within a complex simulation a collapse of a bubble cloud is fairly common and the results help to gain a better understanding of the process. The main finding is here that the inner state of the collapsing bubble is almost fully decoupled from the outside during the collapse.

5.1.3. Grid dependency and pressure variation

For the 3D case a grid independence study is performed. The coarsest mesh has 16 DOF in one axis of the initial bubble cloud. The mesh is then refined by a factor of two for each dimension. The finest mesh has 256 DOF across the initial bubble cloud with 1.510×10^8 DOF in total.

Figure 5.6 shows the maximum pressure p_{max} for different far field pressures $p_\infty = 2\,\text{bar}$, $20\,\text{bar}$, $50\,\text{bar}$ and $100\,\text{bar}$. For the far field pressure $p_\infty = 2\,\text{bar}$ and $20\,\text{bar}$ the grid dependency study is carried out up to 256 DOF across the initial bubble radius and for $p_\infty = 50\,\text{bar}$ and $100\,\text{bar}$ up to 128 DOF. For the latter, the maximum pressure would have exceeded the fluid data and extrapolation with an uncertain error would have been needed. Therefore, only the extrapolated p_{max} is shown without a simulation point. The mass fraction is $x = 1 \times 10^{-6}$. The simulation results for the maximum pressure for all far field pressures suggest a linear correlation with DOF per axis. A higher far field pressure results in a higher maximum pressure compared to the same resolution. The here preformed mesh resolution study shows that no grid independent can be achieved. Schmidt et al. [105] found that for a vapor bubble cloud the maximum pressure correlates linearly with the DOF per axis, which coincides with the present findings.

The resolutions for a single bubble collapse are very high and therefore are out of scope for more complex simulations, e.g., micro channel flow in Section 5.2. For a specific numerical scheme a correlation could be developed to normalize the maximum pressure to compare different designs. This way different designs could be compared qualitatively even on different meshes, i.e., resolution of the smallest cell for a collapse.

5.1.4. Bubble collapse in the proximity of a wall

The impact of a cavitation collapse of a single bubble has been studied for many years, theoretically, experimentally and numerically. As discussed in Section 3.6.3 the applied numerical scheme introduces a number of limitations. Therefore, it is important to verify the results with experiments or analytical solutions. For a collapse close to a wall, the analytical results of Plesset and Chapman [96] and the experimental results of Lauterborn and Bolle [72] are used.

A schematic of the results obtained by Plesset and Chapman [96], which are in great agreement with experiments is shown in Figure 5.7. This schematic is used to verify the general behavior of the bubble collapse close to a wall. It has to be noted, that for the simulation setup the bubble is moved closer to the wall than in the schematic. The key features of the bubble dynamics, which are of interest are the movement towards the wall, the narrowing of the bubble sides, the flattening of the bubble top and the generation of a jet.

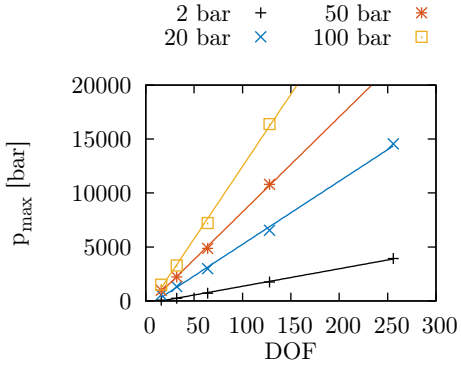

Figure 5.6.: Mesh resolution study with different far field pressures with a line of best fit. The results for $p_\infty = 50\,\mathrm{bar}$ and $100\,\mathrm{bar}$ are extrapolated from the best fit and not simulated for 256 DOF.

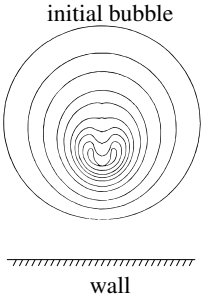

Figure 5.7.: Schematic of a bubble collapse close to a wall, cf. [96].

Grid convergence

For a bubble collapse without wall effects no independence of the grid resolution for the used method is present, i.e., the pressure increases with finer resolutions. A collapse of a bubble close to a wall is now investigated on different grids. Here, a far field pressure of $10\,\mathrm{bar}$ is used. The other initial conditions are the same as for the grid convergence without a wall, cf. Section 5.1.3. The initial bubble position is at a distance slightly more

than one radius to align the initial bubble center with a grid element center.

In Figure 5.8 the maximum collapse pressure for four different grid resolutions are shown. Similar to before, $p_{\max}$ increases significantly with an increase of DOF per bubble. Compared to the collapse without a wall the slope might decrease with larger DOF. The general trend remains and grid independence of the maximum pressure is not found.

To asses the possible damage of a component the corresponding pressure shock wave at the wall tends to be a measure to predict the damage potential. Therefore, the results for the maximum wall pressures are presented in Figure 5.9. Similar to the maximum collapse pressure the maximum wall pressure increases at first with an increase in resolution. However, the two finest grid show almost identical pressures. These findings agree with data from the literature [105] and therefore simulations on even finer grids are not carried out. Nonetheless, in simulations of components collapses of cavitation are commonly simulated with less local resolutions compared to the current simulation. Consequently, a grid independence is unfeasible for most cases within such simulations.

Pressure evolution during collapses

Figure 5.10 shows the wall pressure at the center of the bubble during the collapse. The most coarse grid shows a relatively flat plateau of the peak pressure. The grid with 32

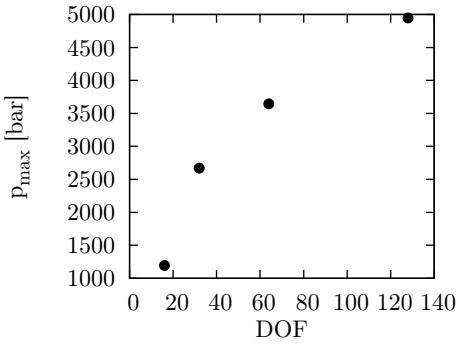

Figure 5.8.: Maximum pressure over the DOF across the initial bubble in each spatial direction for different grid refinements at $T = 330\,\mathrm{K}$ and $p = 10\,\mathrm{bar}$, cf. [81].

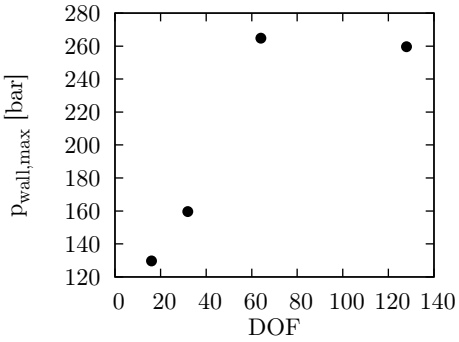

Figure 5.9.: Maximum wall pressure over the DOF across the initial bubble in each spatial direction for different grid refinements at $T = 330\,\mathrm{K}$ and $p = 10\,\mathrm{bar}$, cf. [81].

DOF already shows a sharp peak and a second smaller collapse afterwards. The time of the maximum peak is later than for the coarser grid. The two finest grids almost align around the peak and are only slightly later than for the 32 DOF grid. The peak values increase and the peak shape is even sharper. The only distinct difference for the two finest grids is the second smaller peak. In the simulation on the finest grid it occurs slightly earlier and is stronger than for the other one. Nonetheless, even for the pressure evolution at the wall the results almost converge for the two finest resolutions.

Mass fraction variation for collapses close to a wall

As aforementioned, in a simulation with the HEM the collapse of cavities can occur at different vapor states. It can range from only very low vapor mass fractions up to fully gaseous bubbles at very low pressures. The different initial states are summarized for the Vapor Fraction Study (VFS) in Table 5.2. Note that vapor mass fraction is used as variation value, however, the vapor volume fraction is also used for comparison. Therefore, in the notation those two fractions are not distinguished. This case study is performed in 2D and the initial bubble is discretized with 72 DOF for each axis. For the 2D case only one element is used in z-axis and the impulses are set to $0\,\mathrm{kg\,m\,s^{-1}}$. The resolution is chosen based on the results on a grid study for the 2D case. With this mesh all relevant effects are present and grid refinement only let to an increase in maximum pressure.

First, bubble shapes for the different cases are compared to Figure 5.7. The results

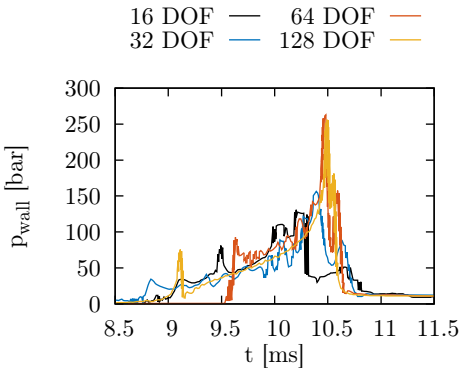

Figure 5.10.: Wall pressure over time for different grid refinements at $T = 330\,\mathrm{K}$ and $p = 10\,\mathrm{bar}$, cf. [81].

Table 5.2.: Initial states for vapor fraction parameter study in 2D.

	ρ [kg m^{-3}]	T [K]	p [Pa]	x	α
far field	985.2	330.0	1×10^6		
VFS 1	906.2	330.0	1.721×10^4	1×10^{-5}	0.07979
VFS 2	527.5	330.0	1.721×10^4	1×10^{-4}	0.4644
VFS 3	101.8	330.0	1.721×10^4	1×10^{-3}	0.8967
VFS 4	11.23	330.0	1.721×10^4	1×10^{-2}	0.9887
VFS 5	1.135	330.0	1.721×10^4	1×10^{-1}	0.9990
VFS 6	0.1136	330.0	1.721×10^4	1	1.000
VFS 7	0.09891	330.0	1.500×10^4		
VFS 8	0.06584	330.0	1.000×10^4		

are shown in Figure 5.11. Note that for the different cases different times for the density snapshot are chosen. Due to the different inertia forces the collapse times vary strongly between the cases. Therefore, the bubble shape is illustrated shortly before the collapse, whilst the shape is still adequately represented on the chosen mesh. The initial bubble shape is represented by the dashed lines and the thick gray line at the bottom represents the wall. The density ranges from the initial state inside the bubble to the density in the

far field and is colored from black to white, respectively.

In Figure 5.11a the bubble becomes very narrow. The top is flatter than the bottom, however, an inward curvature at the top is not present. The collapse duration is shorter than for higher x. For this state the initial speed of sound a is the lowest of all initial cases. From Figures 5.11b to 5.11d the collapse duration increased and the top flattened until an inward curvature is created. In Figure 5.11d a jet formation similar to Figure 5.7 is observed. For the cases VFS 5 to VFS 7 in Figures 5.11d to 5.11g, respectively, the inward curvature becomes more dominant. Additionally, the bubble seems to split. This is a non-physical effect which does not occur in experiments. As shown later, this is due to the LF Riemann solver and is not present with the HLLC Riemann solver. In Figure 5.11h no bubble separation is observed. However, the inward curvature is less than for the former cases. For this vapor fraction study the bubbles move more downwards with increasing x or a reduction in bubble pressure.

Further, the position and the intensity of the final collapse is analyzed. Figure 5.12 illustrates the position and the value of the maximum pressure for different initial conditions. Table 5.3 summarizes these results. The simulation results suggest that with increasing proportion of the vapor in the mixture region the maximum pressure increases and the collapse moves closer to the wall. However, for an initial condition of the bubble outside of the wet steam region and fully in the gaseous regime the maximum pressure decreases. The collapse continues to move towards the wall with the decreased density of the initial condition. Generally, the results indicate that the collapse pressure and movement of the bubble strongly correlate with the vapor volume fraction.

Table 5.3.: Result summary for vapor fraction parameter study in 2D.

	α	p_{max} [bar]	t_{col} [s]	h [m]
VF 1	0.07979	0.4423×10^3	$\approx 2.2 \times 10^{-5}$	3.955×10^{-4}
VF 2	0.4644	1.195×10^3	$\approx 6.0 \times 10^{-5}$	3.820×10^{-4}
VF 3	0.8967	1.456×10^3	$\approx 8.8 \times 10^{-5}$	2.845×10^{-4}
VF 4	0.9887	1.455×10^3	$\approx 9.3 \times 10^{-5}$	2.570×10^{-4}
VF 5	0.9990	1.463×10^3	$\approx 9.4 \times 10^{-5}$	2.570×10^{-4}
VF 6	1.000	1.486×10^3	$\approx 9.4 \times 10^{-5}$	2.570×10^{-4}
VF 7		1.399×10^3	$\approx 9.4 \times 10^{-5}$	2.155×10^{-4}
VF 8		1.443×10^3	$\approx 9.4 \times 10^{-5}$	2.155×10^{-4}

Figure 5.13 compares the collapse with the LF and the HLLC Riemann solver for the VFS7. The simulation results for the LF Riemann solver indicate a separation of the bubble. As discussed prior, this effect has not been published in the literature and

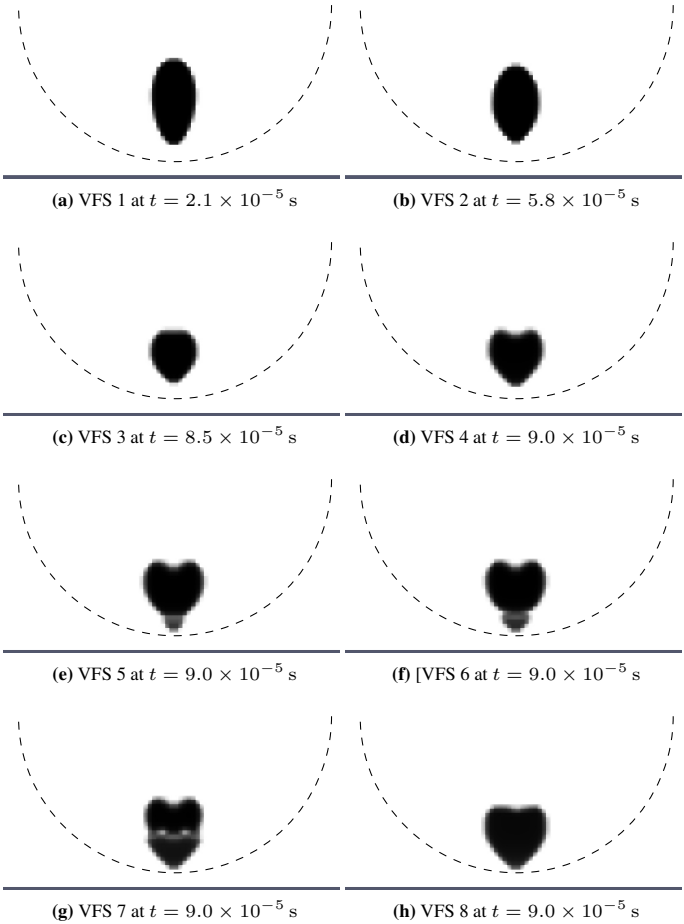

(a) VFS 1 at $t = 2.1 \times 10^{-5}$ s **(b)** VFS 2 at $t = 5.8 \times 10^{-5}$ s

(c) VFS 3 at $t = 8.5 \times 10^{-5}$ s **(d)** VFS 4 at $t = 9.0 \times 10^{-5}$ s

(e) VFS 5 at $t = 9.0 \times 10^{-5}$ s **(f)** [VFS 6 at $t = 9.0 \times 10^{-5}$ s

(g) VFS 7 at $t = 9.0 \times 10^{-5}$ s **(h)** VFS 8 at $t = 9.0 \times 10^{-5}$ s

Figure 5.11.: Cavitation bubble deformation for different initial states shortly before the final collapse; the initial bubble location is indicated by the dashed line and the wall as solid line on the bottom.

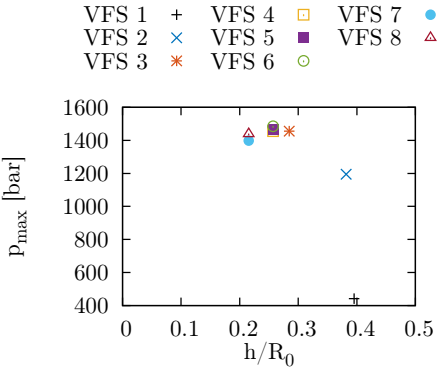

Figure 5.12.: Maximum pressure and collapse distance from the wall for the vapor fraction study in 2D.

therefore the representation of the collapse with the LF is inadequate. Nonetheless, an inward movement of the top of the bubble is observed. On the other hand, the HLLC does not show a bubble separation. The interface is smoother than for the LF and a stronger inward movement is present. The simulation results are similar to [2] which used a sharp interface technique. The bubble shape in the present work is slightly wider than for Plesset and Chapman [96]. The experimental results from Vogel et al. [127] suggested a wider bubble shape than from Plesset and Chapman [96]. Therefore, the results with the HLLC Riemann solver are within the range of the results of the former.

Influence of wall distance on collapse behavior

In Figure 5.14 the maximum collapse pressure for distances wall differences is shown. For $H/R_0 = 0.7$ the bubble is partly "inside" the wall, hence the initial volume is smaller. This and the strong wall interaction cause the lowest collapse pressure. Moving the initial bubble away from the wall the maximum pressure increases and reaches a peak at $H/R_0 = 1.5$. Further away from the wall the peak pressure decreases and a minimal value for the peak is reached at about $H/R_0 = 2.2$. After this point the pressure increases again.Brujan and Matsumoto [24] found that the shock wave pressure with a fixed distance to their focus experiences a minimum value for a finite distance of the initial bubble. In the present work, such a minimal value is present, however, the initial wall distance is different. This might be due to the initial condition of the

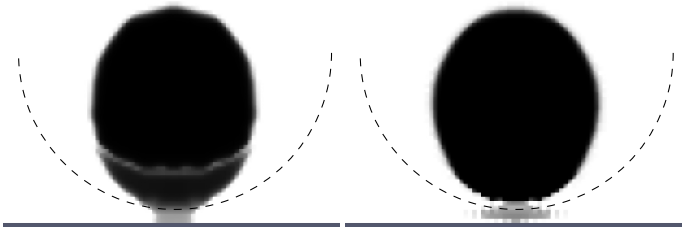

(a) LF at $t = 7.0 \times 10^{-5}$ s **(b)** HLLC at $t = 7.0 \times 10^{-5}$ s

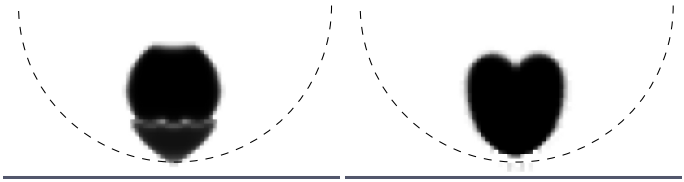

(c) LF at $t = 8.5 \times 10^{-5}$ s **(d)** HLLC at $t = 8.5 \times 10^{-5}$ s

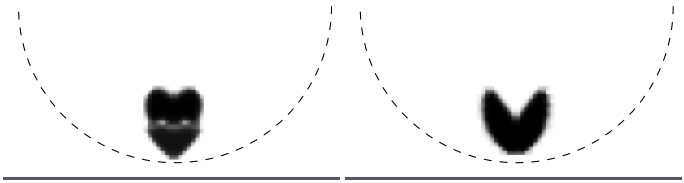

(e) LF at $t = 9.0 \times 10^{-5}$ s **(f)** HLLC at $t = 9.0 \times 10^{-5}$ s

Figure 5.13.: Comparison of LF and HLLC Riemann solver for a bubble collapse close to a wall. The initial bubble interface is dashed.

simulation, e.g., starting the simulation with the maximum bubble radius and the initial state causing a rarefaction wave.

Figure 5.15 shows the maximum wall pressure in the simulation for different initial wall distances at a far field pressure of $1\,\mathrm{bar}$ for the 3D case. In this simulation the FV elements are triggered with the Persson sensor. Therefore, the pressure waves are transported with the higher-order scheme. For a wall distance of $H/R_0 = 0.7$ the collapse occurs directly at the wall. Hence, the corresponding pressure is highest. With increasing distance the pressure signal at the wall is reduced. It has to be noted that the initial state corresponds to VFS1 and therefore, no impinging jet could form for the smaller wall distances.

Further, the collapse time is strongly influenced by wall distance. Figure 5.16 shows the collapse time for different wall distances. For the initial bubble position $H/R_0 = 0.7$ the collapse occurs in the simulation at $t = 10.6 \times 10^{-6}\,\mathrm{s}$. With increasing wall distance the collapse time decreases and approaches the duration time without a wall $t = 8.5 \times 10^{-6}\,\mathrm{s}$. The longer collapse time close to the wall is due to inwards flowing fluid. The wall reduces volume from which fluid can flow into the "gap", i.e., the volume of the bubble, and therefore the inertia of the system is higher.

Influence of fluid pressure on the maximum pressure

Figure 5.17 shows the maximum pressure at the wall for different far field pressures. The initial wall distance is set to $H/R_0 = 1$. Similar to the maximum pressure without

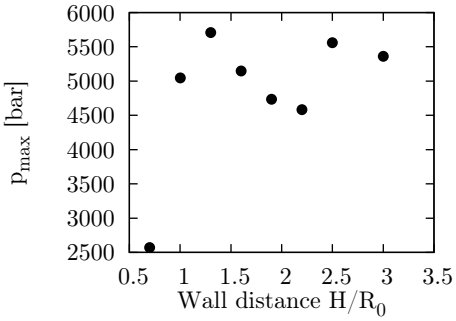

Figure 5.14.: Maximum pressure in the simulation for different initial wall distances at a far field pressure of $10\,\mathrm{bar}$ for the 3D case, cf. [81].

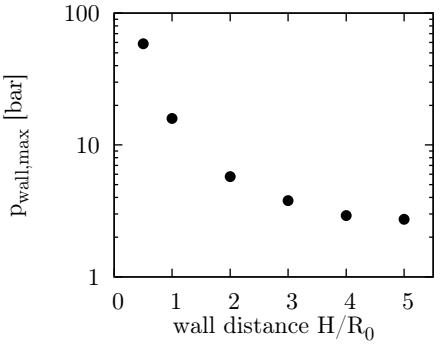

Figure 5.15.: Maximum wall pressure in the simulation for different initial wall distances at a far field pressure of 10 bar for the 3D case, cf. [81].

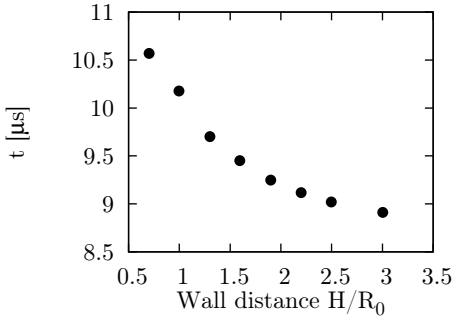

Figure 5.16.: Collapse duration for different initial wall distances at a far field pressure of 10 bar for the 3D case, cf. [81].

a wall (cf. Figure 5.6), the maximum pressure at the wall strongly correlates with the far field pressure. With the increasing pressure outside of the wall, the driving forces of the collapse increase and with it the corresponding impulses of the collapse.

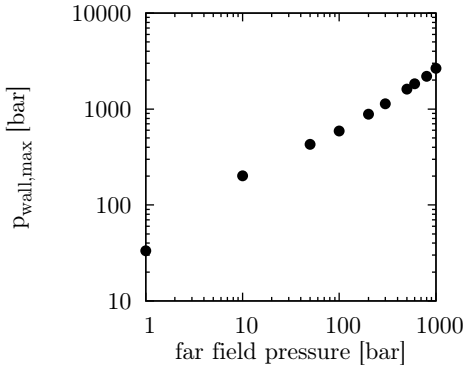

Figure 5.17.: Maximum wall pressure for different far field pressures at a wall distance of $H/R_0 = 1$ for the 3D case, cf. [81].

Influence of cross flow velocity on the bubble collapse

Whilst the previous simulations allow for further insights into the behavior of the applied simulation scheme and bubble dynamics, in a component the fluid is rarely motionless. Therefore, the influence of a cross flow is investigated. The 2D setup for a spherical vapor bubble, cf. VFS 7 in Table 5.2, close to a wall is used. The initial bubble position is moved on the x-axis two bubble radii upstream of the cross flow. The cross flow velocity is varied to $w_0 = 0\,\mathrm{m\,s^{-1}}$, $1\,\mathrm{m\,s^{-1}}$ and $10\,\mathrm{m\,s^{-1}}$.

In Figure 5.18 the maximum pressures during the simulation at each mesh element for the different cross flow velocities are presented. For the case with $0\,\mathrm{m\,s^{-1}}$ a maximum pressure of $1261\,\mathrm{bar}$ is achieved in the simulation, see Figure 5.18a. Due to the aforementioned movement of the initial bubble position an asymmetric collapse in the very late stages occurs. This asymmetry results in an asymmetric maximum pressure distribution. For a symmetric case a lower maximum pressure would be expected. Nonetheless, two separate collapse regions were identified in the simulation.

By introducing only a slight cross flow velocity of $w_0 = 1\,\mathrm{m\,s^{-1}}$ the collapse behavior changes completely in the simulation (see Figure 5.18b). Hence, the symmetry is broken and only a single collapse location is identified. Further, the maximum pressure increases significantly to $2162\,\mathrm{bar}$. This suggests, that only a slight disturbance due to a cross flow velocity influences the collapse significantly and the potential loads on a surface.

By increasing the cross flow velocity even further to $w_0 = 10\,\mathrm{m\,s^{-1}}$ the maximum pressure distribution changes as presented in Figure 5.18c. The location of the high

pressure region moves further downstream of the cross flow due to the increased cross flow velocity. The simulation results suggest, that two locations with high pressure are present and the maximum pressure increases to $5512\,\mathrm{bar}$.

In Figure 5.19 the density is presented for the cross flow velocity of $w_0 = 1\,\mathrm{m\,s^{-1}}$. A difference compared to $w_0 = 0\,\mathrm{m\,s^{-1}}$ is the collapse time. With a cross flow the collapse occurs faster in the simulation. Further, the shape changes drastically. At $t = 67 \times 10^{-6}\,\mathrm{s}$ in Figure 5.19a the top of the bubble seems to move slower than the cross flow and the top right side moves inwards. In Figure 5.19b an even stronger inward movement is observable. The collapse introduces a spin on the bubble, which becomes more clear in Figure 5.19c. Here, a tail of the bubble forms. The dynamics of the bubble collapse are very fast at that time and the tail becomes thinner until the resolution of the simulation is not able to represent it. At $t = 80 \times 10^{-6}\,\mathrm{s}$ in Figure 5.19d the tail vanishes and the shape resembles a half circle. The spin of the collapse results in a narrow ellipsoid shape shortly before the collapse as presented in Figure 5.19e. Hence, the whole process of the collapse is very dynamic and a representation of these dynamics might be very challenging for other simulations, e.g., micro channel flow.

The effects described prior for the cross flow velocity of $w_0 = 1\,\mathrm{m\,s^{-1}}$are more dominant with a velocity of $w_0 = 10\,\mathrm{m\,s^{-1}}$. Figure 5.20 shows the density during the collapse. The tail of the bubble is stronger than for the slower cross flow. The spin of the bubble is also stronger and leads to a kidney shaped bubble shortly before the collapse. The collapse duration is shortest and the corresponding shock wave is strongest. Therefore, the results indicate that with an increasing cross flow velocity the damage potential of cavitation might increase.

Figure 5.21 shows the wall normal velocity shortly after the collapse for the different cross flow velocities. For $w_0 = 0\,\mathrm{m\,s^{-1}}$ the classical impinging jet is present. The cross flow introduces a spin, which increases the maximum velocity towards the wall. With $w = 10\,\mathrm{m\,s^{-1}}$ the collapse center moves notably downstream and spinning movement becomes very strong. Due to the spinning the velocity field varies from the classical impinging jet.

Voß investigated bubble collapses inside a cross flow numerically and experimentally [128]. A quantitative comparison shows a tilt of the bubble and variation from the classical jet directly towards the wall. This is similar to the findings of the present work. However, for the experiment the bubble growth is also in the cross flow and the bubble deformed before the maximum radius R_0. Therefore, a quantitative comparison is not possible.

Multiple bubbles

In the following, the collapse of multiple bubbles is assessed. Here, two bubbles of the same size and the same distance to the wall are investigated. Figure 5.22 shows a schematic of the initial state of the simulation. The distance to the wall is $H/R_0 = 2$ and

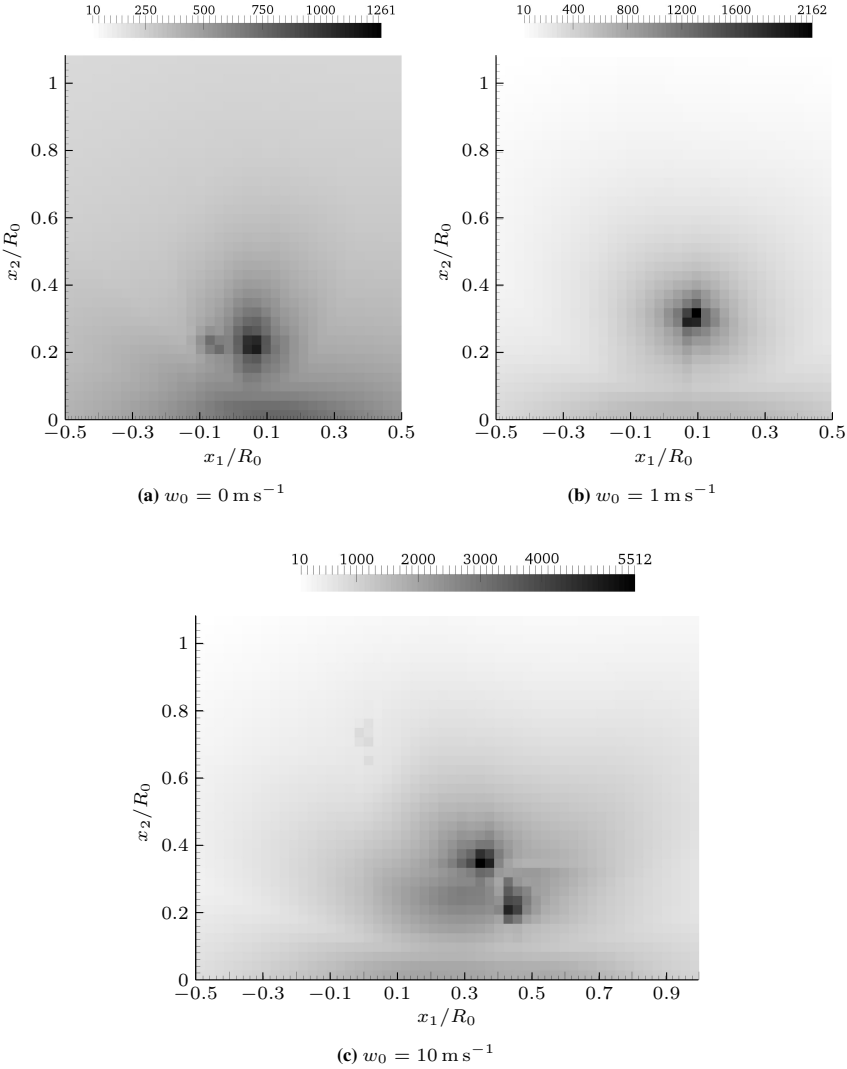

(a) $w_0 = 0\,\mathrm{m\,s^{-1}}$

(b) $w_0 = 1\,\mathrm{m\,s^{-1}}$

(c) $w_0 = 10\,\mathrm{m\,s^{-1}}$

Figure 5.18.: The maximum pressure in bar for each DOF for bubble collapses with a cross flow.

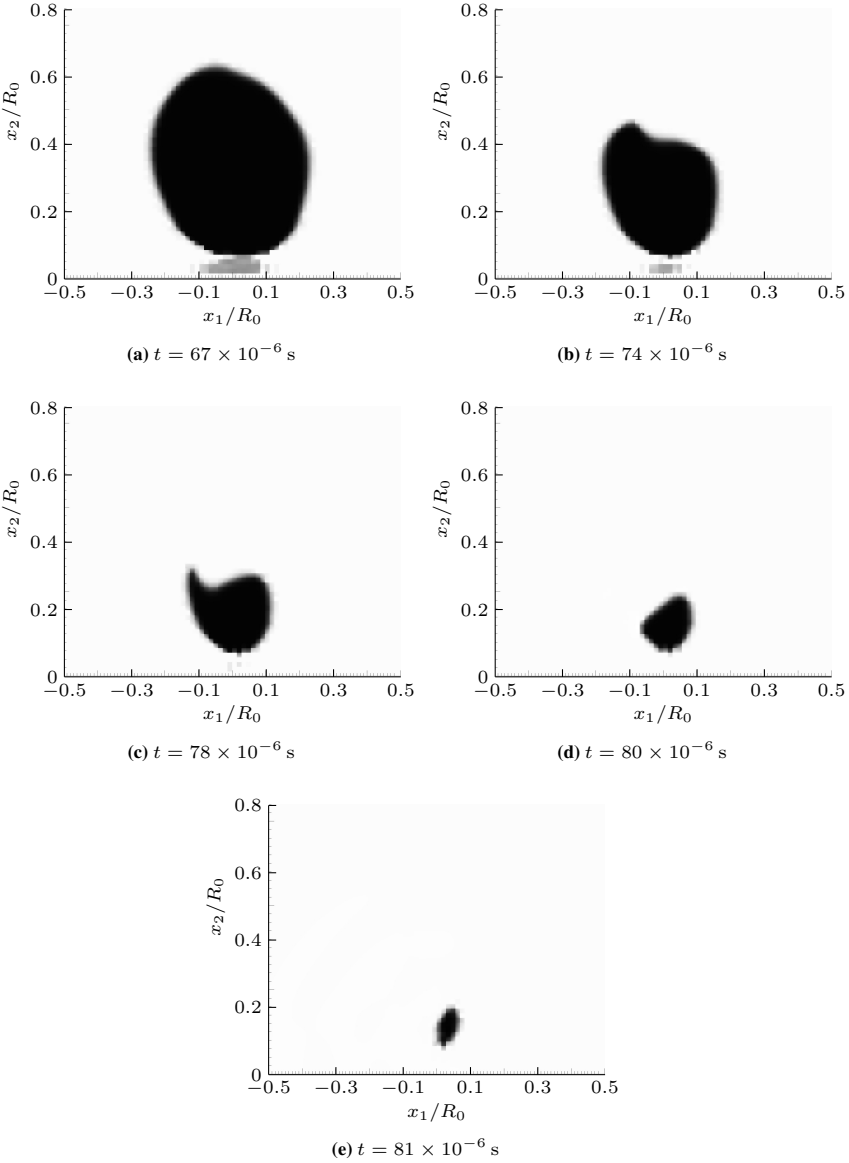

(a) $t = 67 \times 10^{-6}\,\mathrm{s}$

(b) $t = 74 \times 10^{-6}\,\mathrm{s}$

(c) $t = 78 \times 10^{-6}\,\mathrm{s}$

(d) $t = 80 \times 10^{-6}\,\mathrm{s}$

(e) $t = 81 \times 10^{-6}\,\mathrm{s}$

Figure 5.19.: Density for a cross flow velocity of $1\,\mathrm{m\,s^{-1}}$.

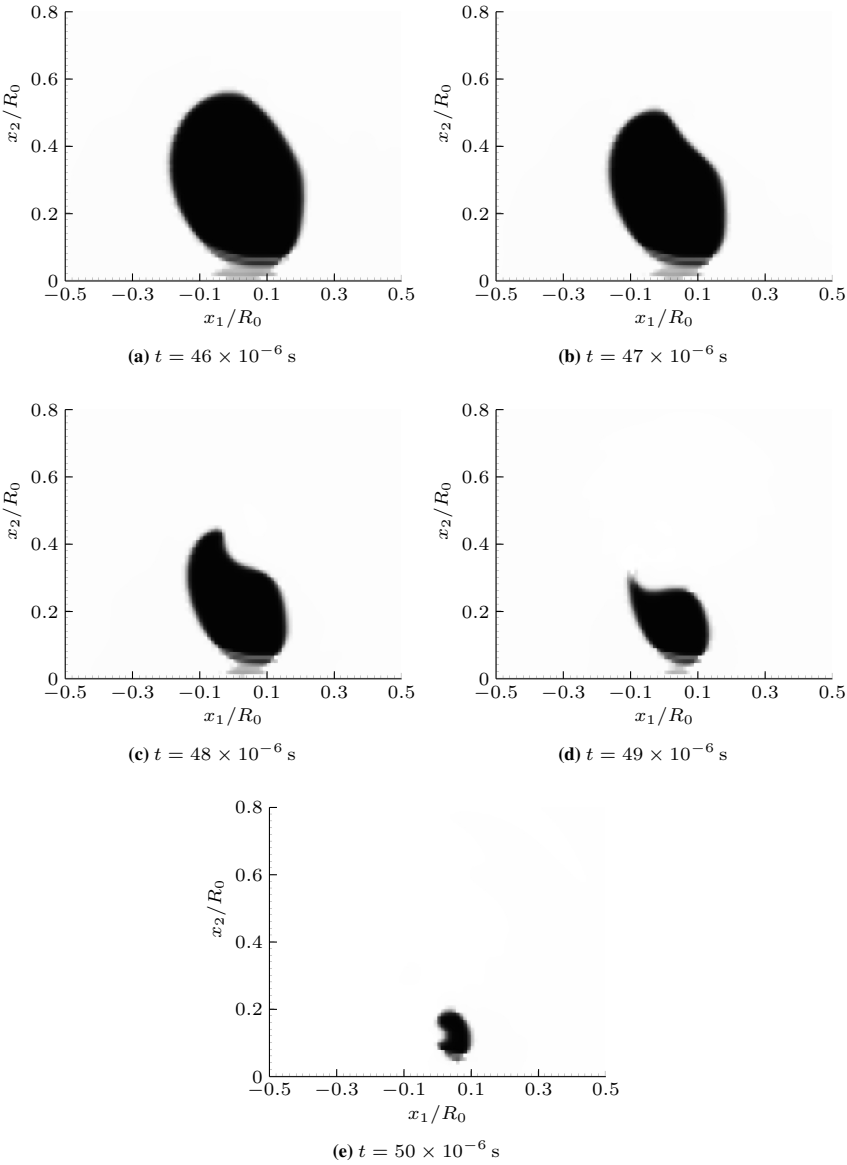

(a) $t = 46 \times 10^{-6}\,\mathrm{s}$

(b) $t = 47 \times 10^{-6}\,\mathrm{s}$

(c) $t = 48 \times 10^{-6}\,\mathrm{s}$

(d) $t = 49 \times 10^{-6}\,\mathrm{s}$

(e) $t = 50 \times 10^{-6}\,\mathrm{s}$

Figure 5.20.: Density for a cross flow velocity of $10\,\mathrm{m\,s^{-1}}$.

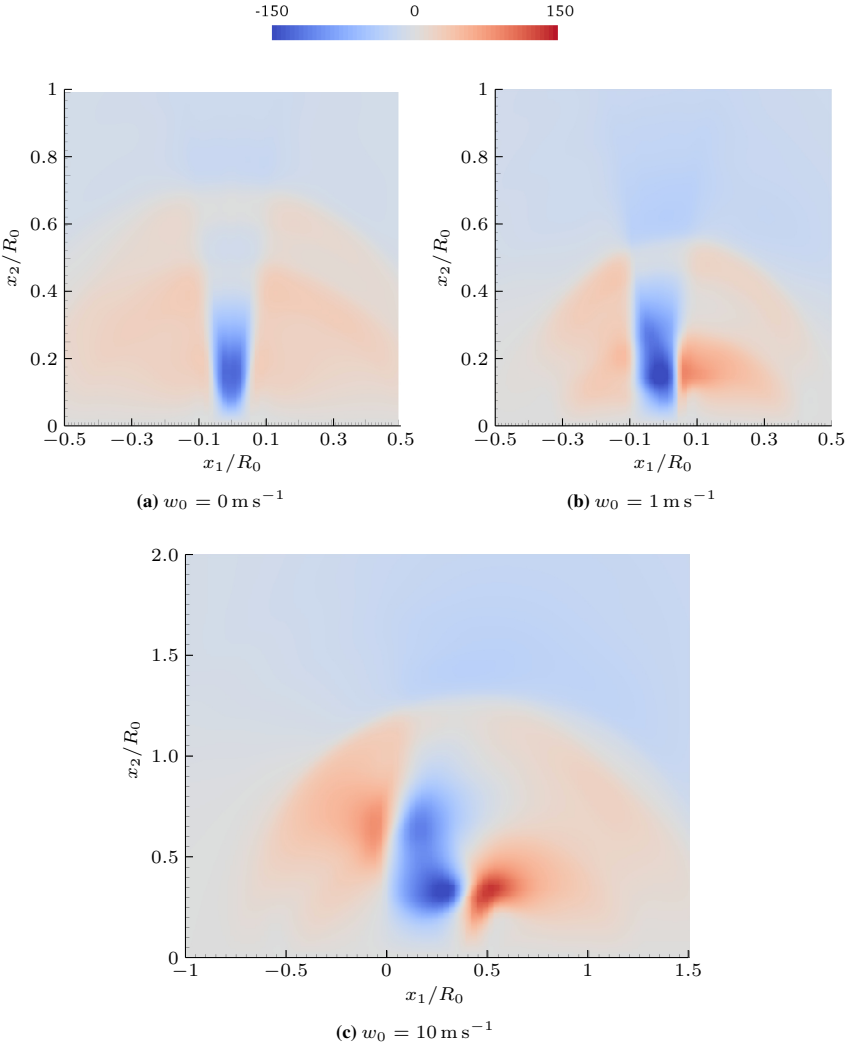

(a) $w_0 = 0\,\mathrm{m\,s^{-1}}$

(b) $w_0 = 1\,\mathrm{m\,s^{-1}}$

(c) $w_0 = 10\,\mathrm{m\,s^{-1}}$

Figure 5.21.: Velocity vertical to the wall, w_2 $[\mathrm{m\,s^{-1}}]$, for different cross flow velocities.

the initial bubble radius $R_0 = 1 \times 10^{-3}\,\mathrm{m}$. The distance of the two bubbles is denoted with D and varies from $D/R_0 = 1$ to $D/R_0 = 5$ in the following.

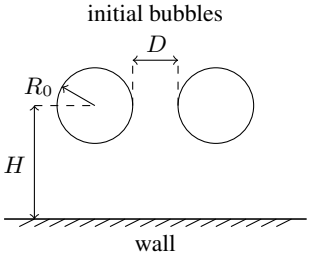

Figure 5.22.: Schematic of a initialization of the simulation with two vapor bubbles.

Figure 5.23 shows the maximum wall pressure, which occurs for two vapor cloud bubbles for different distances between them. The pressure ranges from $2.6 \times 10^6\,\mathrm{Pa}$ to $3.04 \times 10^6\,\mathrm{Pa}$ for the different distances. Therefore, the influence on the maximum wall pressure is rather small. The bubble influence each other strongly at closer distances, e.g., deformation or horizontal movement. However, this has only little influence to the wall pressure. Therefore, the simulation results suggest, that the interaction of the bubbles of this isolated case has therefore negligible influence for a potential surface damage.

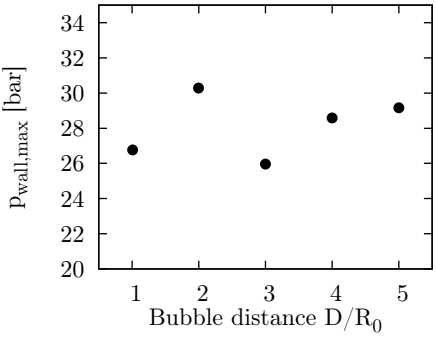

Figure 5.23.: Maximum wall pressure with two vapor bubbles for different distances between them and a fixed distance to the wall $H = 2$, cf. [81].

5.2. Micro channel

The micro channel flow is a widely used test case to validate simulation results with cavitation involved [108]. For the flow through the micro channel experiences many different temporal and spatial scales. For example, the pressure wave velocity, i.e, local speed of sound, within a two phase region is very slow, i.e., less than $1\,\mathrm{m\,s^{-1}}$, and reaches values up to $1400\,\mathrm{m\,s^{-1}}$ in the liquid phase. Further, the turbulent vortexes generated at the channel exit are orders of magnitudes larger than in bubble collapses. From this complexity arise many challenges, one is the representation of EOS.

5.2.1. Numerical setup

For the simulation of the micro channel with water a computation domain with an inlet and an outlet with sufficient distance to the narrowing is used, see Figure 5.24. The narrowing has a height of $0.3 \times 10^{-3}\,\mathrm{m}$, a depth of $0.3 \times 10^{-3}\,\mathrm{m}$ and a length of $1 \times 10^{-3}\,\mathrm{m}$. At the outlet a damping sponge is used to avoid non-physical reflections. All walls are defined with slip.

For the simulation two different grids are used (Figure 5.25). Both grids have the same baseline grid and are refined in the narrowing of the micro channel. The coarse grid is refined by one in the area around and in the narrowing and by a factor of two at the upper and lower walls of the narrowing. The refined area of the coarse grid is shown in Figure 5.25a. The coarse grid has 1.070×10^5 elements and with the applied order

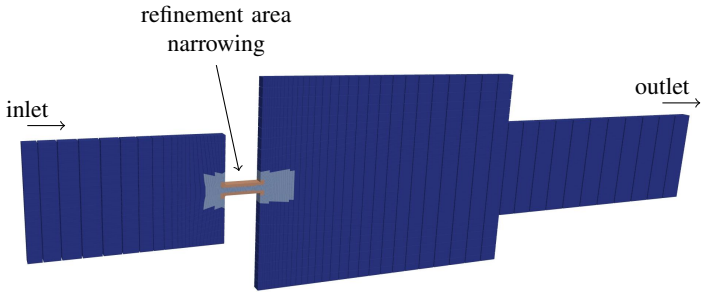

Figure 5.24.: Computational domain of the micro channel, color scales denote the refinement levels for the medium grid.

6.845×10^6 DOF. The fine grid is further refined as is shown in Figure 5.25b. It has 6.304×10^5 elements and with the applied order 7.881×10^7 DOF. A spatial order of 4 for the coarse grid and 5 for the fine grid is used. For this grid the leading and trailing edge of the narrowing are shown in Figure 5.25c. The complete area close to the wall is refined so that the cavitational areas are well resolved in the simulation. Due to curvature of the leading edge and the importance of this area the mesh quality in this area is very important for the simulation. As illustrated in Figure 5.25c the quality of the mesh is very good.

The inlet conditions are $p_{\text{in}} = 3 \times 10^7\,\text{Pa}$ and $T_{\text{in}} = 330\,\text{K}$ and the outlet conditions are $p_{\text{out}} = 1 \times 10^7\,\text{Pa}$ and $T_{\text{out}} = 330\,\text{K}$. The computational domain is initialized with the outlet conditions. This leads to a non-chocked operating point with moderate cavitation.

Stabilization with equation of state evaluation

So far either a fully turbulent flow (Section 4.2) or rapid phase transitions (Section 5.1) have been discussed in the present work. In the micro channel both challenges occur at the same time. As a consequence the simulation with the introduced setup is more unstable and leads to unphysical states, e.g., negative density. These instabilities occur even within the TVD FV sub-cell scheme. Therefore, additional stabilization is necessary to allow for the simulation of the micro channel flow.

In the current work, density and temperature are limited. These two thermodynamic variables are also the basis of the used Helmholtz free energy formulation, hence the limitation is consistent for the equations of state and hysteresis for the EOS calculation in reduced. It has to be noted, that due to the limitation of density the conservation of

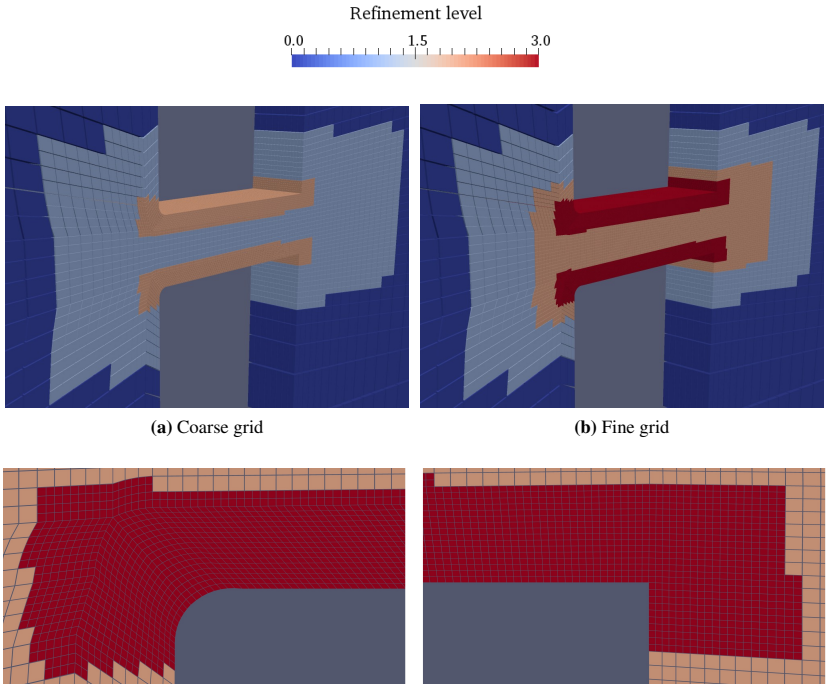

(a) Coarse grid

(b) Fine grid

(c) Boundary layer resolution for the fine grid at the leading and the trailing edge

Figure 5.25.: Different simulation grids for the micro channel flow and detailed illustration of the boundary resolution of the fine grid (not the same scale).

mass is violated. However, the limitation values are set in a way that it is only activated sparsely and the violation is kept to a minimum. Density and temperature are evaluated prior to each access of the table, additionally the density is checked at the beginning of each time step. If the values exceed limiting values, they are set to these limiting values, i.e., isochoric or isotherm process. A $T - \rho$ diagram helps to illustrate the changes in pressure, see Figure B.2. In the current simulation, these values are set to $\rho_{\text{min}} = 1 \times 10^{-3}\,\text{kg}\,\text{m}^{-3}$, $\rho_{\text{max}} = 1300\,\text{kg}\,\text{m}^{-3}$, $T_{\text{min}} = 290.0\,\text{K}$ and $T_{\text{max}} = 1000\,\text{K}$. To ensure that this limitation only changes the results as little as possible, the minimum and maximum values for a number of simulation results in the complete computation domain are checked. The maximum and minimal values are always lower and higher with a

certain margin than the limitation values, respectively. This indicates that this limitation is mostly a stabilization mechanism and only sparsely manipulates the computational results.

5.2.2. Numerical results

In the following, the simulation results for two different Riemann solvers, i.e., LF and HLLC, are compared with each other and their difference to the experimental results of Mauger et al. [77] are discussed. The focus is here on the vapor structures resolved in the simulation and the experiment. Figure 5.26 shows the density at different time intervals. Focusing first on the flow with the LF Riemann solver, the vapor region remains attached during the entire simulation. Within the vapor region shocks travel upstream. This upstream movement is very slow, i.e., approximately $2\,\mathrm{m\,s^{-1}}$, compared to the liquid flow velocity. The liquid velocity ranges approximately from $200\,\mathrm{m\,s^{-1}}$ to $300\,\mathrm{m\,s^{-1}}$. Such shock waves are illustrated in Figures 5.26a, 5.26c and 5.26e. The general dynamic is observed as following: the vapor region travels downstream with a constant thickness, after a certain point either shock waves move upstream or the complete vapor region shrinks upstream. This pumping effect is also observed in the literature for cavitational flows [76]. This process repeats itself, whilst the upper and lower side have similar but independent dynamic. Beyond the trailing edge cavitation areas are only sparsely.

For the simulation with the HLLC Riemann solver this effect is also observed, however, due to additional instabilities the upwards traveling shock waves are disturbed. Consequently, it cannot be illustrated as clearly as for the LF Riemann simulation. More structures are present for the less dissipative Riemann solver and the vapor region width is no longer constant. Larger structures detach from the wall and lead to very strong collapses. The corresponding shock waves then travel upstream and disturb vapor areas. This process is approximately an order of magnitude faster than the upwards traveling shock waves within the vapor region. Hence, this is the dominating effect, which can be observed from simulation results. Beyond the trailing edge far more vapor regions are present than for the LF case. In the experiment of Mauger et al. [77] the vapor region is also very dynamic and detaches from the wall. The general effects are captured by the present simulation with the HLLC.

These results confirm the findings from the single bubble collapse, that the results with the HLLC solver resemble experimental observations better. Therefore, for the finest applied mesh the HLLC Riemann solver is applied. Due to the higher resolution most turbulent scales can be represented by the DG scheme within the channel. Consequently, the FV scheme is used only sparsely for the stabilization of under-resolved scales and is mostly used in cavitation areas.

Figure 5.27 illustrates the shock capturing for the micro channel flow at high resolution. Figure 5.27a shows the density within the channel. In Figure 5.27b the zoomed in view of the lower inlet edge is presented. Small and complex shaped cavitation zones

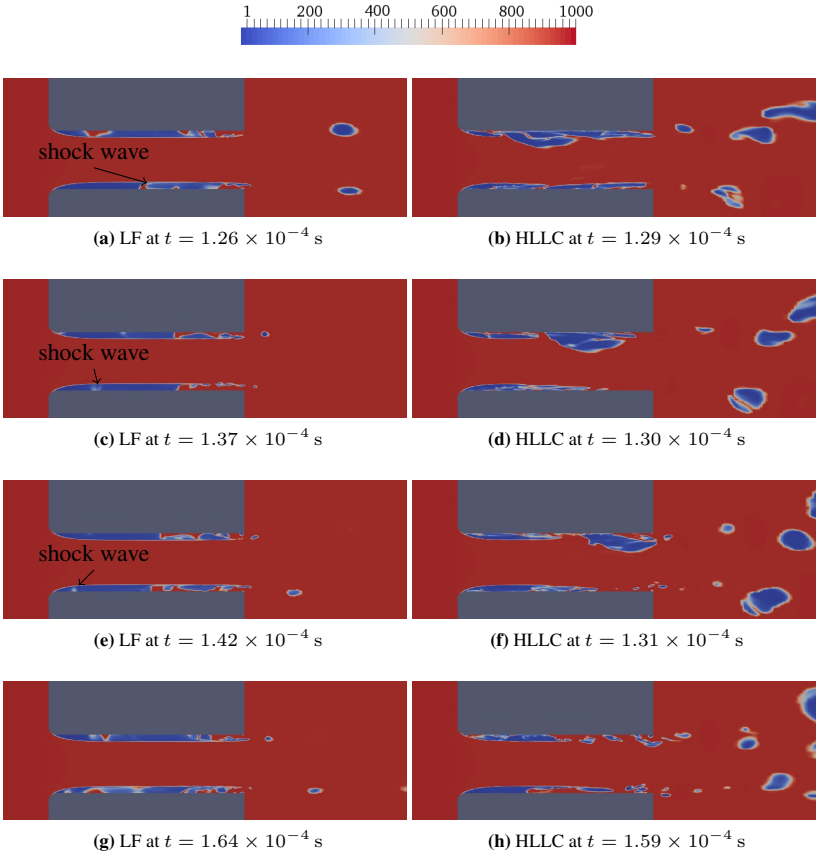

(a) LF at $t = 1.26 \times 10^{-4}$ s

(b) HLLC at $t = 1.29 \times 10^{-4}$ s

(c) LF at $t = 1.37 \times 10^{-4}$ s

(d) HLLC at $t = 1.30 \times 10^{-4}$ s

(e) LF at $t = 1.42 \times 10^{-4}$ s

(f) HLLC at $t = 1.31 \times 10^{-4}$ s

(g) LF at $t = 1.64 \times 10^{-4}$ s

(h) HLLC at $t = 1.59 \times 10^{-4}$ s

Figure 5.26.: Qualitative comparison of density $[\mathrm{kg\,m^{-3}}]$ for the LF and the HLLC Riemann solver for the micro channel flow with cavitation.

form close to the wall. Figure 5.27c shows the Persson indicator values. The colors are from blue to white to red, where blue indicates a low value, white the FV trigger value above which sub-cells are applied and red a high value of the indicator. The indicator values reflect the cavitation zone very well, which results in a good usage of FV elements (see Figure 5.27d).

(a) Density

(b) Density (zoom)

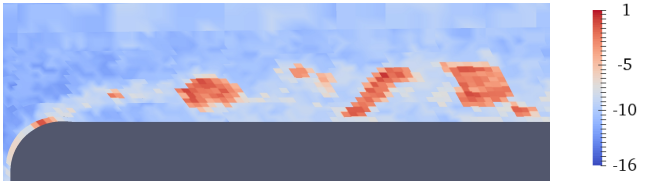

(c) Presson sensor values (zoom)

(d) FV elements (zoom)

Figure 5.27.: Example of shock capturing for the micro channel flow with cavitation.

In the following, a simulation with only FV elements and a simulation with DG are compared. Note that for the calculation with DG the FV shock capturing is sparsely applied where necessary. The DOF are 7.881×10^7. The HLLC Riemann solver is used for the flux calculation of both DG and FV elements. As shown in Hoffmann et al. [57] and Sonntag and Munz [112] the used FV is theoretical 2nd order. For the DG in combination with FV it is important to notice that for this case the DG is 5th order, however, for FV dominated areas the discretization becomes 2nd order. Therefore, it is important to use the FV shock-capturing as little as possible.

Figure 5.28 shows the pressure for a full FV simulation (Figure 5.28a) and a DG simulation with only sparsely used FV shock-capturing (Figure 5.28b). Here, the resolution within the micro channel is increased by a factor of two in each spatial direction compared to Figure 5.26. Hence, the general structures are smaller even with a full FV simulation, since the two-phase regions are always approximated with the FV scheme. In Figure 5.28a small areas of low pressure are present, i.e., cavitation, which move downstream and collapse at different locations. In this snapshot two shock waves are observable at the lower part of the channel. The shock waves origin seems to correspond to the cavitational area. A snapshot of the DG scheme is shown in Figure 5.28b. In comparison with the full FV simulation far more shock waves are represented and are more clearly observable. Even small structures are resolved and shock wave reflections from the wall are represented by the simulation. Overall, the DG scheme damps the waves far less.

One of the parameters to asses potential surface or component damage in a simulation is the maximum pressure at the surfaces. Therefore, the maximum wall pressure is analyzed for the micro channel flow. Figure 5.29 shows the maximum wall pressure for a time range from $t = 48 \times 10^{-6}\,\mathrm{s}$ to $51 \times 10^{-6}\,\mathrm{s}$. The absolute maximum pressure value at the surface is $15\,139\,\mathrm{bar}$. The maximum pressures at the leading edges are very small and about one channel height downstream pressure peaks are observable. These peaks range from several hundreds of bar up to a few thousand bar. The location corresponds to the area around the collapses, i.e., the origin of the shock waves, from Figure 5.28b. Due to the relatively short evaluation time of the maximum pressure single collapses can be identified. By increasing the evaluation time it can be expected to obtain whole areas of high maximum pressure.

In Figure 5.30 the cavitation zones are shown for the micro channel. The isosurfaces for the vapor mass fraction $x > 1 \times 10^{-7}$ are illustrated and the background surface shows the pressure. Even though the geometry is only 2D, the structures in the simulation are highly three dimensional. At the leading edges very thin cavitation zones span over the complete depth of the channel in an almost 2D manner. More downstream the cavitation zones or clouds grow and become less constant along the channel depth. At the location of between 1 and 2 channel heights downstream of the leading edge structures become very chaotic and large. Downstream of these large clouds less cavitation

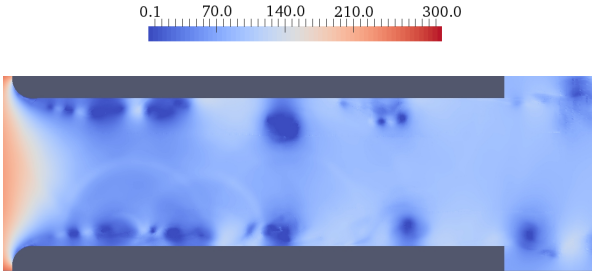

(a) Full FV (2nd order)

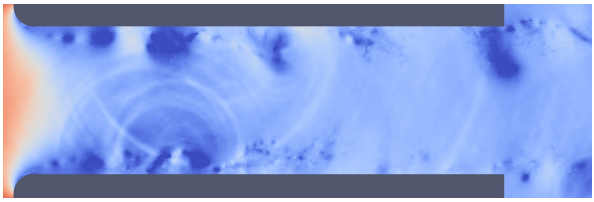

(b) DG (5th order) with FV shock capturing (2nd order)

Figure 5.28.: Qualitative comparison of the pressure [bar] for a FV scheme and DG scheme with FV shock capturing.

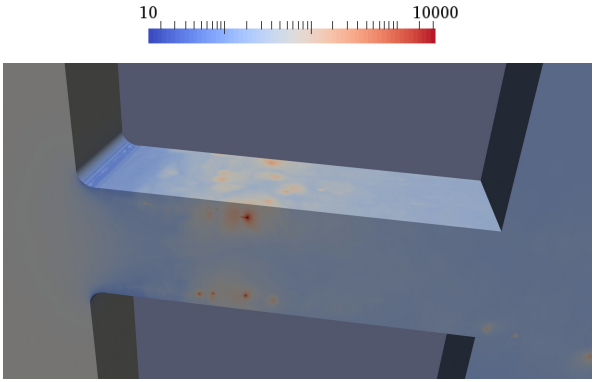

Figure 5.29.: Maximum pressure at the surfaces for $t = 48 \times 10^{-6}$ s to 51×10^{-6} s in bar; absolute maximum Pressure 15 139 bar.

zones are present. Consequently, most of them have collapsed at the location of the maximum wall pressures cf. Figure 5.29.

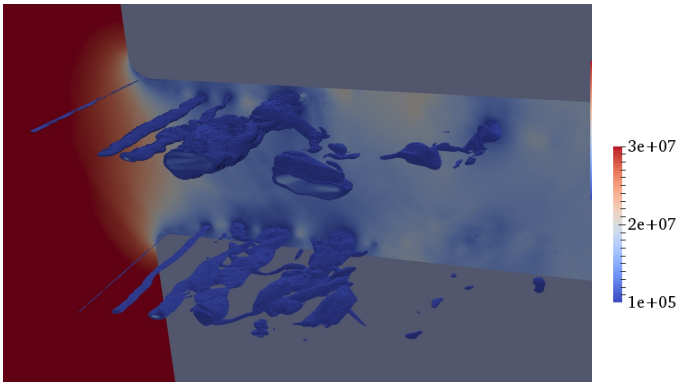

Figure 5.30.: Iso surfaces for vapor mass fraction $x > 1 \times 10^{-7}$ and background surface with pressure.

5.3. Conclusion

In the current chapter simulations with DGSEM and the tabulated EOS for water have been analyzed. In the first part single bubble collapses were investigated. The parameter study involved: grid convergence, variation in initial vapor fraction, variation in wall distance, different cross flow velocities and other parameters. The results of the bubble collapse were compared to the Rayleigh-Plesset equation and showed good agreement. In the literature even better agreement can be found, however, in the present study the Helmholtz formulation was used. It takes thermodynamic properties into account, which are neglected or simplified in the Rayleigh-Plesset equation; hence, the good agreement is satisfactory. Further, the grid convergence study showed the same trend as state-of-the-art simulations with other dense gas simulation codes [105], i.e., no grid convergence for the maximum pressure in the domain. However, for the wall pressure a grid independent solution was achieved.

In the second part, the proposed numerical simulation framework was applied to the most the challenging case in the present work, a micro channel flow with cavitation. With an additional stabilization method the stability of the simulation code was significantly improved for this type of flow. Two different Riemann solvers were compared,

the LF and the HLLC. Both obtained stable results, however, the simulations with the HLLC obtained more details of the flow. It has to be noted, that the HLLC in the used formulation approximates the contact discontinuity wrong, however, the results were still superior over the more dissipative LF.

Some of the key advantages of the applied methodology are:

- for good resolved simulation the Persson indicator works very efficiently,
- the pressure shocks are transported very well and
- the results were in good agreement with radius and deformations of bubbles close to the wall during collapse.

The applied methodology aims to combine the advantages of both high-order schemes and highly accurate EOS and to apply them to numerically very challenging flows. Therefore, a few drawbacks were found with the current implementation:

- Problems at phase jumps even with pure FV
- Time steps became extremely small for micro channel flow

Whilst the first point remains to be investigated, the latter is due to the high speed of sound in water and the very small grid cell.

6. Conclusion and prospect

The present work demonstrated the efficient coupling of a high order numerical method, DGSEM, and an accurate multiparameter EOS, based on the Helmholtz formulation. The proposed framework was applied to gaseous and liquid flows with shocks and phase changes. First, a 1D shock tube experiment was conducted and the results for ideal and real gas approximations were compared. It was shown that for the chosen medium, methane, great differences for most properties occur, e.g., propagation speed, temperature, density and pressure, at high pressures. At low pressures, which were commonly regarded as ideal gas regime, the results for ideal and real gas almost coincide. However, the temperature showed differences. Nonetheless, the differences would be negligible in most cases at low pressures, but the real gas approximation was a necessity at high pressures.

Based on these findings, the behavior of a supersonic jet with real gas approximation was examined. First, the setup was validated with a subsonic real gas jet to the self-similar jet theory. The simulation results agreed well with the data in the literature. Following the validation a jet development at high pressure and supersonic conditions were investigated and again compared to the ideal gas approximation. The development of the jet showed a very dynamic flow behavior, for which slow adjustment processes inside the narrowing are important. Further, the fluid experienced a phase change, due to a temperature drop before the shock. Even though this phase change occured only in a small area in the simulation, this effect should be represented by an appropriate EOS. Comparing the real gas with ideal gas approximation it was clear that strong differences were present. Lowering the pressure with a constant pressure ratio the real gas simulation flow structures converged towards the ideal gas results, e.g., first shock width. It was also demonstrated that the used Persson indicator was capable of detecting shocks and instabilities due to aliasing.

In the second results chapter, the behavior of the used dense gas approach for cavitation was assessed. First, a detailed parameter study for a single bubble collapse in water was conducted. The results were validated and verified to the bubble radius of the Rayleigh-Plesset equation and the state-of-the-art findings of pressure grid convergence, respectively. Both agreed with the reference data. For the bubble radius better agreements can be found in the literature than in the present work. However, the here used EOS took some additional fluid properties into account which are either neglected or simplified in the Rayleigh-Plesset equation. The parameter study for the bubble collapse included a variation of the initial state, e.g., vapor fraction inside the bubble, pressure

inside the bubble and in the far field, wall distance and cross flow velocity. The findings suggested that the used approach is capable of representing a number of physical effects. However, for the isolated bubble collapse other methods might be more suitable, e.g., with sharp interface models at the phase boundary. These more advanced and computationally more expensive methods, would however be infeasible for more complex flows at larger scales. Therefore, the conducted parameter study has contributed to a better understanding of simulations of such more complex flows in the industrial context.

It was also demonstrated that the proposed framework is capable of handling micro channel flows with cavitation. The results for the micro channel flow showed good quantitative agreement to the literature. A comparison between a high order and a low order simulation, i.e., 5th and 2nd order, respectively, showed the high potential of the proposed simulation framework. For the simulation with the high order the shock wave and pressure signals were represented much better than for the 2nd order FV with the same DOF.

Despite the high potential of the combination of a high-order scheme with a tabulated EOS, a number of challenges and unanswered questions remain. The lack of an appropriate sub-grid scale model lead to a loss in resolution due to FV sub-cell scheme as de-aliasing method. However, the current state-of-the-art de-aliasing methods for DGSEM, e.g., over-integration, increases the computational costs even further. Further, the coupling of the DG with the FV sub-cell shock capturing for multiphase flows with very strong gradients, e.g., cavitation, remains very challenging. The results suggest, especially from the single bubble collapse, that at the phase boundary non-physical pressure waves are being generated in the simulation. The applied methods needs to be further improved to avoid such a behavior at these extreme conditions.

Further, in the present work the indicator for the shock capturing has to be adjusted manually for each simulation. Whilst a SGS or de-aliasing method would improve the adjustment, the required indicator value might still change for different cases. Therefore, an improvement or a more general indicator trigger could improve the usability of the whole framework.

In terms of EOS representation the present work has contributed to underline the importance of an appropriate EOS approximation. However, the influence of the different fluid approximations needs to be investigated in further detail. The results in the present work suggest a strong influence of the fluid property modeling, however, it is still unknown when to apply which level of accurate for the EOS approximation, i.e., computational costs against accuracy.

Appendices

A. Expansion

The properties of a fluid have a significant influence on the expansion behavior. In Section 4.1.1 the effects of an isentropic expansion for methane were already assessed. However, other fluids behave differently and an isentropic expansion is also very different to an isenthalpic expansion. Therefore, both expansion processes for different fluids are briefly discussed to give the reader a general introduction on their properties.

A.1. Isentropic expansion

An isentropic expansion process is generally characterized by a temperature drop. In Equation (4.3) the isentropic expansion is described for arbitrary fluids. For the illustration in the following diagrams, the expression

$$\frac{T_1}{T_2} = \frac{T_1(p_1, s_1)}{T_2(p_2, s_1)}, \tag{A.1}$$

is used, where the indexes 1 and 2 denote the states before and after the expansion, respectively. Figure A.1 shows the temperature drop for methane, air and water. The temperature drops for gases more rapidly than for liquids. The temperature drop for water is only marginally compared with air and methane. For higher pressures air and methane become liquid and consequently the temperature drops less.

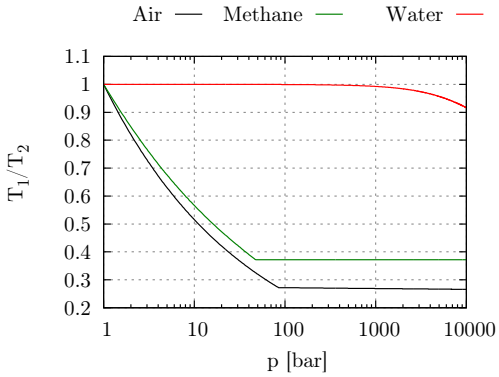

Figure A.1.: Temperature change T_1/T_2 for an isentropic expansion from p_1 to ambient pressure of 1 bar with an initial temperature of $T_1 = 300\,\mathrm{K}$.

A.2. Isenthalpic expansion

The isenthalpic expansion is often referred to as a Joule-Thomson process. For an arbitrary fluid the Joule-Thomson coefficient can be written as [115]

$$\left(\frac{\partial T}{\partial p}\right)_h = -\frac{1}{c_p}\left[v - T\left(\frac{\partial v}{\partial T}\right)_p\right]. \tag{A.2}$$

It is further worth noting that for an real gas commonly a temperature change occurs

$$(\Delta T)_h := T_1(p_1, h_1,) - T_2(p_2, h_1), \tag{A.3}$$

whilst for an ideal gas the temperature remains constant.

$$(\Delta T)_h := T_1(p_1, h_1,) - T_2(p_2, h_1) = 0 \tag{A.4}$$

Figure A.2 shows the temperature ratio T_1/T_2 for a pressure drop from p_1 to ambient pressure at $p_2 = 1\,\mathrm{bar}$ with the initial temperature $T_1 = 300\,\mathrm{K}$. All fluids have a similar trend, i.e., by increasing p_1 the temperature drops more until it reaches a minimum. A further increases in p_1 leads to a reduction of the temperature drop and for high pressures to a heating of the fluid.

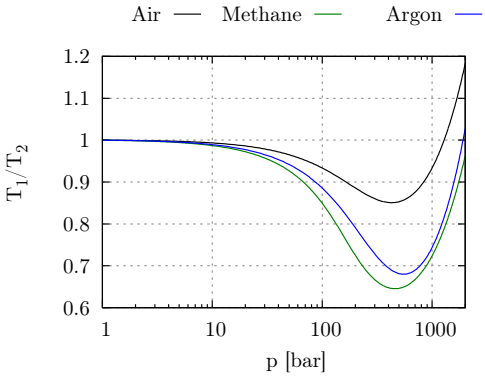

Figure A.2.: Temperature change T_1/T_2 for an isenthalpic expansion from p_1 to ambient pressure of 1 bar with a initial temperature of $T_1 = 300\,\mathrm{K}$.

B. Fluid diagramms

To keep this work self-contained, the essential fluid diagrams of this work are presented in this appendix. The graphs have been plotted with MATLAB and the COOLPROP library version 6 for MATLAB [15].

B.1. Temperature - Entropy

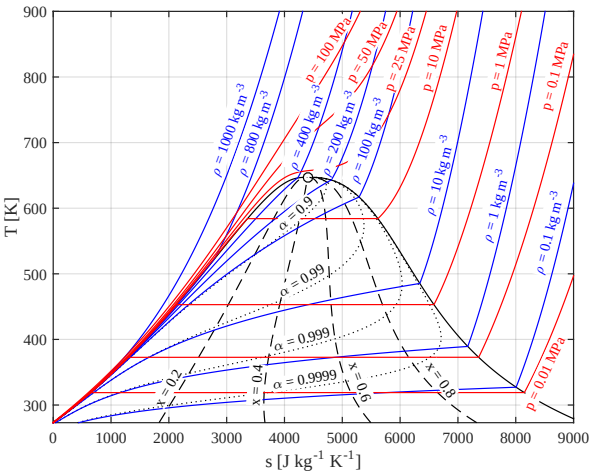

Figure B.1.: $T - s$ diagram for water; constant x (dashed), constant α (dotted), constant density (blue) and constant pressure (red).

B.2. Temperature - Density

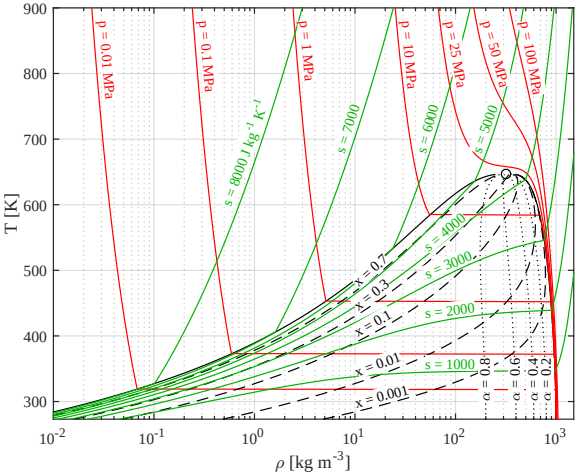

Figure B.2.: $T - \rho$ diagram for water; constant x (dashed), constant α (dotted), constant pressure (red) and constant entropy (green)

B.3. Temperature - specific inner Energy

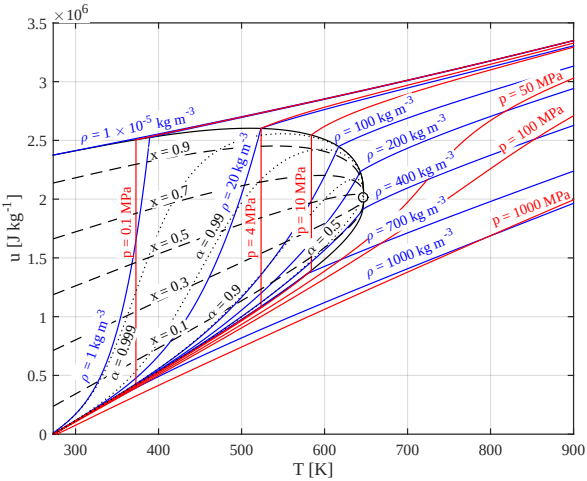

Figure B.3.: $T - u$ diagram for water; with lines for constant density (blue), constant pressure (red) constant x (dashed) and constant α (dotted).

B.4. Pressure - specific Enthalpy

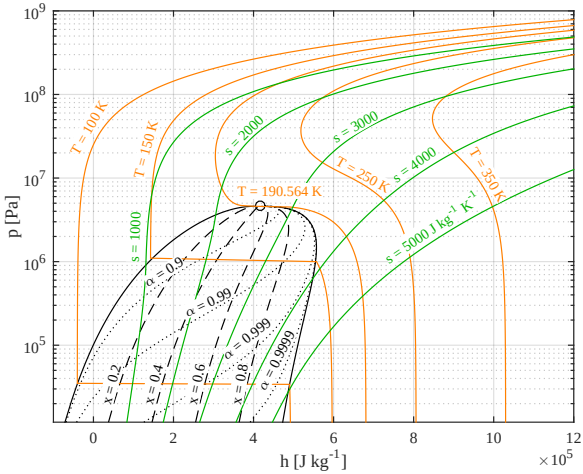

Figure B.4.: $P - h$ diagram for methane; with lines for constant constant entropy (green), constant temperature (orange) constant x (dashed) and constant α (dotted).

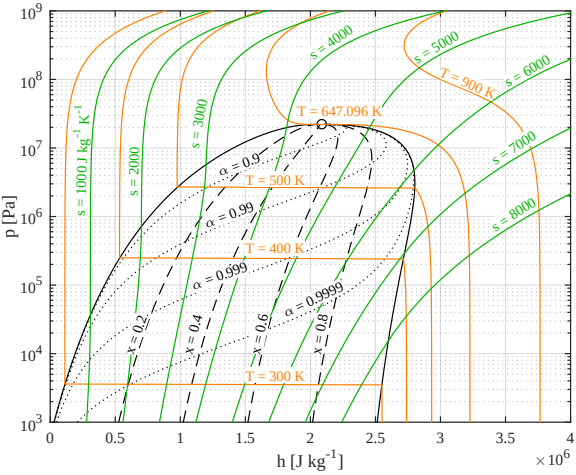

Figure B.5.: $P - h$ diagram for water; with lines for constant entropy (green), constant temperature (orange) constant x (dashed) and constant α (dotted).

Bibliography

[1] FPROPS - ASCEND. ascend4.org/FPROPS. Accessed: 16-12-01.

[2] N. A. Adams and S. J. Schmidt. *Shocks in Cavitating Flows*, pages 235–256. Springer Berlin Heidelberg, Berlin, Heidelberg, 2013.

[3] I. Akhatov, O. Lindau, A. Topolnikov, R. Mettin, N. Vakhitova, and W. Lauterborn. Collapse and rebound of a laser-induced cavitation bubble. *Physics of Fluids (1994-present)*, 13(10):2805–2819, 2001.

[4] C. Altmann, A. Taube, G. Gassner, F. Lörcher, and C.-D. Munz. Shock detection and limiting strategies for high order discontinuous Galerkin schemes. In Klaus Hannemann and Friedrich Seiler, editors, *Shock Waves*, pages 1053–1058. Springer Berlin Heidelberg, 2009.

[5] J. D. Anderson, J. Degroote, G. Degrez, E. Dick, R. Grundmann, and J. Vierendeels. *Computational fluid dynamics: an introduction*. Springer, 2009.

[6] S. Ashforth-Frost and K. Jambunathan. Effect of nozzle geometry and semi-confinement on the potential core of a turbulent axisymmetric free jet. *International Communications in Heat and Mass Transfer*, 23(2):155 – 162, 1996.

[7] P. C. Babu and K. Mahesh. Upstream entrainment in numerical simulations of spatially evolving round jets. *Physics of Fluids (1994-present)*, 16(10):3699–3705, 2004.

[8] P. C. Babu and K. Mahesh. Direct numerical simulation of passive scalar mixing in spatially evolving turbulent round jets. *AIAA Paper*, 1121:2005, 2005.

[9] H. D. Baehr. Der kritische Zustand und seine Darstellung durch die Zustandsgleichung. *Abh. Akad. Wissensch. Literatur, Mathem.-Naturwiss. Klasse*, page S. 235–333, 1953.

[10] H. D. Baehr and S. Kabelac. *Thermodynamik: Grundlagen und technische Anwendungen*. Springer-Verlag, 2012.

[11] F. Bassi, L. Botti, A. Colombo, A. Crivellini, A. Ghidoni, and F. Massa. On the development of an implicit high-order discontinuous Galerkin method for dns and implicit les of turbulent flows. *European Journal of Mechanics-B/Fluids*, 55:367–379, 2016.

[12] F. Bassi and S. Rebay. A high-order accurate discontinuous finite element method for the numerical solution of the compressible Navier-Stokes equations. *Journal of Computational Physics*, 131(2):267 – 279, 1997.

[13] C. E. Baumann and J. T. Oden. A discontinuous hp finite element method for the Euler and Navier–Stokes equations. *International Journal for Numerical Methods in Fluids*, 31(1):79–95, 1999.

[14] A. D. Beck, G. J. Gassner, and C.-D. Munz. High order and underresolution. In Rainer Ansorge, Hester Bijl, Andreas Meister, and Thomas Sonar, editors, *Recent Developments in the Numerics of Nonlinear Hyperbolic Conservation Laws*, volume 120 of *Notes on Numerical Fluid Mechanics and Multidisciplinary Design*, pages 41–55. Springer Berlin Heidelberg, 2013.

[15] I. H. Bell, J. Wronski, S. Quoilin, and V. Lemort. Pure and pseudo-pure fluid thermophysical property evaluation and the open-source thermophysical property library CoolProp. *Industrial & Engineering Chemistry Research*, 53(6):2498–2508, 2014.

[16] A. Berg, U. Iben, A. Meister, and J. Schmidt. Modeling and simulation of cavitation in hydraulic pipelines based on the thermodynamic and caloric properties of liquid and steam. *Shock Waves*, 14(1-2):111–121, 2005.

[17] S. Boblest, M. Hempert, F.and Hoffmann, P. Offenhäuser, M. Sonntag, F. Sadlo, C. W. Glass, C.-D. Munz, T. Ertl, and U. Iben. Toward a discontinuous Galerkin fluid dynamics framework for industrial applications. In *High Performance Computing in Science and Engineering´ 15*, pages 531–545. Springer, 2016.

[18] T. Bolemann, A. Beck, D. Flad, H. Frank, V. Mayer, and C.-D. Munz. High-order discontinuous Galerkin schemes for large-eddy simulations of moderate Reynolds number flows. In Norbert Kroll, Charles Hirsch, Francesco Bassi, Craig Johnston, and Koen Hillewaert, editors, *IDIHOM: Industrialization of High-Order Methods - A Top-Down Approach*, volume 128 of *Notes on Numerical Fluid Mechanics and Multidisciplinary Design*, pages 435–456. Springer International Publishing, 2015.

[19] F. Bonelli, A. Viggiano, and V. Magi. A numerical analysis of hydrogen underexpanded jets under real gas assumption. *Journal of Fluids Engineering*, 135(12):121101, 2013.

[20] J. P. Boris, F. F. Grinstein, E. S. Oran, and R. L. Kolbe. New insights into large eddy simulation. *Fluid dynamics research*, 10(4-6):199–228, 1992.

[21] C. E. Brennen. *Cavitation and Bubble Dynamics*. Cambridge University Press, 1995.

[22] C. E. Brennen. An introduction to cavitation fundamentals. 2011.

[23] E.-A. Brujan. *Cavitation in Non-Newtonian Fluids*. Springer Berlin Heidelberg, 2011.

[24] E.-A. Brujan and Y. Matsumoto. Collapse of micrometer-sized cavitation bubbles near a rigid boundary. *Microfluidics and Nanofluidics*, 13(6):957–966, 2012.

[25] A. Burbeau, P. Sagaut, and Ch.-H. Bruneau. A problem-independent limiter for high-order Runge–Kutta discontinuous Galerkin methods. *Journal of Computational Physics*, 169(1):111–150, 2001.

[26] J. Carlton. *Marine propellers and propulsion*. Butterworth-Heinemann, 2011.

[27] D. R. Chenoweth. Gas-transfer analysis. section h-real gas results via the van der Waals equation of state and virial expansion extension of its limiting Abel-Noble form. Technical report, Sandia National Labs., Albuquerque, NM (USA), 1983.

[28] H. M. Cho and B.-Q. He. Spark ignition natural gas engines—a review. *Energy Conversion and Management*, 48(2):608 – 618, 2007.

[29] M. Chorazewski, F. Dergal, T. Sawaya, I. Mokbel, J.-P. E. Grolier, and J. Jose. Thermophysical properties of normafluid (iso 4113) over wide pressure and temperature ranges. *Fuel*, 105:440 – 450, 2013.

[30] H. Cochard. Cavitation in trees. *Comptes Rendus Physique*, 7(9-10):1018 – 1026, 2006. Nucleation Nucléation.

[31] J. R. Cooper. Representation of the ideal-gas thermodynamic properties of water. *International Journal of Thermophysics*, 3(1):35–43, 1982.

[32] I. Dincer and C. Zamfirescu. A review of novel energy options for clean rail applications. *Journal of Natural Gas Science and Engineering*, 28:461 – 478, 2016.

[33] N. Dittakavi, A. Chunekar, and S. Frankel. Large eddy simulation of turbulent-cavitation interactions in a venturi nozzle. *J. Fluids Eng.*, 132(12):11, 2010.

[34] M. Dumbser, U. Iben, and C.-D. Munz. Efficient implementation of high order unstructured WENO schemes for cavitating flows. *Computers & Fluids*, 86(0):141 – 168, 2013.

[35] J. H. Dymond and R. Malhotra. The tait equation: 100 years on. *International Journal of Thermophysics*, 9(6):941–951, 1988.

[36] C. P. Egerer, S. Hickel, S. J. Schmidt, and N. A. Adams. Large-eddy simulation of turbulent cavitating flow in a micro channel. *Physics of Fluids (1994-present)*, 26(8):–, 2014.

[37] C. P. Egerer, S. J. Schmidt, S. Hickel, and N. A. Adams. Efficient implicit LES method for the simulation of turbulent cavitating flows. *Journal of Computational Physics*, 316:453 – 469, 2016.

[38] S. D. Fechter. *Compressible multi-phase simulation at extreme conditions using a discontinuous Galerkin scheme*. PhD thesis, University of Stuttgart, 2015.

[39] F. H. Fisher and O. E. Dial Jr. Equation of state of pure water and sea water. Technical report, DTIC Document, 1975.

[40] Ansys Fluent. 15.0. *User's Guide. Physical Models for the Discrete Phase Model. Cap*, 24(5), 2013.

[41] J.-P. Franc and J.-M. Michel. *Fundamentals of Cavitation*. Fluid Mechanics and Its Applications. Springer Netherlands, 2005.

[42] D. G. Friend, J. F. Ely, and H. Ingham. Thermophysical properties of methane. *Journal of Physical and Chemical Reference Data*, 18(2):583–638, 1989.

[43] H. Ganesh. *Bubbly shock propagation as a cause of sheet to cloud transition of partial cavitation and stationary cavitation bubbles forming on a delta wing vortex*. PhD thesis, The University of Michigan, 2015.

[44] H. Ganesh, S. A. Mäkiharju, and S. L. Ceccio. Bubbly shock propagation as a mechanism for sheet-to-cloud transition of partial cavities. *Journal of Fluid Mechanics*, 802:37–78, 2016.

[45] G. J. Gassner and A. D. Beck. On the accuracy of high-order discretizations for underresolved turbulence simulations. *Theoretical and Computational Fluid Dynamics*, 27(3-4):221–237, 2013.

[46] G. J. Gassner and D. A. Kopriva. A comparison of the dispersion and dissipation errors of Gauss and Gauss-Lobatto discontinuous Galerkin spectral element methods. *SIAM Journal on Scientific Computing*, 33(5):2560–2579, 2011.

[47] F. R. Gilmore. The growth or collapse of a spherical bubble in a viscous compressible liquid. 1952.

[48] A. Gnanaskandan and K. Mahesh. A numerical method to simulate turbulent cavitating flows. *International Journal of Multiphase Flow*, 70(0):22 – 34, 2015.

[49] A. Gnanaskandan and K. Mahesh. Large eddy simulation of the transition from sheet to cloud cavitation over a wedge. *International Journal of Multiphase Flow*, 83:86 – 102, 2016.

[50] F. F. Grinstein and C. Fureby. Recent progress on MILES for high Reynolds number flows. *Journal of Fluids Engineering*, 124(4):848–861, 2002.

[51] A. Hamzehloo and P. G. Aleiferis. Large eddy simulation of highly turbulent under-expanded hydrogen and methane jets for gaseous-fuelled internal combustion engines. *International Journal of Hydrogen Energy*, 39(36):21275 – 21296, 2014.

[52] F. Hempert, S. Boblest, T. Ertl, F. Sadlo, P. Offenhäuser, C. W. Glass, M. Hoffmann, A. Beck, C.-D. Munz, and U. Iben. Simulation of real gas effects in supersonic methane jets using a tabulated equation of state with a discontinuous galerkin spectral element method. *Computers & Fluids*, 145(2):167–179, 2016.

[53] F. Hempert, S. Boblest, M. Hoffmann, P. Offenhäuser, F. Sadlo, C. W. Glass, C.-D. Munz, T. Ertl, and U. Iben. *High Performance Computing in Science and Engineering '16*, chapter High-Pressure Real-Gas Jet and Throttle Flow as a Simplified Gas Injector Model Using a Discontinuous Galerkin Method, pages 289–300. Springer International Publishing, 2016.

[54] F. Hempert, M. Hoffmann, U. Iben, and C.-D. Munz. On the simulation of industrial gas dynamic applications with the discontinuous Galerkin spectral element method. *Journal of Thermal Science*, 25(3):250–257, 2016.

[55] S. Hickel, M. Mihatsch, and S. J. Schmidt. Implicit large eddy simulation of cavitation in micro channel flows. *WIMRC 3rd International Cavitation Forum*, 2011.

[56] F. Hindenlang, G. J. Gassner, C. Altmann, A. D. Beck, M. Staudenmaier, and C.-D. Munz. Explicit discontinuous galerkin methods for unsteady problems. *Computers & Fluids*, 61:86–93, 2012.

[57] M. Hoffmann, S. Boblest, P. Offenhäuser, and C.-D. Munz. A robust high-order discontinuous galerkin solver for fluid flow with cavitation. In *Proceedings of the 9th International Conference on Computational Fluid Dynamics*, 2016.

[58] J. W. Holl and A. L. Treaster. Cavitation hysteresis. *Journal of Basic Engineering*, 88(1):199–211, 1966.

[59] B. Huang, Y. Zhao, and G. Wang. Large eddy simulation of turbulent vortex-cavitation interactions in transient sheet/cloud cavitating flows. *Computers & Fluids*, 92:113 – 124, 2014.

[60] M. L. Huber, R. A. Perkins, D. G. Friend, J. V. Sengers, M. J. Assael, I. N. Metaxa, K. Miyagawa, R. Hellmann, and E. Vogel. New international formulation for the thermal conductivity of H_2O. *Journal of Physical and Chemical Reference Data*, 41(3):033102, 2012.

[61] M. L. Huber, R. A. Perkins, A. Laesecke, D. G. Friend, J. V. Sengers, M. J. Assael, I. N. Metaxa, E. Vogel, R. Mareš, and K. Miyagawa. New international formulation for the viscosity of H_2O. *Journal of Physical and Chemical Reference Data*, 38(2):101–125, 2009.

[62] U. Iben, F. Wrona, C.-D. Munz, and M. Beck. Cavitation in hydraulic tools based on thermodynamic properties of liquid and gas. *Journal of Fluids Engineering*, 124(4):1011–1017, 2002.

[63] M. Jungemann. *1D-Modellierung und Simulation des Durchflussverhaltens von Hydraulikkomponenten bei sehr hohen Drücken unter Beachtung der thermodynamischen Zustandsgrössen von Mineralöl*. VDI-Verlag, 2005.

[64] R. Khaksarfard, M. R. Kameshki, and M. Paraschivoiu. Numerical simulation of high pressure release and dispersion of hydrogen into air with real gas model. *Shock Waves*, 20(3):205–216, 2010.

[65] S. W. Kieffer. Sound speed in liquid-gas mixtures: Water-air and water-steam. *Journal of Geophysical research*, 82(20):2895–2904, 1977.

[66] M. Koch, C. Lechner, F. Reuter, K. Köhler, R. Mettin, and W. Lauterborn. Numerical modeling of laser generated cavitation bubbles with the finite volume and volume of fluid method, using OpenFOAM. *Computers & Fluids*, 126:71–90, 2016.

[67] N. I. Kolev. *Transiente Zweiphasen-Strömung*. Springer-Verlag, 2013.

[68] T. Korakianitis, A. M. Namasivayam, and R. J. Crookes. Natural-gas fueled spark-ignition (SI) and compression-ignition (CI) engine performance and emissions. *Progress in Energy and Combustion Science*, 37(1):89 – 112, 2011.

[69] P. Kumar and R. P. Saini. Study of cavitation in hydro turbines—a review. *Renewable and Sustainable Energy Reviews*, 14(1):374 – 383, 2010.

[70] K. K. Kuo. Principles of combustion. 1986.

[71] T. G. Lang. *Speed, Power, And Drag Measurements of Dolphins and Porpoises*, pages 553–572. Springer US, Boston, MA, 1975.

[72] W. Lauterborn and H. Bolle. Experimental investigations of cavitation-bubble collapse in the neighbourhood of a solid boundary. *Journal of Fluid Mechanics*, 72(02):391–399, 1975.

[73] T. Leighton. *The acoustic bubble*. Academic press, 2012.

[74] E. W. Lemmon, M. L. Huber, M. O. McLinden, et al. NIST standard reference database 23: Reference fluid thermodynamic and transport properties — REFPROP. National Institute of Standards and Technology, Standard Reference Data Program, 2013.

[75] D. Lohse, B. Schmitz, and M. Versluis. Snapping shrimp make flashing bubbles. *Nature*, 413(6855):477–478, 2001.

[76] K. Mahesh. The interaction of jets with crossflow. *Annual Review of Fluid Mechanics*, 45:379–407, 2013.

[77] C. Mauger, L. Méès, M. Michard, and M. Lance. Velocity measurements based on shadowgraph-like image correlations in a cavitating micro-channel flow. *International Journal of Multiphase Flow*, 58(0):301 – 312, 2014.

[78] R. S. McDowell and F. H. Kruse. Thermodynamic functions of methane. *Journal of Chemical and Engineering Data*, 8(4):547–548, 1963.

[79] G. P. McTaggart-Cowan, H. L. Jones, S. N. Rogak, W. K. Bushe, P. G. Hill, and S. R. Munshi. The effects of high-pressure injection on a compression–ignition, direct injection of natural gas engine. *Journal of engineering for gas turbines and power*, 129(2):579–588, 2007.

[80] G. P. McTaggart-Cowan, K. Mann, J. Huang, A. Singh, B. Patychuk, X. Zheng, and S. Munshi. Direct injection of natural gas at up to 600 bar in a pilot-ignited heavy-duty engine. *SAE International Journal of Engines*, 8(3):981–996, 2015.

[81] Stefanie Meburger. Simulation des Kollapses einzelner Kavitationsblasen. Master's thesis, University of Stuttgart, 2016.

[82] M. S. Mihatsch, S. J. Schmidt, M. Thalhamer, and N. A. Adams. Numerical prediction of erosive collapse events in unsteady compressible cavitating flows. In Luís Eça, Eugenio Oñate, Julio García-Espinosa, Trond Kvamsdal, and Pål Bergan, editors, *MARINE 2011, IV International Conference on Computational Methods in Marine Engineering*, volume 29 of *Computational Methods in Applied Sciences*, pages 187–198. Springer Netherlands, 2013.

[83] Mitja Morgut, Enrico Nobile, and Ignacijo Biluš. Comparison of mass transfer models for the numerical prediction of sheet cavitation around a hydrofoil. *International Journal of Multiphase Flow*, 37(6):620 – 626, 2011.

[84] S. Müller, M. Bachmann, D. Kröninger, T. Kurz, and P. Helluy. Comparison and validation of compressible flow simulations of laser-induced cavitation bubbles. *Computers & fluids*, 38(9):1850–1862, 2009.

[85] C.-D. Munz and T. Westermann. *Numerische Behandlung gewöhnlicher und partieller Differnzialgleichungen*. Springer Berlin Heidelberg, 2012.

[86] C. F. Naude, Charl F., and A. T. Ellis. On the mechanism of cavitation damage by nonhemispherical cavities collapsing in contact with a solid boundary. *Journal of Basic Engineering*, 83(4):648–656, 1961.

[87] M. L. Norman and K.-H. A. Winkler. Supersonic jets. *Los Alamos: Los Alamos National Laboratory, 1985*, 1, 1985.

[88] M. L. Norman, K.-H. A. Winkler, L. Smarr, and M. D. Smith. Structure and dynamics of supersonic jets. *Astronomy and Astrophysics*, 113:285–302, 1982.

[89] N. R. Panchapakesan and J. L. Lumley. Turbulence measurements in axisymmetric jets of air and helium. part 1. air jet. *Journal of Fluid Mechanics*, 246:197–223, 1993.

[90] F. Payri, R. Payri, F. J. Salvador, and J. Martínez-López. A contribution to the understanding of cavitation effects in diesel injector nozzles through a combined experimental and computational investigation. *Computers & Fluids*, 58:88 – 101, 2012.

[91] D.-Y. Peng and D. B. Robinson. A new two-constant equation of state. *Industrial & Engineering Chemistry Fundamentals*, 15(1):59–64, 1976.

[92] P.-O. Persson and J. Peraire. Sub-cell shock capturing for discontinuous galerkin methods. *AIAA*, 112, 2006.

[93] A. Philipp and W. Lauterborn. Cavitation erosion by single laser-produced bubbles. *Journal of Fluid Mechanics*, 361:75–116, 1998.

[94] M. Pini, A. Spinelli, G. Persico, and S. Rebay. Consistent look-up table interpolation method for real-gas flow simulations. *Computers & Fluids*, 107:178 – 188, 2015.

[95] K. S. Pitzer. *Origin of the acentric factor*. Jan 1977.

[96] M. S. Plesset and R. B. Chapman. Collapse of an initially spherical vapour cavity in the neighbourhood of a solid boundary. *J. Fluid Mech*, 47(2):283–290, 1971.

[97] M. S. Plesset and A. Prosperetti. Bubble dynamics and cavitation. *Annual Review of Fluid Mechanics*, 9(1):145–185, 1977.

[98] S. E. Quinones-Cisneros and U. K. Deiters. Generalization of the friction theory for viscosity modeling. *The Journal of Physical Chemistry B*, 110(25):12820–12834, 2006. PMID: 16800618.

[99] G. Raman. Supersonic jet screech: Half-century from powell to the present. *Journal of Sound and Vibration*, 225(3):543 – 571, 1999.

[100] J. L. Reboud, O. Coutier-Delgosha, B. Pouffary, and R. Fortes-Patella. Numerical simulation of unsteady cavitating flows: Some applications and open problems. *Fifth International Symposium on Cavitation*, 2003.

[101] O. Redlich and J. N. S. Kwong. On the thermodynamics of solutions. v. an equation of state. fugacities of gaseous solutions. *Chemical reviews*, 44(1):233–244, 1949.

[102] D. Rist. *Dynamik realer Gase: Grundlagen, Berechnungen und Daten für Thermogasdynamik, Strömungsmechanik und Gastechnik*. Springer, Berlin; Heidelberg [u.a.], 1996.

[103] G. Rutkai, M. Thol, R. Lustig, R. Span, and J. Vrabec. Communication: Fundamental equation of state correlation with hybrid data sets. *The Journal of Chemical Physics*, 139(4), 2013.

[104] F. J. Salvador, J. Martinez-Lopez, J.-V. Romerob, and M.-D. Rosell. Computational study of the cavitation phenomenon and its interaction with the turbulence developed in diesel injector nozzles by large eddy simulation (les). *Mathematical and Computer Modelling*, 57:1656–1662, 2013.

[105] S. J. Schmidt, M. Mihatsch, M. Thalhamer, and N. A. Adams. Assessment of the prediction capability of a thermodynamic cavitation model for the collapse characteristics of a vapor-bubble cloud. *WIMRC 3rd International Cavitation Forum*, 3, 2011.

[106] A. J. R. Schneider. *Some compressibility effects in cavitation bubble dynamics*. PhD thesis, California Institute of Technology, 1949.

[107] U. Setzmann and W. Wagner. A new equation of state and tables of thermodynamic properties for methane covering the range from the melting line to 625 k at pressures up to 100 mpa. *Journal of Physical and Chemical Reference Data*, 20(6):1061–1155, 1991.

[108] R. Skoda, U. Iben, A. Morozov, M. Mihatsch, S. J. Schmidt, and N. A. Adams. Numerical simulation of collapse induced shock dynamics for the prediction of the geometry, pressure and temperature impact on the cavitation erosion in micro channels. In *Warwick WIMRC 3rd International Cavitation Forum*, 2011.

[109] A. J. Smits and J.-P. Dussauge. *Turbulent Shear Layers in Supersonic Flow*. Springer New York, 2nd edition, 2006.

[110] G. Soave. Equilibrium constants from a modified Redlich-Kwong equation of state. *Chemical Engineering Science*, 27(6):1197–1203, 1972.

[111] M. Sonntag and C.-D. Munz. Shock capturing for discontinuous Galerkin methods using finite volume subcells. In Jürgen Fuhrmann, Mario Ohlberger, and Christian Rohde, editors, *Finite Volumes for Complex Applications VII-Elliptic, Parabolic and Hyperbolic Problems*, volume 78 of *Springer Proceedings in Mathematics & Statistics*, pages 945–953. Springer International Publishing, 2014.

[112] M. Sonntag and C.-D. Munz. Efficient parallelization of a shock capturing for discontinuous Galerkin methods using finite volume sub-cells. *Journal of Scientific Computing*, pages 1–28, 2016.

[113] A. Sou, B. Biçer, and A. Tomiyama. Numerical simulation of incipient cavitation flow in a nozzle of fuel injector. *Computers & Fluids*, 103:42 – 48, 2014.

[114] R. Span. *Multiparameter Equations of State: An Accurate Source of Thermodynamic Property Data*. Engineering online library. Springer, 2000.

[115] P. Stephan, K. Schaber, K. Stephan, and F. Mayinger. *Thermodynamik: Grundlagen und technische Anwendungen Band 1: Einstoffsysteme*. Springer-Lehrbuch. Springer Berlin Heidelberg, 2013.

[116] I. Szabó. *Geschichte der mechanischen Prinzipien: und ihrer wichtigsten Anwendungen*, volume 32. Birkhäuser Basel, 1979.

[117] C. K. W. Tam. Supersonic jet noise. *Annual Review of Fluid Mechanics*, 27(1):17–43, 1995.

[118] Christopher K.W. Tam, Nikolai N. Pastouchenko, and Robert H. Schlinker. Noise source distribution in supersonic jets. *Journal of Sound and Vibration*, 291(1):192 – 201, 2006.

[119] S. Tanaka, S. Bunya, J. J. Westerink, C. Dawson, and R. A. Luettich. Scalability of an unstructured grid continuous galerkin based hurricane storm surge model. *Journal of Scientific Computing*, 46(3):329–358, 2011.

[120] H. K. Tanna. An experimental study of jet noise part I: Turbulent mixing noise. *Journal of Sound and Vibration*, 50(3):405 – 428, 1977.

[121] H. K. Tanna. An experimental study of jet noise part II: Shock associated noise. *Journal of Sound and Vibration*, 50(3):429 – 444, 1977.

[122] C. Tegeler, R. Span, and W. Wagner. A new equation of state for argon covering the fluid region for temperatures from the melting line to 700 k at pressures up to 1000 mpa. *Journal of Physical and Chemical Reference Data*, 28(3):779–850, 1999.

[123] E. F. Toro. *Riemann Solvers and Numerical Methods for Fluid Dynamics*. Springer, 2009.

[124] D. H. Trevena. *Cavitation and tension in liquids*. Adam Hilger, 1987.

[125] A. Unsworth, D. Dowson, and V. Wright. Cracking joints. a bioengineering study of cavitation in the metacrapophalangeal joint. *Annals of the Rheumatic Diseases*, 1971.

[126] M. Versluis, B. Schmitz, A. von der Heydt, and D. Lohse. How snapping shrimp snap: Through cavitating bubbles. *Science*, 289(5487):2114–2117, 2000.

[127] A. Vogel, W. Lauterborn, and R. Timm. Optical and acoustic investigations of the dynamics of laser-produced cavitation bubbles near a solid boundary. *Journal of Fluid Mechanics*, 206:299–338, 1989.

[128] M. Voß. *Numerische, theoretische und experimentelle Untersuchungen zur Kavitationsblasendynamik*. PhD thesis, Mathematisch-Naturwissenschaftlichen Fakultäten der Georg-August-Universität zu Göttingen, 2002.

[129] V. Vuorinen, J. Yu, S. Tirunagari, O. Kaario, M. Larmi, C. Duwig, and B. J. Boersma. Large-eddy simulation of highly underexpanded transient gas jets. *Physics of Fluids (1994-present)*, 25(1):016101, 2013.

[130] W. Wagner. Software fluidcal. *Ing W. Wagner, Lehrstuhl für Thermodynamik, Ruhr-Universitaet Bochum*, 2005.

[131] W. Wagner and A. Pruß. The IAPWS formulation 1995 for the thermodynamic properties of ordinary water substance for general and scientific use. *Journal of Physical and Chemical Reference Data*, 31(2):387–535, 2002.

[132] W. Wagner, A. Saul, and A. Pruß. International equations for the pressure along the melting and along the sublimation curve of ordinary water substance. *Journal of Physical and Chemical Reference Data*, 23(3):515–527, 1994.

[133] G. Wang and M. Ostoja-Starzewski. Large eddy simulation of a sheet/cloud cavitation on a NACA0015 hydrofoil. *Applied Mathematical Modelling*, 31(3):417 – 447, 2007.

[134] M. Watanabe and A. Prosperetti. The effect of gas diffusion on the nuclei population downstream of a cavitation zone. Technical report, American Society of Mechanical Engineers, New York, NY (United States), 1994.

[135] Y.-J. Wei, C.-C. Tseng, and G.-Y. Wang. Turbulence and cavitation models for time-dependent turbulent cavitating flows. *Acta Mechanica Sinica*, 27(4):473–487, 2011.

[136] C. C. Wiart, K. Hillewaert, L. Bricteux, and G. Winckelmans. Implicit LES of free and wall-bounded turbulent flows based on the discontinuous Galerkin/symmetric interior penalty method. *International Journal for Numerical Methods in Fluids*, 78(6):335–354, 2015.

[137] I. Wygnanski and H. Fiedler. Some measurements in the self-preserving jet. *Journal of Fluid Mechanics*, 38(03):577–612, 1969.

[138] F. R. Young. *Cavitation*. World Scientific, 1999.

[139] J. Yu, V. Vuorinen, O. Kaario, T. Sarjovaara, and M. Larmi. Visualization and analysis of the characteristics of transitional underexpanded jets. *International Journal of Heat and Fluid Flow*, 44(0):140 – 154, 2013.

List of Tables

List of Figures